Erling Aares Vårli

Effects of Mn content and cooling conditions in a rolled AA 3005A alloy

Master's thesis in Materials Science and Engineering
Supervisor: Knut Marthinsen
Co-supervisor: Håkon Wiik Ånes and Kristian Knarbakk
July 2021

Master's thesis

NTNU
Norwegian University of Science and Technology
Faculty of Natural Sciences
Department of Materials Science and Engineering

NTNU
Norwegian University of
Science and Technology

Erling Aares Vårli

Effects of Mn content and cooling conditions in a rolled AA 3005A alloy

Master's thesis in Materials Science and Engineering
Supervisor: Knut Marthinsen
Co-supervisor: Håkon Wiik Ånes and Kristian Knarbakk
July 2021

Norwegian University of Science and Technology
Faculty of Natural Sciences
Department of Materials Science and Engineering

NTNU
Norwegian University of
Science and Technology

Abstract

Secondary aluminium production involves remelting of aluminium scrap along with additions of primary aluminium and alloying elements. As the chemical compositions of the scrap are not the same every time, the produced alloy will also have some chemical variations from time to time, which may influence the material properties. Material properties are, of course, also highly affected by process parameters. For rolled products, these could be e.g. rolling temperature, strain, strain rate etc. Both processing parameters and the chemistry of the alloy may significantly affect features in the material like microstructure, texture and microchemistry, which in turn may affect the material properties. A comprehensive understanding of the effects of processing conditions and chemical variations is therefore necessary in order to control the material properties of rolled aluminium sheets. The present study has investigated the effect of cooling conditions following hot rolling for two rolled AA 3005A alloys containing 1.11 wt.% and 1.33 wt.% Mn. Two parallels of each alloy were investigated: One cooled by air, and one cooled by a fan, i.e. 'slow' vs 'fast' cooling. The materials have been examined in the hot rolled and cold rolled state, and during back-annealing by an isothermal annealing experiment at 315 °C.

The effects have been evaluated in terms of mechanical properties, texture, microstructure and microchemistry. Mechanical properties have been measured by tensile- and hardness testing. The microstructure and texture of the materials have been characterized by the electron backscatter diffraction (EBSD) technique, followed by subsequent analysis using the MTEX MATLAB toolbox. Microchemistry has been analyzed using backscatter electron imaging (BSE), energy-dispersive X-ray spectroscopy (EDS) and electrical conductivity measurements. The results revealed that the effect of cooling conditions and Mn content on mechanical properties generally were small. However, the alloy containing 1.33 wt.% Mn showed significantly slower recrystallization kinetics when cooled by a fan, compared to air, which is believed to be attributed to increased concurrent precipitation following possibly more Mn in solid solution after hot rolling and cooling. For both alloys, fan cooling resulted in the precipitation of a higher number of dispersoids compared to air, following hot rolling. The fan cooling also resulted in a lower amount of Mn incorporated into constituent particles. Texture and texture evolution was shown to be mainly unaffected by the Mn content and cooling conditions studied in this work.

The assessment of the effects of cooling conditions following hot deformation at different Mn contents contributes to a more comprehensive understanding of the effects of variations in chemistry and processing conditions in 3xxx alloys. Further, this knowledge may allow Hydro more freedom in process design for this particular alloy with respect to variations in chemical composition and cooling conditions after hot rolling.

Sammendrag

Sekundærproduksjon av aluminium innebærer omsmelting av aluminiumsskrap i tillegg til tilsetninger av primæraluminium og legeringselementer. Ettersom den kjemiske sammensetningen i skrapet varierer vil dette også føre til variasjoner i kjemien til den ferdige legeringen, noe som kan påvirke egenskapene til materialet. Materialegenskaper påvirkes selvsagt også i stor grad av prosesseringsparametre. For valsede produkter kan slike parametre være valsetemperatur, tøyning eller tøyningsrate, for å nevne noen. Både prosessparametre og kjemisk sammensetning kan ha store effekter på materialkarakteristikker som mikrostruktur, tekstur og mikrokjemi, som igjen kan påvirke egenskapene til materialet. En omfattende forståelse av effektene av variasjoner i prosessparametre og kjemisk sammensetning er derfor nødvendig for å kontrollere materialegenskaper i valsede aluminiumslegeringer. Denne studien har undersøkt effekten av forskjellige avkjølingforhold etter varmvalsing i to valsede AA 3005A legeringer, som inneholdt henholdsvis 1,11 wt.% og 1,33 wt.% Mangan. To paralleller for hver av disse legeringene ble studert: Én avkjølt i luft, og én avkjølt ved hjelp av en vifte, som gir langt raskere avkjøling. Materialene har blitt undersøkt etter varmvalsing, kaldvalsing, og under tilbakegløding av det kalddeformerte materialet gjennom et isotermt glødeeksperiment ved 315 °C.

Mulige effekter på materialenes mekaniske egenskaper, tekstur, mikrostruktur og mikrokjemi er blitt studert. Mekaniske egenskaper har blitt undersøkt ved hjelp av strekkprøving og hardhetstester. Mikrostrukturen og teksturen til material har blitt karakterisert ved hjelp av diffraksjon av tilbakespredte elektroner (EBSD), etterfulgt av analyse ved bruk av MATLAB verktøykassen MTEX. Mikrokjemi har blitt analysert ved bruk av billeddannelse gjennom atomnummerkontrast ved hjelp av tilbakespredte elektroner og målinger av elektrisk ledningsevne. Resultatene viste at effektene av avkjølingsforholdene og manganinnholdet undersøkt i denne studien, generelt var små. Ikke desto mindre viste legeringen som inneholdt 1,33 wt.% Mn signifikant tregere rekrystallisasjonskinetikk ved viftekjøling sammenlignet med luftkjøling, noe som antakelig stammer fra økt samtidig presipitering i det viftekjølte materialet, muligens på grunn av mer Mn i fast løsning etter varmvalsing. For begge manganinnhold resulterte viftekjøling i mindre innlemmelse av mangan i konstituente partikler. Tekstur og teksturutvikling viste seg å hovedsaklig være upåvirket av manganinnholdet og avkjølingsforholdene som ble undersøkt i denne studien.

Kartleggingen av effektene av avkjølingsforhold etter varmvalsing ved ulike manganinnhold, bidrar til en mer helhetlig forståelse av effektene av variasjoner i kjemi og prosessparametre i 3xxx-legeringer. Videre kan denne kunnskapen tillate Hydro mer frihet i prosesseringen av denne bestemte legeringen, med hensyn til kjemisk sammensetning og avkjøling etter varmvalsing.

Preface

The work in this report has been carried out as part of the course TMT4905 - Materials Technology, Master's Thesis at Department of Materials Science and Engineering (DMSE) at the Norwegian University of Science and Technology, during the spring of 2021. The work has been carried out in collaboration with Hydro Aluminium Rolled Products, Holmestrand.

I would like to express my deepest appreciation to my supervisor, Professor Knut Marthinsen. Your advice, feedback, fruitful discussions and good sense of humor have all been very valuable for me to carry out this thesis, and I really appreciate your extensive effort.

I am also extremely grateful to my co-supervisor at NTNU, Ph.D. Candidate Håkon Wiik Ånes. He has helped me and provided me with scripts for the MTEX MATLAB toolbox, and assisted me at the EM lab at NTNU. Håkon, I really appreciate all your help, advice and feedback, and I wish you the best in the future.

I would also like to thank my co-supervisor, Kristian Knarbakk at Hydro Holmestrand, for his valuable advice and feedback during this project.

A special thanks to Yingda Yu at the EM lab at NTNU. Thank you for all your assistance and your fantastic humor. I am also thankful for the assistance from Pål Christian Skaret, Berit Vinje Kramer and Marit Elinda Olaisen Odden at DMSE.

I would like to thank all my classmates. The past five years in Trondheim have been fantastic, which is very much thanks to all of you. I wish you all the best of luck in the future.

Last but not least, thank you to my parents. Your encouragement and support have been, and are invaluable.

Trondheim, July 2021
Erling Aares Vårli

Contents

Abstract i

Sammendrag iii

Preface v

1 Introduction 1

2 Theory 3

2.1 Aluminium alloys . . . 3
2.2 Production of rolled aluminium sheets . . . 4
2.3 Formation and evolution of second phase particles . . . 6
2.4 Plastic deformation in FCC metals . . . 6
2.4.1 Single crystal deformation . . . 6
2.4.2 Polycrystal deformation . . . 7
2.5 Strengthening mechanisms . . . 8
2.5.1 Solid solution strengthening . . . 9
2.5.2 Strain hardening . . . 9
2.5.3 Dispersoid strengthening . . . 9
2.5.4 Grain size strengthening . . . 10
2.5.5 Substructure strengthening . . . 10
2.6 Softening behaviour . . . 10
2.6.1 Recovery . . . 11
2.6.2 Recrystallization . . . 12
2.6.3 Grain growth . . . 13
2.6.4 Influence of second phase particles and solutes . . . 14
2.6.5 Interaction between recrystallization and precipitation . . . 15
2.7 Texture . . . 17
2.7.1 Characteristic textures . . . 18

2.8 Electron Backscatter Diffraction . . . 21

3 Experimental **23**

3.1 Delivered material . . . 23
3.2 Material processing . . . 23
3.3 Vickers hardness test . . . 24
3.4 SEM sample preparation . . . 25
3.5 Electron Backscatter Diffraction . . . 25
3.5.1 Data Aquisition . . . 25
3.5.2 Indexing . . . 26
3.5.3 Post-processing of orientation data . . . 26
3.6 Macrotexture Analysis . . . 27
3.7 Microtexture Analysis . . . 28
3.7.1 Orientation Distribution Function . . . 28
3.8 Second phase particle analysis . . . 29
3.9 Isothermal annealing experiments . . . 30
3.10 Electrical conductivity . . . 31
3.11 Tensile testing . . . 32

4 Results **33**

4.1 Mechanical properties and electrical conductivity . . . 34
4.1.1 Hot deformed material . . . 34
4.1.2 Estimate of Mn_{SS} . . . 35
4.1.3 Back-annealing of "As deformed" material . . . 35
4.2 Microstructure . . . 38
4.2.1 Orientation maps . . . 38
4.2.2 Segmentation maps . . . 43
4.2.3 Grain statistics . . . 44
4.3 Texture . . . 47
4.3.1 ϕ_2 sections . . . 47
4.3.2 Volume fraction of texture components . . . 51
4.4 Second phase particles . . . 53
4.4.1 Second phase particle size distributions . . . 55
4.5 EDS analysis of constituent particles . . . 57

5 Discussion **59**

5.1 Main findings . . . 59

5.2 "Hot deformed" 60
5.3 "As deformed" 61
5.4 Back-annealing of "As deformed" 62
5.5 "Fully RX" 63

6 Further Work **65**

7 Conclusion **67**

References **69**

A Segmentation maps **75**

B Microtexture **81**

1 | Introduction

In this study, rolled aluminium alloys produced by Hydro Aluminium Rolled Products, Holmestrand (Hydro), have been investigated. Hydro is a manufacturer of secondary aluminium in the form of flat rolled sheets and coils. Secondary aluminium involves remelting of aluminium scrap and additions of primary aluminium and alloying elements. As the chemical compositions of the scrap are not the same every time, the produced alloy will also have some chemical variations from time to time. The melt is Direct Chill (DC) cast into rolling slabs, which are transformed into thin sheets through thermomechanical processing in terms of hot and cold deformation. The deformation strengthens the material but reduces ductility. The sheets manufactured by Hydro are often processed further through forming operations such as deep drawing, which requires a certain formability of the material. Hence, the cold deformed sheet is subjected to a subsequent annealing step, which aims to give the desired combination of strength and formability. At Hydro, the hot deformed material may be cooled to ambient temperature through natural cooling or by forced convection using a fan. As fan cooling induces a higher cooling rate than natural cooling, this allows faster processing of the fan cooled materials. The rolling induces preferred crystallographic orientations (texture) in the material, which is the origin of mechanical anisotropy. This is of particular interest for metal sheets intended for further forming operations such as deep drawing, for which mechanical anisotropy may lead to material loss through various degrees of elongation in different directions, known as "earing". The properties of the finished product is a complex interplay between strengthening mechanisms and softening reactions, where the presence of alloying elements in the form of second phase particles or solid solution play a major role. Second phase particles and solute elements may accelerate or retard the softening kinetics, thus affecting the material's response to annealing. Alloying elements also affects the evolution of texture, both during deformation and annealing.

The sheets produced by Hydro must fulfill requirements of mechanical properties and chemical content according to certain standards. At Hydro, many alloys are produced with more narrow chemical composition than specified in the standards, limiting the chemical variations in the alloys. The AA 3005A alloy, on the other hand, uses the whole range of elemental contents specified in the standard because it contains more recycled aluminium. From an environmental and economic perspective, using a higher fraction of recycled material in the products is beneficial, as remelting of scrap aluminium consumes far less energy compared to primary aluminium, and scrap aluminium is cheaper than primary aluminium.[1] However, as the variations in chemistry increase, a good understanding of how these variations affect the properties and annealing response of the material is needed in order to maintain control of the properties of the final product. It is well established that the manganese (Mn) content may severely affect

the annealing response of 3xxx-alloys,[2] which may range from 1-1.5 wt% for the AA 3005A alloy produced by Hydro.

The properties of the rolled sheets are also a result of numerous process parameters such as homogenization temperature, hot rolling temperature, strain rate, total strain and annealing temperature, amongst many. Many of these process paramaters have been previously been extensively studied.[3–7] To the author's knowledge, little research has been carried out on the effect of cooling conditions following hot deformation in aluminium alloys. In the present work, the effect of cooling conditions following hot deformation will be investigated for an AA 3005A alloy, at two different nominal Mn contents: 1.11 wt.% and 1.33 wt.%. As mentioned earlier, cooling from hot deformation to ambient temperature may occur by natural cooling or fan cooling at Hydro. To study the combined effect of cooling conditions and Mn content, two parallels were studied for each Mn content: One parallel cooled by air, and one cooled by a fan. The study will examine the effect of the mentioned parameters on the evolution of mechanical properties and texture by investigating materials from the hot deformed and cold deformed state, and by studying the response of back-annealing on the cold deformed material. The mechanical properties will be measured using Vickers hardness testing and tensile testing. Electron Backscatter Diffraction (EBSD) and analysis in the MTEX MATLAB Toolbox[8] will provide information on the development of the grain structure and texture in the materials. The development of microchemistry in terms of volume fraction, distribution and chemical composition of second phase particles will be examined using Backscatter Electron (BSE) imaging and Energy-dispersive X-Ray Spectroscopy (EDS) and further processing in the image processing software ImageJ/FIJI.[9] Electrical conductivity measurements will also be carried out to indicate the level of Mn in solid solution.

The investigations will reveal possible differences in material properties as a result of varying Mn content and cooling conditions. The investigations will provide statistics on grain structure, second phase particles and electrical conductivity, which will give a good basis to discuss if eventual differences in material properties and annealing response can be attributed to any differences in microstructure and microchemistry. Together, this will give a more complete understanding of the effect of Mn content and cooling conditions, hence contribute to more control of the material properties of this alloy.

2 | Theory

Production of rolled aluminium sheet and foils is done by reducing thick, Direct Chill (DC) cast slabs into thin sheets. The reduction is done by alternating deformation and heating steps, known as thermomechanical processing. As previously mentioned in Chapter 1, this processing involves strengthening and softening reactions, along with the development of preferred crystallographic orientations. In alloys, i.e. metals containing a severe amount of alloying elements, the presence of solute elements and second phase particles may have a huge impact. This chapter will in more detail address the processing of aluminium sheets and relevant strengthening methods and softening reactions involved. The role of solutes, second phase particles and other relevant parameters will also be covered. Basic theory about crystallography and texture measurements will also be included, as they are necessary to understand the methodology used in this work, and to discuss the results.

2.1 Aluminium alloys

Aluminium alloys are industrially important materials, commonly used in construction, packaging and transport. Some of the key properties of aluminium alloys are their high specific strength, good formability, good corrosion resistance and high thermal and electric conductivity. Aluminium possesses the Face Centred Cubic (FCC) crystal structure, which gives the highest possible atomic packing factor, 74 %. Primary aluminium is produced by the electrolysis process developed independently in 1886 by Charles Hall and Paul Héroult. Alumina produced by the Bayer process[1] is dissolved in a molten salt, mainly containing cryolite. The dissolved alumina is reduced to aluminium in the electrolysis process, by the reaction

$$\frac{1}{2}\mathrm{Al_2O_3} + \frac{3}{4}\mathrm{C} \rightarrow \mathrm{Al} + \frac{3}{4}\mathrm{CO_2}.$$

Secondary aluminium production involves remelting of aluminium scrap, which contains alloying elements and impurities. To modify the chemical composition of the scrap melt to the desired alloy, pure aluminium and alloying elements are added. This process consumes only 5 % of the energy compared to primary production.[1,10]

Aluminium alloys are divided into cast and wrought aluminium alloys. The alloys can further be categorized as heat-treatable or non-heat-treatable, indicating whether or not the primary strengthening mechanism is related to heat treatment or not. Wrought aluminium alloys are denoted as XXXX, where the first digit denotes the series, which represents the main alloying element(s). The two last digits represents different alloys within the series. The second digit

denotes the original alloy and possible variations of the given alloy. In an alloy family (i.e. digit 1, 3 and 4 are the same), the alloy with the lowest value of the second digit is considered the original alloy, while other values are modifications of the original alloy.[11] The 3xxx series is a wrought, non-heat-treatable aluminium alloy, with manganese as its main alloying element. Initially, the alloy gets its strength from elements in solid solution, and can be further hardened by cold work.[12] 3xxx-alloys are used in applications such as beverage cans, heat exchangers and cooking utensils.

2.2 Production of rolled aluminium sheets

Figure 2.1 shows a generic process route for rolled aluminium sheets. Firstly, the melt is DC cast to a rolling slab containing a coarse microchemistry, i.e. the distribution of alloying elements in solid solution and second phase particles. The slab is then homogenized and/or pre-heated prior to hot deformation, at a temperature around 500-600 °C. At this temperature, the coarse microchemistry is transformed to a finer one, as coarse particles may be redissolved or spheroidised, and fine particles may precipitate from the supersaturated matrix.[13] The hot deformation is normally carried out in several passes at 450-500 °C. At this temperature, the flow stress is lower and the ductility is higher compared to cold deformation, which allows severe thickness reductions. The main objectives of the hot deformation is to severely reduce the thickness of the slab, and transform the casting structure to a more homogenous one.[7] The cold deformation occurs at temperatures lower than 40 % of the melting temperature, and is also carried out in several passes, or break downs. The thickness reduction is much smaller compared to hot deformation, but allows a precise control of the final dimensions and material properties of the material. The cold deformed metal is strong, but not very ductile. Often, and especially for materials intended for further forming operations as deep drawing, a more ductile material is required. This is achieved by a heat treatment known as back-annealing, which softens the material and results in a proper combination of strength and ductility. Different and alternating deformation and heating steps induce changes in microchemistry, and alternating deformation and softening reactions are associated with microstructure and texture changes, shown in Figure 2.1. After hot rolling the material may be non-recrystallized, partially or fully recrystallized depending in the alloy composition and the specific processing conditions, while after cold rolling the material will in any case be in a fibrous deformed state, while a fully recrystallized structure will be re-established during the final back-annealing stage. The texture will change accordingly. The details of the changes in microstructure, microchemistry and texture will be discussed in detail in Section 2.6, 2.3 and 2.7.1, respectively.

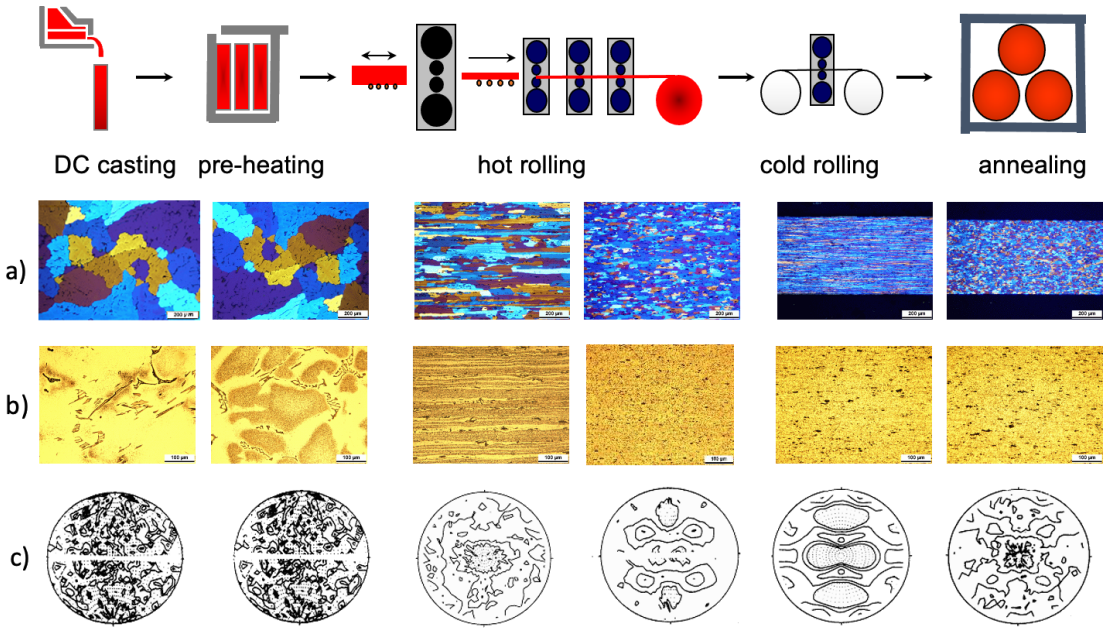

Figure 2.1: *Generic process route for rolled metal sheets, showing the development of a) microstructure b) microchemistry and c) texture.*[14]

2.3 Formation and evolution of second phase particles

3xxx-alloys are composed of the Al matrix and intermetallic second phase particles. Second phase particles can be divided into constituent particles and dispersoids. The constituent particles are larger, and form during casting, while the dispersoids are smaller and form during subsequent processing of the material. Dispersoids may be formed during homogenization/preheating, as concurrent precipitation (i.e. simultaneously with recrystallization during back-annealing), which will be addressed in Section 2.6.5, or subsequent to recrystallization. Second phase particles may either promote or retard recrystallization, depending on their size, spatial distribution and the thermomechanical history of the material. Large particles, > 1 µm are usually associated with acceleration of recrystallization due to Particle Stimulated Nucleation, while fine dispersoids can retard or suppress recrystallization due to the Zener drag.[15] Both these phenomena will be addressed in Section 2.6.2. This section covers the formation and evolution of second phase particles, while effects of such particles in terms of recrystallization kinetics and texture evolution will be addressed in Section 2.6.2 and 2.7, respectively.

For DC-cast 3xxx alloys, the casting structure consist of $(FeMn)Al_6$, Mg_2Si and α-$Al(Fe, Mn)Si$ constituent particles.[16,17] The presence of such particles are influenced by the excact chemistry and the solidification conditions of the alloy. For instance, at magnesium concentrations in the range of 0.8 - 1.3 %, Mg_2Si constituents are observed.[17] Higher Si concentrations promotes α-$Al(Fe, Mn)Si$ and Mg_2Si at the expence of $(FeMn)Al_6$ particles. Much of the Mn remains in solid solution after casting.

During homogenization, the Mg_2Si particles are dissolved. This releases silicon, which is believed to assist the transformation of $(FeMn)Al_6$ particles into α-$Al_{15}(FeMn)_3Si_2$. The manganese is partly incorporated into Fe-bearing constituents, and partly as fine α-$Al_{15}Mn_3Si_2$ dispersoids.[17] α-$Al_{15}Mn_3Si_2$ are the most common type of dispersoids in 3xxx alloys, but $Al_6(Fe, Mn)$ dispersoids are also observed when the Si-content is very low.[18,19]

2.4 Plastic deformation in FCC metals

2.4.1 Single crystal deformation

In cubic metals, deformation can occur by slip or twinning. FCC metals with medium to high stacking fault energy (SFE), such as aluminium, deforms by slip. Hence, twinning will not be discussed. For slip to occur in a single crystal, the shear stress on a given slip plane must exceed a critical resolved shear stress (CRSS). Figure 2.2 shows slip in a single crystal, where the CRSS is given as[20]

$$\tau_R = \frac{P\cos\lambda}{A/\cos\phi}, \tag{2.1}$$

where $P\cos\lambda$ is the force along the slip direction, and $A/\cos\phi$ is the projection of the cross sectional area, A, on the slip plane.

When the shear stress on a given slip plane exceeds the CRSS, deformation occurs by dislocation motion along that slip plane, shown in Figure 2.3. During slip, dislocations move in preferred planes and directions. A slip plane and a slip direction makes up what is known as a slip system. Slip planes and directions are usually the planes and directions within that plane that are the

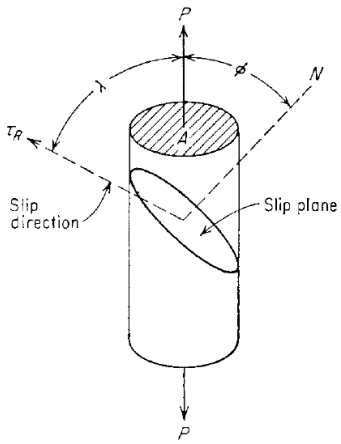

Figure 2.2: *Geometry for calculating critical resolved shear stress for a single crystal.*[20]

most close packed. In aluminium, there are primarily 12 slip systems, which are made up of the {111}-planes and ⟨110⟩-directions. However, it is also known that to some extent, slip can occur in other planes than the {111}-planes for FCC metals, especially at high temperature deformation.[21,22] When a crystal deforms by slip, a rotation of the crystal lattice is necessary to accommodate the external imposed load. If the crystal is subjected to tensile stress, the slip plane will rotate towards the direction of the imposed load. In compression, the plane normal of the slip plane will rotate towards the direction of the imposed load, i.e. the slip plane will rotate towards an antiparallel configuration to the load axis. The situations above are illustrated in Figure 2.4.

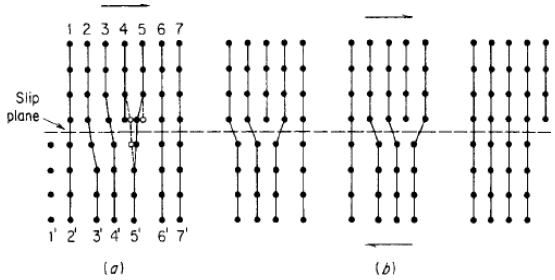

Figure 2.3: *a) Atom movements near dislocations in slip. b) Movement of an edge dislocation.*[20]

2.4.2 Polycrystal deformation

When a polycrystal is deformed by slip, each individual grain deform on the most favorable slip systems as well as complying with the imposed load (strain and/or stress). Hence, the orientation changes during the deformation are non-random, and a deformation texture is developed. In general, the deformation texture evolution can be considered a combination of crystallographic constraints (slip) and geometrical constraints (imposed load). Several theories have been proposed to predict the texture evolution of polycrystals during plastic deformation, starting from the early work of Sachs[24] and Taylor.[25]

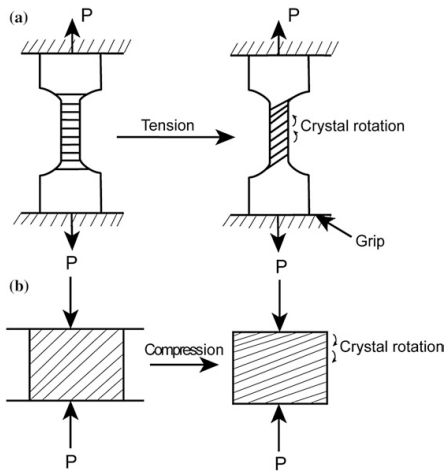

Figure 2.4: *Deformation by slip and crystal lattice rotation in (a) tensile and (b) compressive stress.*[23]

The Sachs theory assumes that the stress in each grain is the same as the external stress, and that each grain will deform on the slip system that has the highest resolved shear stress. As a result, the grains in the Sachs model deform like single crystals with the same orientation, i.e. with no constraints, which is why the model is referred to as the "No Constraint" model.[26]

The Taylor theory, on the other hand, assumes that the strain in all grains are the same as the external strain and is therefore referred to as the "Full Constraint" model. In order to fulfill the strain condition, five independent slip systems must be activated. As cubic metals have numerous combinations of available independent slip systems that could be a solution, e.g. 384 combinations in FCC metals, a condition must be set in order to select a combination of slip systems. Taylor's solution was the set of slip system that required the minimal internal work on an increment of deformation of the grain. However, this criterion yields multiple equivalent solutions in terms of minimum internal work, but with different lattice rotations. This is known as "the Taylor ambiguity", and is a well known weakness in the model.[27,28]

Ever since the publications from Sachs and Taylor, prediction of texture evolution in plastically deformed polycrystals has been extensively studied, and still is to this day. Other models and approaches have been made, with the purpose of improving the prediction of texture evolution. For a more comprehensive overview on modeling of plastic anisotropy, the reader is referred e.g. to the work of Gawad, van Bael and Van Houtte.[29]

2.5 Strengthening mechanisms

Aluminium alloys can be strengthened in several ways, e.g. by deformation or heat treatment. This section will cover the relevant methods for non-heat-treatable wrought alloys.

2.5.1 Solid solution strengthening

Aluminium can be hardened by introducing foreign atoms into the aluminium lattice. The hardening is achieved due to interactions between solute atoms and dislocations.[30] For elements forming solid solutions, the hardening effect increases with difference in atomic radii between the solute element and the Al matrix. Manganese (Mn) has a 11.3 % smaller atomic radii than aluminium, making the hardening effect in super pure aluminium highly effective. However in 3xxx-alloys, the addition of manganese is not as effective in terms of solid solution hardening compared to a pure aluminium alloy, due to the formation of Mn-containing second phase particles in 3xxx-alloys.

2.5.2 Strain hardening

Strain hardening, or work hardening, is an important process for strengthening of industrial aluminium alloys. The ductile metal is subjected to plastic deformation, which strengthens the material. The hardening implies that dislocations gliding on intersecting systems interacts in an obstructive manner. These interactions could be stress fields around dislocations, locking of intersecting dislocations, and slip systems penetrating other slip systems.[20] As a result more and more dislocations are stored in the material with increasing strain, i.e. the dislocation density, ρ, increases. From these processes, strain hardening theories have been developed, which has resulted in the following equation, relating the resolved shear stress τ to the dislocation density, ρ:

$$\tau = \alpha G b \sqrt{\rho}, \tag{2.2}$$

where G is the shear modulus and b is the magnitude of the burgers vector. α is a constant related to the geometry of interaction between dislocations and the obstacles that determines the flow stress.[31]

2.5.3 Dispersoid strengthening

During deformation, particles may introduce excess dislocations if they to do not deform. Dislocations will bow around the particles, and leave a dislocation loop around the particle, known as an Orowan loop. This increases the dislocation density in the material, and may have a significant effect on the yield strength of the material.[31] The total contribution of fine dispersoids on the yield strength due to the Orowan mechanism, σ_{oro}, is given as[32]

$$\Delta\sigma_p = \frac{0.81 M A G b}{2\pi\lambda} \ln\frac{\pi d}{4b}, \tag{2.3}$$

where M is the Taylor factor, G is the shear modulus of the matrix, b is Burgers vector, and d is the average size of the dispersoids. The constant A can be estimated by $A = 1/\sqrt{1-v}$, where v is the Poisson's ratio,.[32] λ is the spacing between dispersoids (surface to surface) on a slip plane, given as[33]

$$\lambda = 0.4d\left(\sqrt{\frac{\pi}{f_v}} - 2\right), \tag{2.4}$$

where f_v is the volume fraction of dispersoids.

The effect of dispersoids in 3xxx alloys has been proven to have a significant effect on the yield strength. Muggerud et al. showed that a high number density of dispersoids resulted in a significant increase of the yield strength, and that the dispersion hardening effect increased with higher Mn and Si contents. The effect of dispersoid hardening are not restricted to the yield strength, as they may also contribute to work hardening. Previous work have shown an increased work hardening in aluminium alloys attributed to dispersoids at low strains, but that the effect diminishes at higher strains.[33,34]

2.5.4 Grain size strengthening

Since the pioneering work of Hall and Petch on steels, it has been known that the a smaller grain size may strengthen polycrystalline metals. Their work was based on that grain boundaries restricted dislocation movement, and resulted in the famous Hall-Petch equation, which relates the yield stress, σ_0, to the grain size, D.[35,36] The equation is given as

$$\sigma_0 = \sigma_i + kD^{-\frac{1}{2}}, \tag{2.5}$$

where σ_i is the friction stress, which represents the resistance of the crystal lattice to dislocation movement. k is a constant related to the hardening effect of grain boundaries.[20]

2.5.5 Substructure strengthening

Substructures can be defined as a mixture of single dislocations and dislocation arrangements.[37] The dislocation arrangements observed in FCC metals as aluminium are tangles, subgrains and cells, which will be adressed in Section 2.6.1. In the case of dislocations arranged in cells, their strengthening effect is attributed to a high dislocation density, which increases as the cell size decreases.[38] In general the substructure strengthening is related to the total dislocation density as described in Equation (2.2). In the case of a well developed subgrain structure, the substructure strengthening contribution can be expressed by the following relationship:[39]

$$\sigma \propto \frac{1}{\delta}. \tag{2.6}$$

Here, σ is the flow stress and δ is the subgrain size.[37,40]

Although materials show different preferences in what kind of substructure that is developed (e.g. high SFE materials tend to develop cell structures), it must be emphasized that materials rarely develops substructures consisting of categorically cells or subgrains, and that it can be hard to distinguish between them. As will be discussed in 2.6.1, cell structures can be transformed into subgrains through recovery processes, which will affect the appearance of the substructure in the form of cells and/or subgrains.[41]

2.6 Softening behaviour

As described in Section 2.5.2, ductile metals can be strengthened by plastic deformation. The strengthening is accompanied by an increase in the in the free energy of the material due to an increased number of defects in the material. Subsequent annealing can reduce the energy in the material by thermally activated processes, transforming the strengthened metal back to a

ductile state, i.e. the metal can be softened. Softening is often described in terms of recovery, recrystallization and grain growth, which all are processes that lower the free energy in the material, but have different impact on the microstructure. Figure 2.5 shows schematically how the properties of the metal change during these processes.

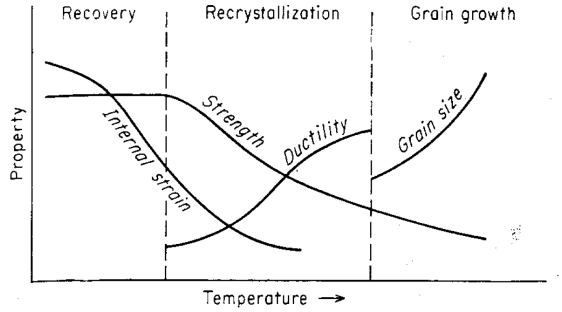

Figure 2.5: *Schematic drawing of the evolution of material properties during softening processes.*[20]

Softening reactions as recovery and recrystallization can are not restricted to subsequent annealing and may also occur during deformation, for which they are termed "dynamic". If they occur during subsequent annealing, they are termed "static". Annealing phenomena may also be classified as continuous or discontinuous. Discontinuous processes occur heterogeneously through the material and can be described by nucleation and growth stages, while continuous processes occur uniformly, without the observable nucleation and growth stages.

2.6.1 Recovery

Recovery partially restores the material properties to their pre-deformed state, through series of events. In the deformed material, dislocations are arranged in substructures within the grains. The substructures may display various degrees of development, which all involves orientation gradients within the grains.[31] Recovery transforms the substructures, which are typically dislocation tangles or cells, into subgrains with fewer, but more misoriented boundaries, which may also grow. A typical series of events during recovery is displayed in Figure 2.6, which shows the transition of a substructure consisting of dislocations ordered in tangles into well-defined subgrains. It must be emphasized that this is just a typical course of recovery, and the occurrence and the order of the events depends on several factors, such as material, purity, strain etc. Some of the recovery events may already have occurred in the deformed material during deformation, i.e. dynamic recovery.

Lowering the free energy in the material during recovery occurs mainly through two processes, being annihilation of dislocations, and rearrangement of dislocations to lower energy states. Annihilation of edge dislocations may occur through dislocation glide within the same glide plane alone, or by a combination of glide and dislocation climb. Dislocation climb requires thermal activation, and can thus only occur at high homologous temperatures. Screw dislocations may annihilate through cross-slip, which is available at lower temperature for high SFE materials such as aluminium. The dislocations that are not annihilated, may still be transformed into lower energy configurations. This is done through aligning dislocations across glide planes, forming low angle grain boundaries (LAGBs).[43,44]

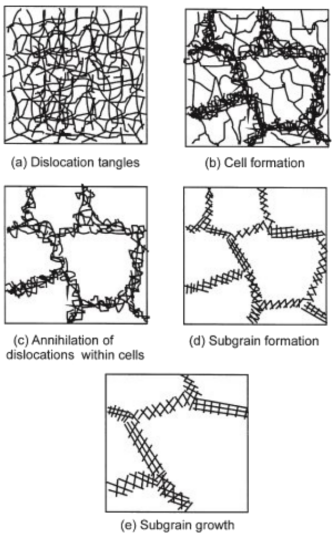

Figure 2.6: *Typical proceeding of recovery processes.*[42]

The angle of a LAGB with spacing h between edge dislocations of Burgers vector, b, can be approximated to

$$\theta \approx \frac{b}{h}, \tag{2.7}$$

at low angles. The energy of such a boundary, γ_0, is given by the Read-Shockley equation:[45]

$$\gamma_s = \gamma_0\, \theta(A - \ln \theta) \tag{2.8}$$

Here, $\gamma_0 = Gb/4\pi\,(1-v)$, $A = 1 + \ln(b/2\pi\, r_o)$, v is the Poisson's ratio, G is the shear modulus, and r_0 is the radius of the dislocation core, usually taken between b and $5b$. It follows from Equation (2.7) and (2.8) that the energy of a boundary increases by the angle θ, while the energy per dislocation decreases. Hence, the energy of the system can be lowered by arranging the dislocations in fewer, but more misoriented LAGBs.

2.6.2 Recrystallization

As described in the previous section, recovery may partially restore the properties of the deformed metal. The restoration process may proceed with recrystallization, through formation of strain-free grains within the deformed microstructure. The new strain-free grains grow, and consumes the deformed microstructure. As the dislocation-rich deformed microstructure are consumed by strain-free grains, it follows that the dislocation density, thus also the internal energy of the metal decreases.[21,42] An important feature to notice is that recovery and recrystallization are competing processes, as they both are driven by the stored energy from the deformation. As recrystallization consumes the strained, deformed microstructure into a strain-free microstructure, recovery processes cannot occur anymore. Vice versa, as recovery reduces the driving force for recrystallization, the extent of the recovery may retard or even completely

hinder the recrystallization process. Recrystallizaition may originate from classical nucleation, which essentially is small crystallites originating in the deformed structures, which have formed high angle boundaries with the matrix through recovery processes. Another recrystallization mechanism is strain induced grain boundary migration (SIBM), which was first observed by Beck and Sperry,[46] and involves the growth of an already present grain boundary, which leaves an area with lower dislocation content behind. Typically, the new grains has similar orientations from the grain they have grown from.[47]

The recrystallization behaviour is a complex matter, which is influenced by numerous factors, such as annealing time, temperature, prior deformation, composition, initital grain size and the extent of previous recovery processes.[20] This is well illustrated in by the work of Tangen et al. showed in Figure 2.7. The figure shows an Al-Mn alloy deformed to 95 %, isothermally annealed at a temperature above (a) and below (b) a critical temperature, resulting in two completely different recrystallized microstructures.[48] The presence of second phase particles and solutes is also a very important factor, which may both accelerate and retard the recrystallization process, and will be further addressed in Section 2.6.4.

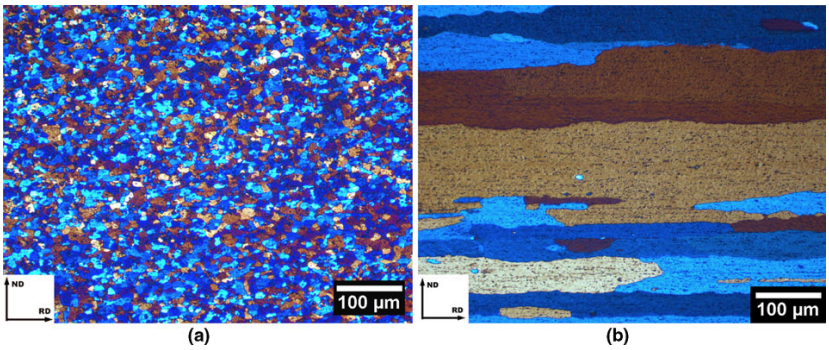

Figure 2.7: *Recrystallized microstucture of an Al-Mn cold rolled to 95 %, and isothermally annealed at a temperature above (a), and below (b) below a critical temperature, T_C.*[48]

2.6.3 Grain growth

Recrystallization lowers the internal energy of the system by removing dislocations, but energy is still stored in grain boundaries within the recrystallized microstructure. The excess energy of the system can be further reduced by decreasing the total grain boundary area, which can occur by grain growth. The driving force for grain growth is much smaller than for recrystallization. A consequence of this is that retarding forces such as drag force exerted by particles and solutes will become more significant than during recrystallization. It must be emphasized that this is not a claim that the effect of particles are higher during grain growth than recrystallization, as precipitation of particles during recrystallization may severely retard recrystallization (a matter that will be addressed in Section 2.6.4. It does however mean that the drag force from solutes and particles will be more significant during grain growth than recrystallization. Restricting grain growth due to pinning by second phase particles and solutes is an effective way to control the final grain size of two phase alloys.[49]

2.6.4 Influence of second phase particles and solutes

Second phase particles and solutes may have a significant impact on recrystallization behaviour. They may retard or accelerate the softening kinetics in several ways, which may affect the development of microstructure and mechanical properties. Some of the most relevant cases will be addressed in this section, and for a more comprehensive review, the reader is referred to this review paper by Huang et. al.[15]

Dispersions of second phase particles exerts a retarding drag force on grain boundaries known as the Smith-Zener drag, or simply Zener drag, which may strongly influence recovery, recrystallization and grain growth.[50,51] The Zener drag is often divided into two parts: The force exerted by a single particle, and the total force exerted by a distribution of particles. Considering the first, the force, F, exerted by a single particle is given as

$$F = 2\pi r\gamma \cos \beta \sin\beta, \tag{2.9}$$

where β is the angle between the boundary and the particle, γ is the specific energy of the boundary, and r is the radius of the particle. This force has a maximum value when $\beta = 45°$, in which case $F = \pi r\gamma$. If a random distribution of particles is present, the total pinning force (i.e. the Zener drag), P_{SZ} can be written as[43]

$$P_{SZ} = \frac{3f_V\gamma}{2r}, \tag{2.10}$$

where f_V is the volume fraction of particles. Pinning due to the Zener drag have shown to be very efficient in limiting recovery processes when the cell or subgrain size is about the same as the distance between the particles.[42] It is important to note that Equation (2.10) is a simplified estimate, assuming a random distribution of particles with the same size. In practice, this is not the case, as two phase alloys contain a distribution of particle sizes which not necessarily are spatially distributed uniformly. For more details regarding adjustments that tries to cope with this, the reader is referred to review papers by Nes[51] and Hillert.[52]

Large second phase particles, > 1 µm, may act as nucleation sites for recrystallization, which is a recrystallization mechanism known as particle stimulated nucleation (PSN). When a two-phase alloy containing such particles is deformed, a deformation zone is created around such particles. For a nucleus to form in the deformation zone, the maximum misorientation in the deformation zone must be high enough to form a high angle grain boundary with the matrix. This can occur through the growth of a subgrain within the deformation zone. The deformation zone contains an orientation gradient, and when a subgrain consumes parts of the deformation zone, the misorientation to other subgrains increases. A potential recrystallization nucleus is said to have formed once the misorientation reaches 10-15°. Recrystallization may proceed with the nucleus consuming the matrix, or it may stop when the nucleus has consumed the deformation zone. As the nucleation involves local recovery processes, the presence of dispersoids may retard this process through the previously described Zener pinning. Thus, dispersoids may play a significant role during recrystallization by restricting the nucleation process in PSN. In addition to dispersoids, the occurence and extent of PSN is affected by the strain, particle size, volume fraction of particles and deformation temperature.[53,54] PSN is an important mechanism which can be used to control the grain size and texture of metals, the latter will be addressed further in Section 2.7.1.

Solutes may also reduce the mobility of grain boundaries, and the effect of the solutes are highly related to the concentration, which can be divided into two regions: High solute concentrations is associated with a high effect of solutes on the boundary migration. This is due to a "solute atmosphere", which limits the migration of boundaries through diffusion processes. At lower concentrations, the effect of the atmosphere has diminished, and the solute concentration has little effect.[55]

2.6.5 Interaction between recrystallization and precipitation

Precipitation and recrystallization in deformed supersatured alloys is a complex matter. The deformed microstructure may affect the precipitation behaviour, and the precipitates may in turn also affect the recovery and recrystallization processes in the material. When such a material is annealed, recrystallization and precipitation may occur alone or simultaneously. This behaviour is often represented in a Time-Temperature-Transformation (TTT)-diagram, e.g. Figure 2.8. The figure is divided into regions I,II, and III. The regions correspond to whether precipitation occurs prior, concurrently or subsequent to recrystallization, respectively.

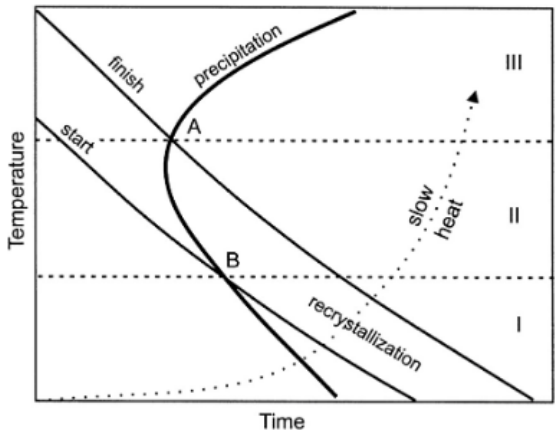

Figure 2.8: *TTT diagram for recrystallization and precipitation in cold rolled supersaturated aluminium alloys, rapidly heated to temperature.*[53]

The TTT diagram is influenced by many factors, such as chemistry and thermomechanical history of the material. This is well illustrated by the experiments of Nes,[56] shown in Figure 2.9. The figure shows how different heat treatments impacts the kinetics of precipitation and recrystallization of an AlMn alloy. Extensive studies have been carried out on effects of the Mn content in 3xxx alloys in terms of softening kinetics, resulting grain structure and texture. Huang et al. showed that the a fine dispersion of both pre-existing dispersoids and concurrent precipitation could slow down the softening kinetics and also influence the resulting grain size and texture.[2] Another paper by Huang et al. states that the degree of concurrent precipitation increases with increased supersaturation of Mn in solid solution.[57]

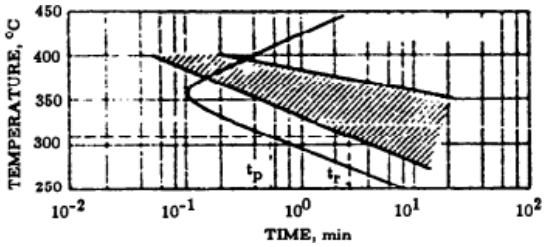

(a) Annealed to 570 °C for 6h.

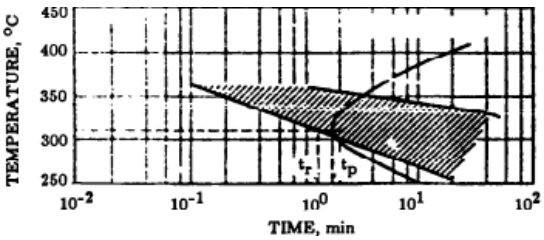

(b) Annealed to 570 °C for 4h, then cooled to 520 °C at a rate of about 100 °C/h, and kept at this temperature for 17h.

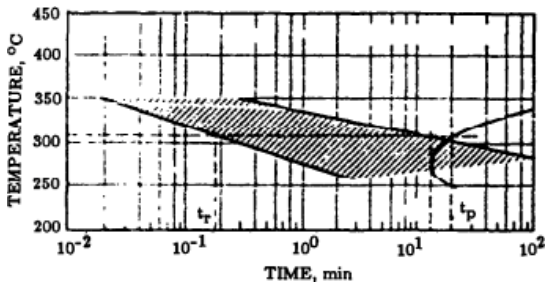

(c) Annealed to 570 °C for 6h, then cooled to 450 °C at a rate of about 100 °C/h, and kept at this temperature for 41h.

Figure 2.9: *TTT diagrams for three chemically identical strip-casted AlMn-alloys, but with different heat treatments prior to 85 % deformation at room temperature. The shaded region indicates the range of recrystallization, and the solid line marks the start of decomposition of the supersaturated Al-Mn matrix.*[56]

2.7 Texture

Crystallographic texture can be defined as the tendency of preferred crystallographic orientations, which is an important feature of thermomechanically processed materials.[58] As described in Section 2.2, the transformation of a cast rolling slab to a thin sheet is done through different and alternating deformation and heating steps, which induces changes in the texture of the material. As many material properties exhibit crystallographic directionality, known as anisotropy, the presence of crystallographic texture may lead to anisotropic properties for the material on a macroscopic level. For rolled metal sheets, this is of particular interest for products that are further processed through forming operations such as deep drawing. Depending on the texture of the rolled sheet, deep drawing may lead to a different degrees of plastic deformation in different directions, known as earing. Earing is an undesirable effect in the processing of e.g. beverage can, as the ears have to be trimmed off, which leads to material loss, and the effect has been studied for a long time.[59]

To define the orientation of a crystal, two coordinate systems must be defined: One coordinate system for the specimen, and one for the crystal structure. For rolled products, the Rolling Direction (RD), Transverse Direction (TD) and the Normal Direction (ND) are orthogonal directions, and are commonly used as the specimen coordinate system. The crystal coordinate system is often selected to fit the crystal symmetry. For instance, in cubic materials, the [100], [010] and [001] directions form an orthogonal frame, and is a convenient choice of crystal coordinate system. To represent the orientation of a crystal with respect to the specimen coordinate system, three rotations are necessary. Many definitions have been proposed, but the rotations proposed by Bunge, displayed in Figure 2.10 is the most commonly used: The rotations are passive, meaning that the specimen coordinate system is rotated to coincide with the crystal coordinate system.

1. A rotation of ϕ_1 about the Normal Direction. The initial directions for RD and TD have been rotated to new directions, RD' and TD', respectively.
2. A rotation of Φ about RD'. ND now coincides with [001], and TD' has been rotated to TD".
3. A rotation of ϕ_2 about ND", making RD' and TD" coincide with [100] and [010], respectively.

Suwas states that a polycrystal "can be considered as an aggregate of single crystals, or grains, where each grain has its own crystallographic orientation".[23] In polycrystals, the distribution of crystallographic orientations of the grains are in most cases not random, as some orientations tend to occur more frequent than others. Such non-random distribution of crystallographic orientations is known as texture.[58] Texture can be divided into macrotexture and microtexture. Macrotexture consideres the average texture of an aggregate, and has traditionally been measured using X-ray diffraction. As advanced characterization techniques such as Electron Backscatter Diffraction have been developed, measuring the crystallographic orientation of individual grains has been made possible. This is the origin of another approach to texture, known as microtexture. Microtexture can be seen as the connection of microstructure and texture, linking microstructural features as the shape, size, and spatial location of grains, to the corresponding crystallographic orientation of the grains.

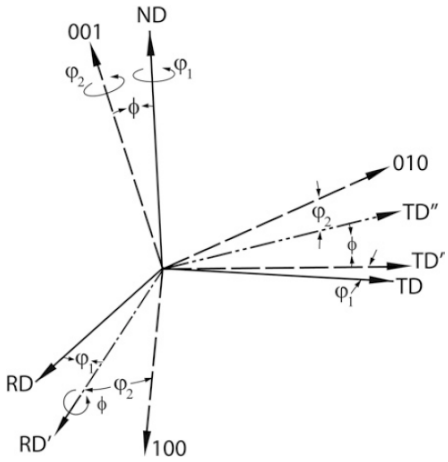

Figure 2.10: *The three Euler angles proposed by Bunge.*[60]

The orientation distribution function (ODF), $f(g)$, can be written as

$$f(g)dg = \frac{\Delta V}{V}, \tag{2.11}$$

where ΔV is the volume of the sample within the orientation spread dg, and V is the total volume of the sample.[58] The ODF is a function of the three Euler angles, hence any crystallographic orientation can be described as a point in the three dimensional Euler space. Visual representation of the ODF can be done in several ways. One approach is taking cross sections at different ϕ_2 sections, and projecting the intensity of $f(g)$ into the Φ-ϕ_1 plane. The intensity of $f(g)$ is represented by contour lines, often accompanied by color levels. Another approach is by evaluating $f(g)$ along characteristic fibers in the Euler space, such as the α and β fiber in FCC metals, shown in Figure 2.11. Fibers are usually defined as a path between two or several texture components, and in most cases, they are fixed in the Euler space. The β fiber is not fixed in Euler space, and runs from Copper $\{112\}\langle 111\rangle$ to Brass $\{011\}\langle 211\rangle$, via the S $\{123\}\langle 634\rangle$ component. Because it is not fixed in Euler space, the fiber is sometimes referred to as a "skeleton line".[23]

2.7.1 Characteristic textures

A consequence of deformation and annealing of metals are characteristic textures. As described in Section 2.4, a rotation of the crystal lattice accommodates the external imposed load as a crystal is deformed by slip. When metals deformed by slip are rolled, the grains will rotate to some preferred orientations, i.e. develop a rolling texture. Typical rolling texture for FCC metals are shown in Figure 2.12a, and the orientation of characteristic texture components are given in Table 2.1. In many FCC metals, the rolling texture is affected by the stacking fault energy, which is typically reduced by alloying elements. If the alloying elements are precipitated as second phase particles, they may affect the deformation behaviour of the material, and in turn also the deformation texture.[58]

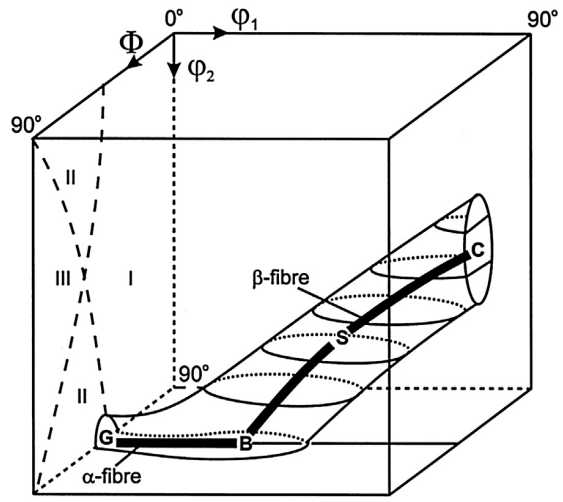

Figure 2.11: *α- and β fibers in the Euler space.*[28]

During rolling of a metal sheet, the texture does not necessarily evolve homogenously through the material. Due to the shear strain caused by friction between the metal and rolls, a shear texture may develop in a layer close to the surface. Factors that may affect the shear strain in this layer are the friction coefficient, rolling speed and geometry, temperature, total reduction and initial thickness among others.[61]

Table 2.1: *Texture components in deformed FCC metals.*[28]

Component, symbol	$\{hkl\}$	$\langle uvw \rangle$	$\varphi_1[°]$	$\Phi[°]$	$\varphi_2[°]$
Copper, C	112	111	90	35	45
S	123	634	59	37	63
Goss, G	011	100	0	45	90
Brass, B	011	211	35	45	90
Cube	001	100	0	0	0
Dillamore	4,4,11	11,11,8	90	27	45

When the deformed metal is annealed, the deformation texture is further developed into a recrystallization texture. For FCC metals, the recrystallization texture is more complex than the deformation textures. The recrystallization texture is determined by the orientation of new, recrystallized grains and their subsequent growth. The nuclei of the new grains are restricted to the orientations already present in the structure. Hence, the recrystallization texture is a result of preferred nucleation and/or growth of orientations in the deformed structure, and is typically a mixture of weak remaining deformation texture and texture developed from nucleation and/or growth preferences. Typical recrystallization textures for FCC metals are displayed in Figure 2.13.[13,64,65]

In two-phase alloys like 3xxx-alloys, the second phase particles may affect the recrystallization

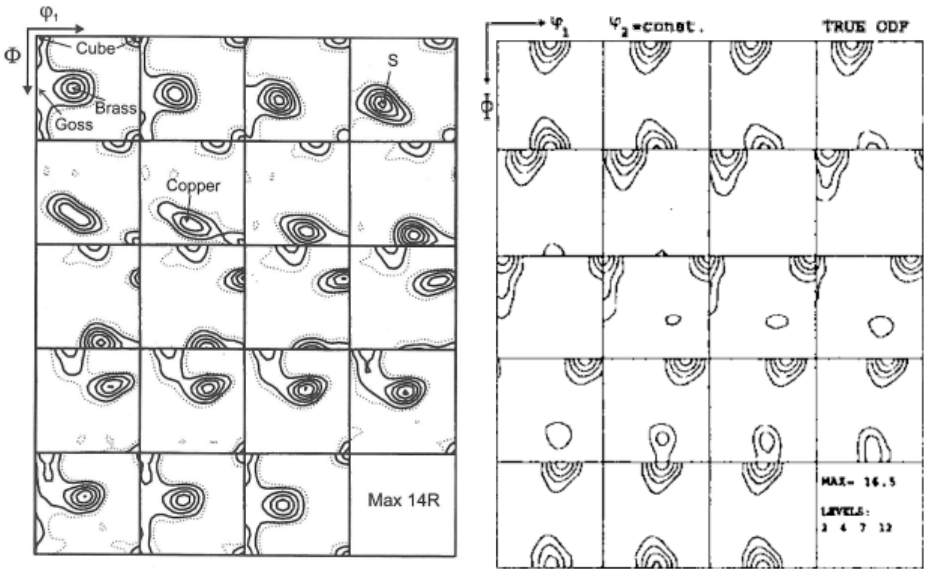

(a) 90 % cold rolled aluminium[62] *(b) AA3003-alloy rolled with no lubricant, close to surface*[63]

Figure 2.12: *ODFs showing deformation textures in FCC-metals. a) classic rolling texture b) shear texture.*

texture. As discussed in Section 2.6.4, large second phase particles may act as nucleation sites for new grains. The orientations of the PSN grains are restricted to the orientations in the deformation zone around the particles. For heavily deformed polycrystals, PSN is associated with a weak recrystallization texture, with some presence of the P component and Cube component rotated 20-25° about the normal direction of the rolled sheet. Thus, the recrystallization texture is highly affected by the extent of PSN, which in turn depends on the presence of large particles. The extent of recrystallization through PSN is also dependent on temperature and strain rate, and tends to increase as the deformation temperature decreases and the strain rate increases.[64]

The influence of particles that are not large enough for PSN also affects the recrystallization texture. The presence of particles that are not large enough for PSN alone, increases the critical nucleus size through the Zener drag exerted by the particles. This promotes SIBM, which may assist the growth of the cube texture from existing cube bands.[67] If both small and large particles capable of PSN are present prior to recrystallization, the Zener drag from the smaller particles will increases the critical nucleus size, and decrease the number of possible nucleation sites for PSN. The tendency of a more random texture which comes with PSN compared to other recrystallization mechanisms, decreases. Still recrystallization through SIBM is possible, and a stronger cube texture is observed. Particles that precipitate simultaneously with recrystallization, i.e. concurrent precipitation, has shown to significantly affect the recrystallization texture in AlMn alloys, by promoting P- and ND-rotated cube texture, at the expense of the Cube texture.[48,68,69]

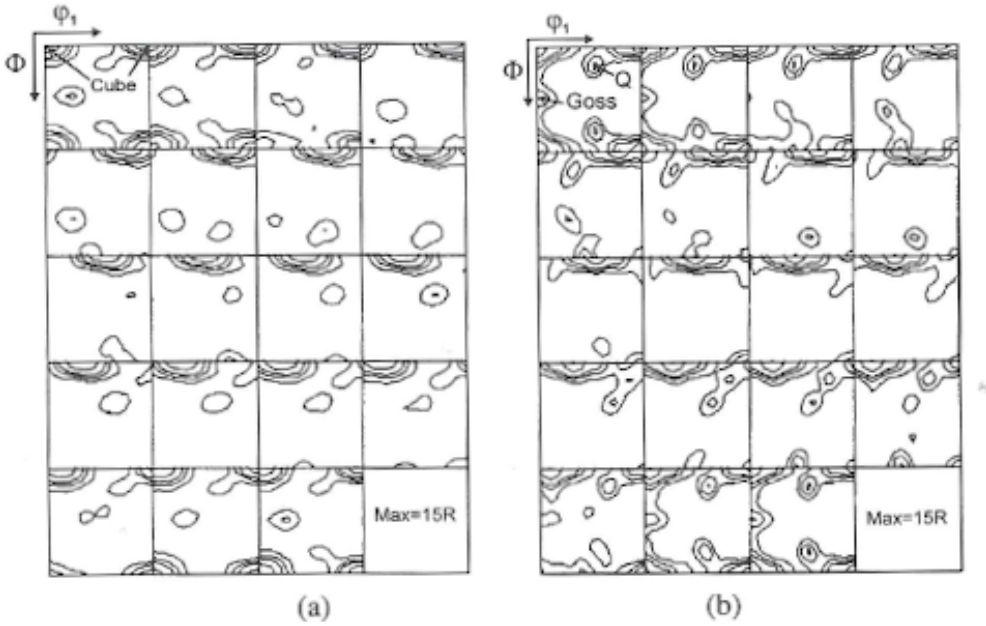

Figure 2.13: *Recrystallization textures in an Al 3%Mg alloy with prior a) 90 % reduction b) 97.5 % reduction.*[66]

Table 2.2: *Texture components in recrystallized FCC metals.*[64]

Component, symbol	{hkl}	⟨*uvw*⟩	φ_1[°]	Φ[°]	φ_2[°]
Cube	001	100	0	0	0
CubeND	001	310	22	0	0
-	236	385	79	31	33
Goss, G	011	100	0	45	90
S	123	634	59	37	63
P	011	122	70	45	0
Q	013	231	58	18	0
R (aluminium)	124	211	57	29	63

2.8 Electron Backscatter Diffraction

Electron backscatter diffraction (EBSD)[70] is a characterization technique that has, among other techniques, allowed a rapid and precise method for microtexture measurements. A typical experimental setup of EBSD measurements is shown in Figure 2.14. A 70° tilted sample is bombarded by an electron gun. For electrons to be diffracted by crystal planes where the gun is focused, the crystal planes must fulfill Bragg's law, which is given as

$$n\lambda = 2d\sin\theta, \tag{2.12}$$

where n is the order of diffraction, λ is the wavelength of the incident electrons, d is the interplanar spacing and θ is the diffraction angle between a particular crystal plane and the incident electrons. Crystal planes that fulfill Bragg's law may be diffracted, and appear as Kikuchi diffraction patterns on a phosphorous screen. The pattern consists of diffraction lines from individual crystal planes, which may be used to identify the phase and crystallographic orientation of the area or grain where the beam is focused.The process of matching the experimental pattern to reference patterns is known as indexing. Indexing of Kikuchi patterns is usually done via the Hough transform, although other approaches as dictionary indexing have shown good performance when conventional indexing via the Hough transform struggles with noisy patterns.[71] Nevertheless, the Kikuchi bands can be represented by a perpendicular distance from a reference axis, ρ, and the angle between the band and the reference axis, θ. This way, the Kikuchi bands can now be represented by cartesian coordinates in the Hough space, given by the equation

$$\rho = x\cos\theta + y\sin\theta. \tag{2.13}$$

The Hough transformation simplifies the matching of the Kikuchi patterns to reference patterns. When a pattern has been successfully indexed, the crystallographic orientation and the phase of the material have been determined. This process can be done iteratively over a given specimen area, mapping the phase(s) and crystallographic orientation within the area. However, a trade-off between good statistics in terms of a large scan area and good spatial resolution has to be done, as such measurements are both time and data consuming.[58]

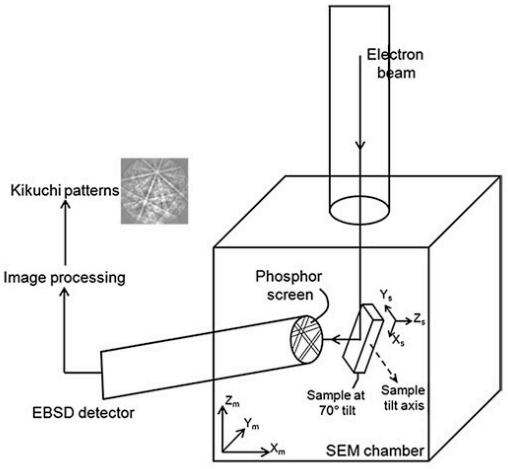

Figure 2.14: *Experimental setup of EBSD measurements.*[23]

3 | Experimental

3.1 Delivered material

Two nearly identical AA3005 alloys with different Mn content were delivered by Hydro Holmestrand, containing 1.11% and 1.33% Mn. Both alloys were delivered with two identical parallels, except for the cooling rate from hot deformation to room temperature. The first parallel were cooled using a fan, i.e. forced convection, while the second parallel were cooled naturally at room temperature. The first and second parallel has been labeled *"Fan"* and *"Air"*, respectively. Thus, four different materials have been studied, labeled as follow: *1.11 - Air*, *1.11 - Fan*, *1.33 - Air* and *1.33 - Fan*, where the first part of the label marks the Mn content in %. Samples from the four materials were taken both after hot deformation and cold deformation. These material states will from here be labeled as "Hot deformed" and "As deformed", respectively. Due to unfortunate circumstances, the "As deformed" samples from the 1.11-material were taken prior to the last rolling step of the cold deformation. As a consequence, the last rolling step was carried out at NTNU Trondheim, for these materials. The chemical compositions of the four materials are shown in Table 3.1.

Table 3.1: *Chemical content in the investigated materials in wt.%.*

	Al bal.	**Si**	**Fe**	**Cu**	**Mn**	**Mg**	**Cr**	**Zn**	**Ti**
1.11 - Fan	-	0.42	0.56	0.17	1.11	0.40	0.021	0.059	0.017
1.11 - Air	-	0.42	0.56	0.17	1.11	0.40	0.021	0.059	0.017
1.33 - Fan	-	0.43	0.53	0.17	1.33	0.38	0.019	0.053	0.018
1.33 - Air	-	0.43	0.53	0.17	1.33	0.38	0.019	0.053	0.018

3.2 Material processing

Figure shows the process route at the rolling mill at Hydro Holmestrand. The materials in this work was Direct Chill-casted to a rolling slab, which was then prepared for rolling by sawing and milling, into a 314 mm thick rolling slab. The slabs were then pre-heated, prior to being hot rolled to coils with a thickness of 4.5 mm. Data for the pre-heating and hot rolling are displayed in Table 3.2.

Subsequent to the hot deformation, all materials rested at least 2 days and 5 hours prior to cold rolling. The materials were cold deformed from 4.5 to 0.87 mm by three rolling sequences,

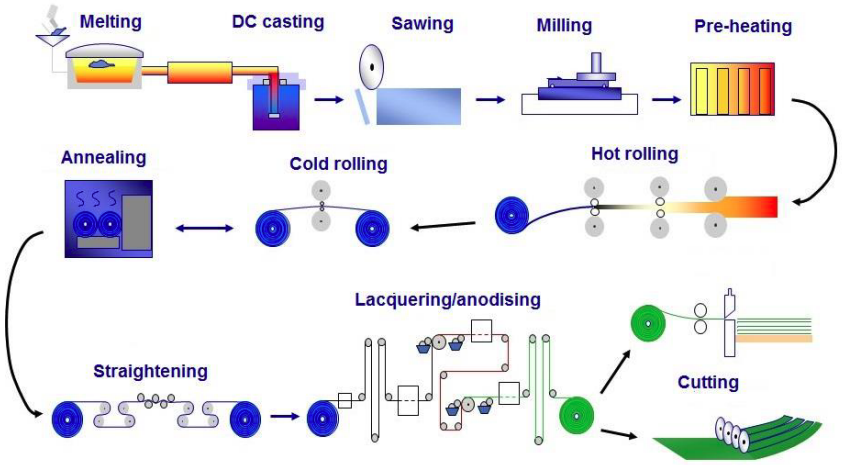

Table 3.2: *Data for pre-heating and hot rolling.*

	Pre-heating temperature [°C]	Pre-heating time [h]	Temperature after hot rolling [°C]
1.11 - Fan	570	12.57	325
1.11 - Air	572	11.55	322
1.33 - Fan	564	10.85	314
1.33 - Air	570	11.20	327

or breakdowns.

3.3 Vickers hardness test

Vickers hardness testing was used to measure the hardness of the investigated materials. Prior to the measurements, the samples were grinded down to 4000 grit. The hardness measurements were carried out using an Innovatest manual hardness testing machine. A dwell time of 10 s and a load of 1 kg was used. For all measurements, ISO 6507 was complied.[72] For light metals as aluminium, the minimum distance between indentations should be at least six times the mean diagonal length of the indentation. The distance between indentations and the edge of the sample should be at least three times the mean diagonal length of the indentation. The standard also states a requirement of a minimum thickness of the sample, based on the hardness of the material. The lowest value measured hardness value in this study was 42 HV1. A hardness of 40 HV1 gives a thickness requirement of 0.33 mm. This was fulfilled for all samples, as the thinnest sample was measured to 0.66 mm.

3.4 SEM sample preparation

The samples were cold mounted in an epoxy consisting of Epofix Resin and Epofix Hardener. After the epoxy was cured, the samples were grinded and polished using the polishing program displayed in Table 3.3. The program was carried out with a Struers Tegramin-30 polishing machine. In between the polishing steps, the samples were rinsed in water and cleaned with dishwasher liquid and a cotton piece, before a final rinse with ethanol. After polishing with OP-S NonDry, the samples were washed and rinsed as before, except without dishwashing liquid, as the liquid contained abrasives.

Table 3.3: *Metallographic sample preparation prior to SEM*

Disc/paper	Suspension	Lubricant	Time
SiC Foil #320	-	Water	2:00
Largo	DiaPro Allegro Largo 9	-	3:00
Mol	DiaPro Mol3	-	4:00
Nap	Nap-R1	-	5:00
Chem	OP-S NonDry	-	1:00

3.5 Electron Backscatter Diffraction

Electron Backscatter Diffraction (EBSD) was used to analyze the micro- and macrotexture and microstructure of the materials. The sections below will describe the data acquisition and the methods used to analyze the mentioned features of the materials. All processing and analysis of the orientation data were carried out using the MTEX MATLAB Toolbox.[8]

3.5.1 Data Aquisition

Acquisition of the EBSD data was carried out with a Zeiss Ultra 55 Field Emission SEM and a NORDIF UF-1100 detector. Measuring macro- and microtexture has different requirements for data acquisition. The macrotexture is an average texture for the material, that does not take into account the location of individual grains. The microtexture, on the other hand, links the microstructural features such as grain size and shape, to the crystallographic orientation of that given grain.[58] Macrotexture measurements are carried out at a rather large area of the sample, large enough to encompass a significant number of grains (several hundreds) to ensure that the measured texture is representative for the sample. The microtexture depends on high enough spatial resolution to display the microstructural features of the investigated area. Hence, the step size has to be much lower. In theory, both measurements could be done simultaneously, scanning a large area while using a small step size. However, this would be very data- and time consuming, hence separate scans are preferred. Considering microtexture analysis, it is desired to study a certain number of grains to ensure statistical significance. Samples with larger grain size thus requires a larger scan area to achieve the same number of grains as a sample with lower grain size. In this work, both deformed aluminium and recrystallized aluminium are studied. As the recrystallized grains are larger than the grains in the deformed material, it follows that a larger scan area is needed for these materials. In order to perform Hough Indexing, it is

necessary to know the position of the pattern centre of the acquired patterns on the detector. This is done using a few calibration patterns with higher resolution than the rest of the dataset. The calibration patterns are indexed via the Hough transform, and the resulting pattern centre is used for indexing the rest of the dataset. As a consequence, different settings are used for the calibration patterns and the rest of the dataset. These settings are displayed under *Calibration settings* and *Acquisition settings*, respectively, in Table 3.4, along with other settings used to acquire EBSD data.

Table 3.4: *Settings used for acquisition of EBSD-data*

	Hot deformed		As deformed, Recovery, Partly RX		Fully RX	
	Micro	**Macro**	**Micro**	**Macro**	**Micro**	**Macro**
Tilt angle	70°	70 °	70°	70 °	70°	70 °
Acc. voltage	17 kV	17 kV	17 kV	17 kV	17 kV	17 kV
Working distance	20.6 - 25 mm	24.9 - 25.1 mm	23.9 - 25 mm	23.2-25.1 mm	22.4-25 mm	22.4 - 24.9 mm
Scan area	76 x 76 µm	500 x 500 µm	61 x 61 µm	303 x 303 µm	200 x 200 µm	303 x 303 µm
Step size	0.091 µm	1.0 µm	0.091 µm	0.606 µm	0.30 µm	0.606 µm
Acquisition settings						
Frame rate	120 - 130 fps	70 fps	65 - 75 fps	70 - 75 fps	70 - 75 fps	70 75 fps
Resolution	80x80 px	96x96 px	96x96 px	96x96 px	96x96 px	96x96 px
Exposure time	7642 - 8283 µs	14235 µs	13283 - 15334 µs	13283 - 14235 µs	13283 - 14235 µs	13283 - 14235 µs
Gain	0	0	0	0	0	0
Calibration settings						
Frame rate	40 - 60 fps	25 fps	22 - 40 fps	24 - 45 fps	25 fps	25 fps
Resolution	160x160 px	160x160 px	160x160 px	160x160 px	160x160 px	160x160 px
Exposure time	16616 - 24950 µs	39950 µs	24950 - 39950 µs	22172 - 41616 µs	39950 µs	39950 µs
Gain	2 - 5	0	0 - 3	0 - 3	0	0

3.5.2 Indexing

Prior to indexing, the raw EBSD patterns were processed using the Kikuchipy open source Python library.[73] Static and dynamic background were subtracted from the patterns. Subsequently, the patterns were neighbor pattern averaged, using a Gaussian filter.[71] For details, the reader is referred to the script "kik.py" in the GitHub repository of the author.[74] The processed patterns were Hough indexed using the TSL OIM Data Collection 7 software, via the Hough transform, described in Section 2.8.

3.5.3 Post-processing of orientation data

The indexed EBSD data, i.e. the orientation data, were analyzed using the MATLAB toolbox MTEX. The algorithm for the filtration of the raw data is shown schematically in Figure 3.1. The orientations data of the macrotexture measurements was filtred by a treshold for image quality (IQ). The treshold was manually set by comparing the removed orientation data with secondary electron (SE) imaging of the scan area, and by selecting a filter value that gave the best match between the removed orientation data and the second phase particles in the SE image.

The orientation data of the microtexture measurements were filtred by the same method described above. The filtred orientation data was used to reconstruct grains,[75] using a misorien-

tation threshold of 2°. Grains with a size < 10 px was, in addition to not indexed pixels with a ratio < 0.25 of total pixels/boundary pixels, removed. Finally, grains was reconstructed again, using the same misorientation treshold, 2°.

For the complete scripts used to filtrate the orientation data and reconstruct grains (only for microtexture), the reader is referred to the scripts "macrotexture.m" and "microtexture.m" in the GitHub repository of the author,[74] which are modified scripts from code provided by Håkon Wiik Ånes.[76]

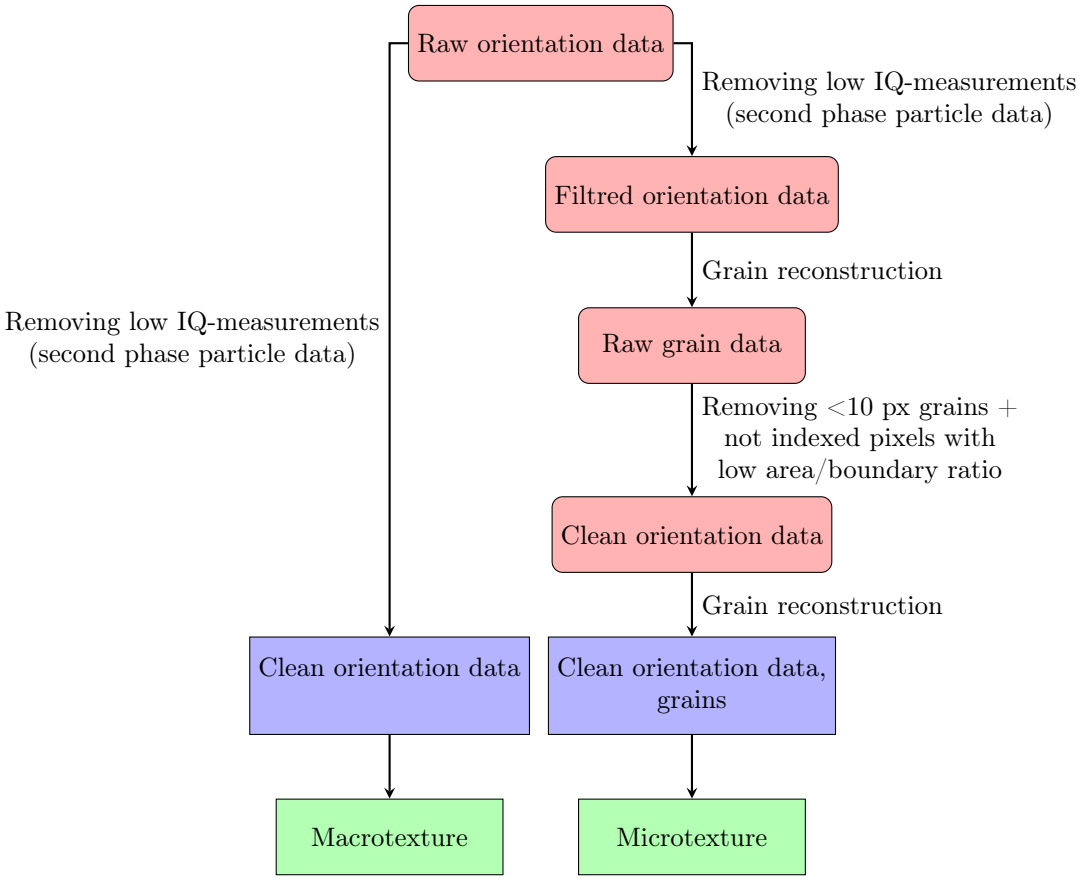

Figure 3.1: *Schematic representation of the processing from the raw orientation data to the filtered orientation and grain data used in the analyzes of micro- and macrotexture.*

3.6 Macrotexture Analysis

To visualize the macrotexture of the materials, Orientation Distribution Functions (ODFs) were calculated from the filtered orientation data, using MTEX. The calculation of the ODFs were done using the "calcDensity" function,[77] using a de la Vallée Poussin kernel with halfwidth = 5° and a resolution of 5°. From the ODFs, sections at $\phi_2 = 0$, 45 and 65 ° were plotted, as these sections were assumed to include the main texture components of interest. All plots used

the same contour levels and color range for the plots, which was (0, 2, 4, 6, 8, 10, 15, 20, 25, 30) and (0,30), respectively. To compare the development of the rolling texture between the investigated materials, the ODFs were evaluated along the β fiber, which runs from Cu to Br, via the S component, as described in Section 2.7.

For the complete script used in the macrotexture analysis, the reader is referred to the script "macrotexture.m" in the GitHub repository of the author.[74]

3.7 Microtexture Analysis

3.7.1 Orientation Distribution Function

From the filtred orientation data, ODFs were calculated as described above.

Orientation mapping. Orientation maps were plotted from the filtered EBSD- and grain data, described in Section 3.5.3. The orientation maps were plotted with respect to the rolling direction (RD), using the inverse pole figure key shown in Figure 3.2 .

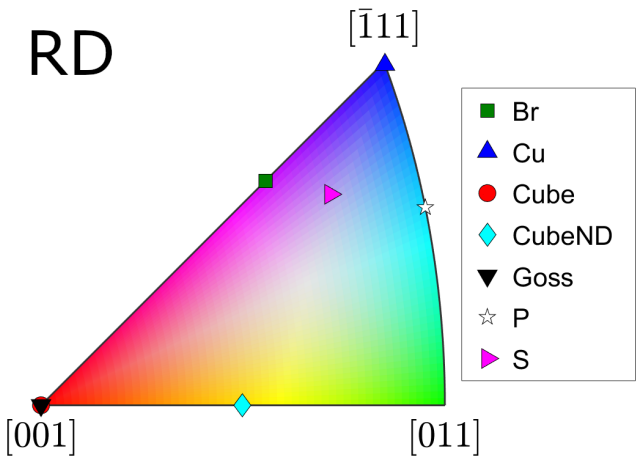

Figure 3.2: *Inverse polefigurekey used for the orientation maps, annotated with relevant texture components from Table 2.1 and 2.2.*

Classification of grains. In the present work, grains were classified as one of the following grain types: Original grains (OG), subgrains (Sub) and recrystallized (RX) grains. The grain orientation spread (GOS) criteria used in this work is taken from,[78] and modified to the experimental data in this work. The previously reconstructed grains (described in Section 3.5.3) were classified as follows:
For a grain to be classified as recrystallized, it has to fulfill all criteria below:

i. Fraction High Angle Grain Boundary > 0.5
ii. Grain Orientation Spread (GOS) < 2.7 °
iii. ECD > 3 µm

For a grain to be considered as an original grain (OG), it has to fulfill all criteria below:

i. Grain Orientation Spread (GOS) > 2.7 °

All other grains were classified as subgrains.

Grain size. The grain sizes were described using Equivalent Circular Diameter (ECD), which is the diameter of a circle containing the measured area of the grain. ECD is given as

$$d_{ecd} = 2f_s\sqrt{\frac{n_{px}\Delta x^2}{\pi}}, \tag{3.1}$$

where f_s is the shape factor set to 0.816,[58] n_{px} is the number of pixels inside of the grain and Δx is the step size for the acquisiton. The area weighted average grain size for grain class c were calculated by

$$\overline{d}_{ecd,c} = \frac{\sum_{i=1}^{n}(d_{ecd,c,i} \cdot A_{c,i})}{\sum_{i=1}^{n} A_{c,i}}, \tag{3.2}$$

where c is the class of grains (i.e. subgrains, RX-grain, or original (OR) grains), n is the number of grains of class c in the measurement, $d_{ecd,c,i}$ and $A_{c,i}$ is the equivalent circular diameter and area of grain i, respectively. For further details, the reader is referred to the complete MATLAB-script "microtexture.m" in the GitHub repository of the author.[74]

3.8 Second phase particle analysis

The second phase particles have been analyzed using Backscatter Electron (BSE) imaging, using a Zeiss Ultra 55 Field Emission SEM and a Four Quadrant Backscatter Electron Detector Type 212/U, made by K.E. Developments. The settings used for BSE imaging are displayed in Table 3.5.

To separate the second phase particles from the Al matrix, the BSE images was processed using the Robust Automatic Treshold Selection (RATS) algorithm[79] in the image processing software

Table 3.5: *Settings used for BSE-imaging of second phase particles*

Acc. voltage	5 kV
Aperture	120 µm
Working distance	10 mm
Magnification	500X/4500X

ImageJ/FIJI.[9] RATS computes a treshold map for 2d images based upon the value of pixels and their gradients. The default settings in the algorithm was used, displayed in Table 3.6

Table 3.6: *Default settings in the RATS algorithm, used for tresholding of BSE-images in the analysis of second phase particles*

Noise treshold	25
Lambda factor	3
Min. leaf size	414
Verbose	False

Subsesquent to the separation of the matrix and the second phase particles, the latter was analyzed in FIJI/ImageJ:

To distinguish between dispersoids and constituents particles, a treshold must be set. To the author's knowledge, the size range of dispersoids is not clearly defined, as upper limits ranging from 300-1000 nm have been used in other work.[10,80–82] In this study, a treshold of an ECD of 1 µm has been used to separate dispersoids and constituent particles. A requirement that all dispersoids must contain at least four pixels were also used in the analysis. Hence, particles with ECD 0.036 - 1 µm were classified as dispersoids, and all particles larger than 1 µm were classified as constituent particles.

3.9 Isothermal annealing experiments

The cold rolled materials were isothermally back-annealed in a salt bath at 315 °C, at annealing times ranging from four seconds to 5000 seconds. At the end of the annealing, the samples were water quenched. First, samples for measuring Vickers hardness and electrical conductivity was carried out. Based on the back-annealing curve for these properties, annealing times were selected for a smaller scale annealing experiment used for tensile testing. The annealing times used in both experiments are presented in Table 3.7.

Table 3.7: *Annealing times for isothermal annealing experiments. Normal text denotes annealing experiments used for measuring Vickers Hardness and electrical conductivity. Bold and highlighted text denotes annealing times used for tensile testing in addition to the mentioned measurements.*

Annealing time
As deformed
4 s
9 s
20 s
60 s
134 s
201 s
300 s
433 s
634 s
900 s
3000 s
5000 s

3.10 Electrical conductivity

The electrical conductivity of the materials was measured with a Sigmatest 2.069 eddy current instrument. For each sample, 20 measurements were taken. In order to obtain reliable results, the thickness of the samples must be at least three times the effective penetration depth, d_{eff}, which is given as

$$d_{eff} = \frac{503}{\sqrt{f\sigma}}, \tag{3.3}$$

where f is the frequency [Hz] used in the measurements, which was set to 960 kHz, and σ is the conductivity [MS/m] of the specimen.

A relation between elements in solid solution, particles and electrical conductivity, EC, is according to Altenpohl[83]

$$\frac{1}{EC} = 0.0267 + 0.032Fe\% + 0.033Mn\% + 0.0068Si\%. \tag{3.4}$$

It follows from Equation (3.4) that the contribution on the EC from Si is much lower than from Mn. As it previously has been shown that almost all Fe is present in particles in DC cast 3xxx alloys,[84] %Mn can be estimated from (3.4), by neglecting the contrbution from Fe and Si in solid solution.

3.11 Tensile testing

Because tensile testing is the conventional method for characterization of mechanical properties at Hydro Holmestrand, a smaller scale annealing experiment was also carried out, as data from tensile testing would be easier to compare to Hydro's own test data. A Subsequent to the annealing experiments, specimens for tensile testing were machined at the mechanical engineering workshop at NTNU. The geometry of the machined specimens are showed in Figure 3.3. Tensile testing were carried out using a 100 kN MTS 810 Hydraulic tensile testing machine with a strain rate of 1.80 mm/min. For each annealing time and material, four specimens were tested.

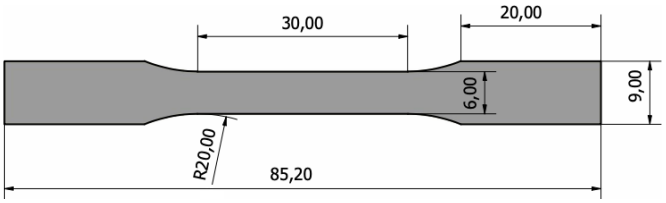

Figure 3.3: *Geometry of the machined specimen for tensile testing. All measurements are given in mm.*

4 | Results

In this chapter, results providing a thorough overview of the development of texture, microstructure, mechanical properties and dispersoid characteristics of the materials will be presented. As mentioned in Section 3.9, some measurements were carried out only on selected annealing times during back-annealing of the "As deformed" state. For practical reasons, these annealing times have been labeled corresponding to their degree of softening. The labels are presented in Table 4.1 and annotated in Figure 4.3.

Table 4.1: *Labeling of material states and their respective processing history.*

State	Material history
Hot deformed	Hot deformed
As deformed	Hot deformed + cold deformed
Recovery	As deformed + 9 sec annealing at 315 °C
Partly RX	As deformed + 201 sec annealing at 315 °C
Fully RX	As deformed + 5000 sec annealing at 315 °C

For clearance, the labels of the materials previously defined in Section 3.1 are repeated in Table 4.2.

Table 4.2: *Labeling of the investigated materials.*

Label	Mn content [wt%]	Cooling condition
1.11 - Fan	1.11	Fan
1.11 - Air	1.11	Air
1.33 - Fan	1.33	Fan
1.33 - Air	1.33	Air

4.1 Mechanical properties and electrical conductivity

To investigate the mechanical properties of the studied materials, hardness measurements and tensile testing was carried out. Data from tensile testing conducted by Hydro is also included for comparison, as this is the preferred method for measuring mechanical properties at Hydro. From the tensile testing, yield strength (YS) and ultimate tensile strength (UTS) will be presented.

4.1.1 Hot deformed material

Hardness and electrical conductivity measurements for the materials in the "Hot deformed" state are presented in Figure 4.1a and 4.1b, respectively. The hardness measurements reveal higher hardness for *Air* than *Fan*. The electrical conductivity measurements display an opposite trend, where *Fan* exhibits higher electrical conductivity than *Air*. Although the mentioned trend was observed, the standard deviation of the measurements was quite high, especially for *1.33*.

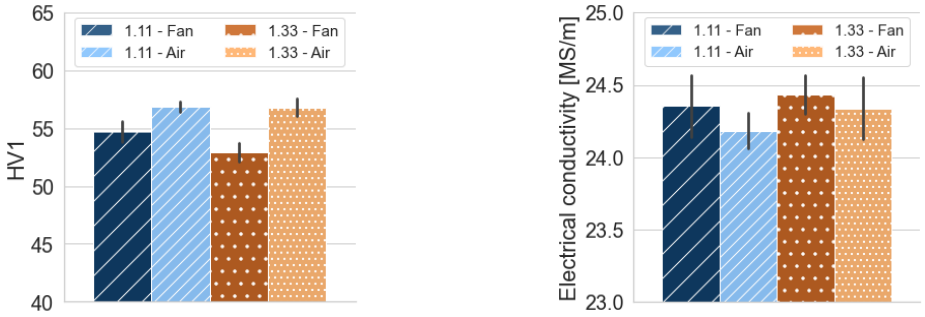

(a) *Hardness measurements*

(b) *Electrical conductivity*

Figure 4.1: *Hardness and electrical conductivity measurements of the hot deformed material. Error bars are plotted with one standard deviation.*

4.1.2 Estimate of Mn_{SS}

Estimates of the concentration of Mn_{SS} in the "Hot deformed" and "Fully RX" state are shown in Figure 4.2. It can be seen that the initial content of Mn_{SS} is very similar for the materials in the "Hot deformed" state, and that no significant differences can be observed. In the "Fully RX" state, the Mn_{SS} is general lower than in the "Hot deformed" state. A larger decrease is observed for 1.11 - Fan.

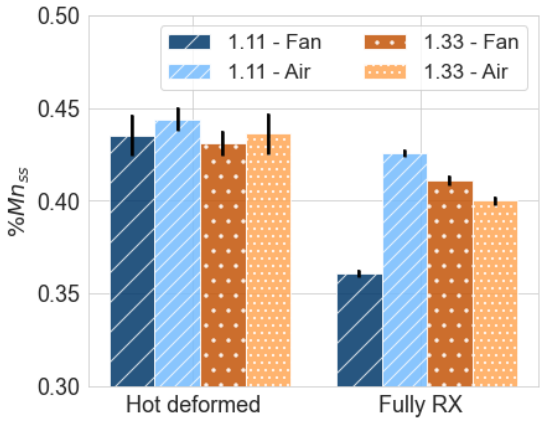

Figure 4.2: *Estimated wt% of Mn in solid solution, calculated from electrical conductivity measurements, after Equation* (3.4).

4.1.3 Back-annealing of "As deformed" material

The response of back-annealing of the "As deformed" in terms of HV1 and electrical conductivity is displayed in Figure 4.3. For both 1.11 and 1.33, the parallel with the highest hardness also displays the lowest electrical conductivity. For 1.11, Air trends to have a higher hardness, whereas Fan is the strongest parallel for 1.33. Considering the kinetics of the back-annealing, the shape of the hardness and electrical conductivity curves are similar for Air and Fan at 1.11. For 1.33, the softening proceeds faster for Air than Fan, with a corresponding increase in electrical conductivity, as indicated with circles in Figure 4.3b .

YS and UTS for the materials in the "As deformed" state and during back-annealing are presented in Figure 4.4a and 4.4b, respectively. For the 1.33 materials, the trend is that YS and UTS are higher for Fan, whereas the 1.11 material exhibits the highest strength for Air.

Mechanical properties determined from tensile tests conducted by Hydro are presented in Figure 4.5. The tested materials was processed as the "As deformed" material in the study, with a subsequent annealing at 218-224 °C for three hours. The tensile tests from Hydro reveals higher YS and UTS for Fan compared to Air. For the 1.11 materials the difference is $\sim$ 5 MPa, while $\sim$ 10 MPa for the 1.33 materials.

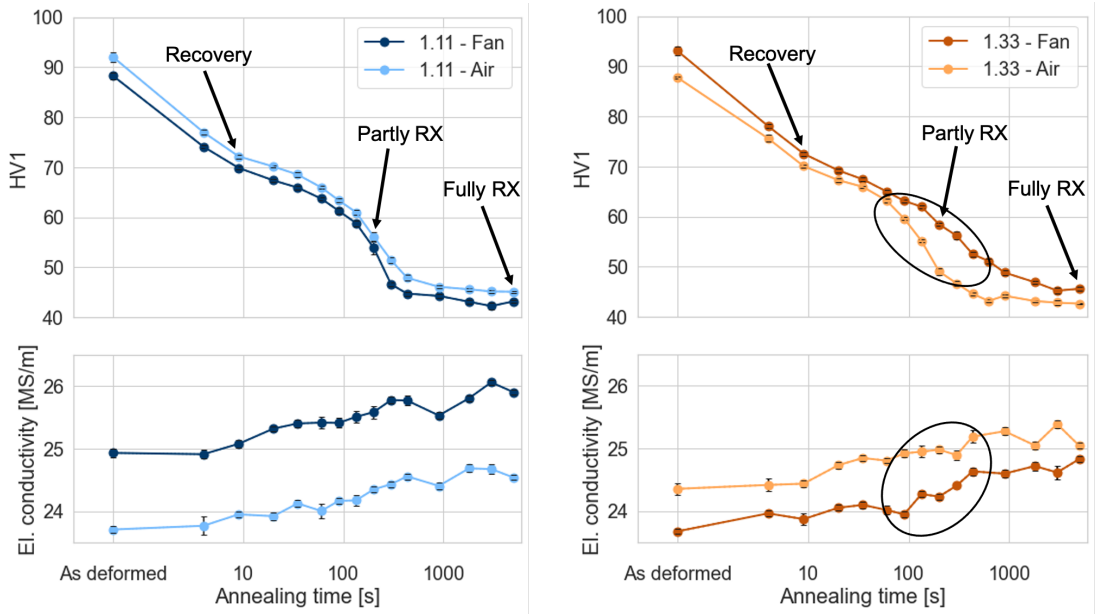

(a) 1.11 - Mn *(b) 1.33 - Mn*

Figure 4.3: *Hardness (upper) and electrical conductivity (lower) measurements as a function of annealing time at 315 °C.*

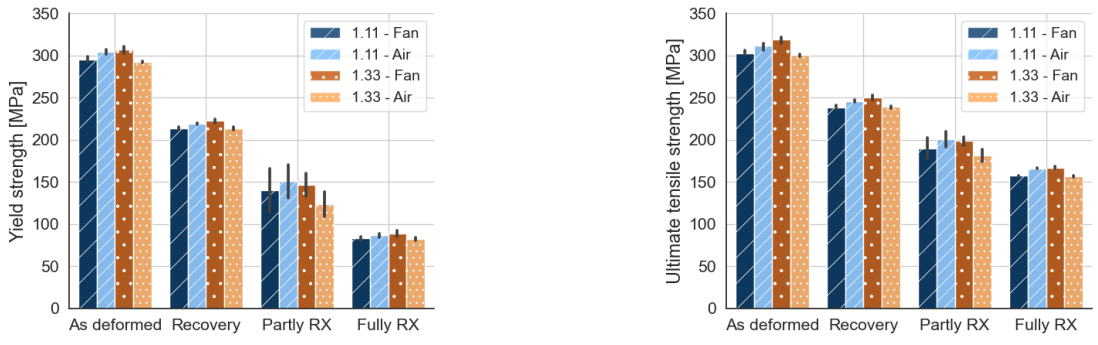

(a) Yield strength *(b) Ultimate tensile strength*

Figure 4.4: *Mechanical properties measured at NTNU.*

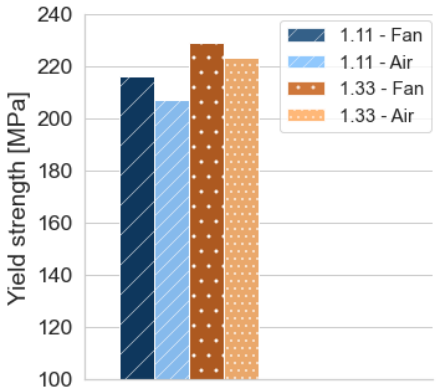

(a) Yield strength

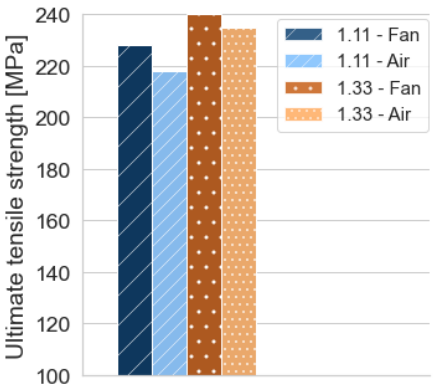

(b) Ultimate tensile strength

Figure 4.5: *Mechanical properties of "As deformed" material, annealed at 218-224 °C for three hours. The testing of these material was conducted by Hydro.*

4.2 Microstructure

4.2.1 Orientation maps

Hot deformed

The orientation maps of the hot deformed materials are presented in Figure 4.6. The microstructures consist of larger, microbands, which are elongated in the rolling direction, and substructures within these microbands. Both the size of the microbands and how well-developed the substructures are, differ between the materials. For *1.11*, *Air* seem to be display a more developed substructure than *Fan*. Larger, recrystallized grains are also observed for *Fan*, in both *1.11* and *1.33*. Considering microtexture, the materials all display a mixture of Brass (purple), S (light purple) and Cu (blue), although the distribution of these components varies.

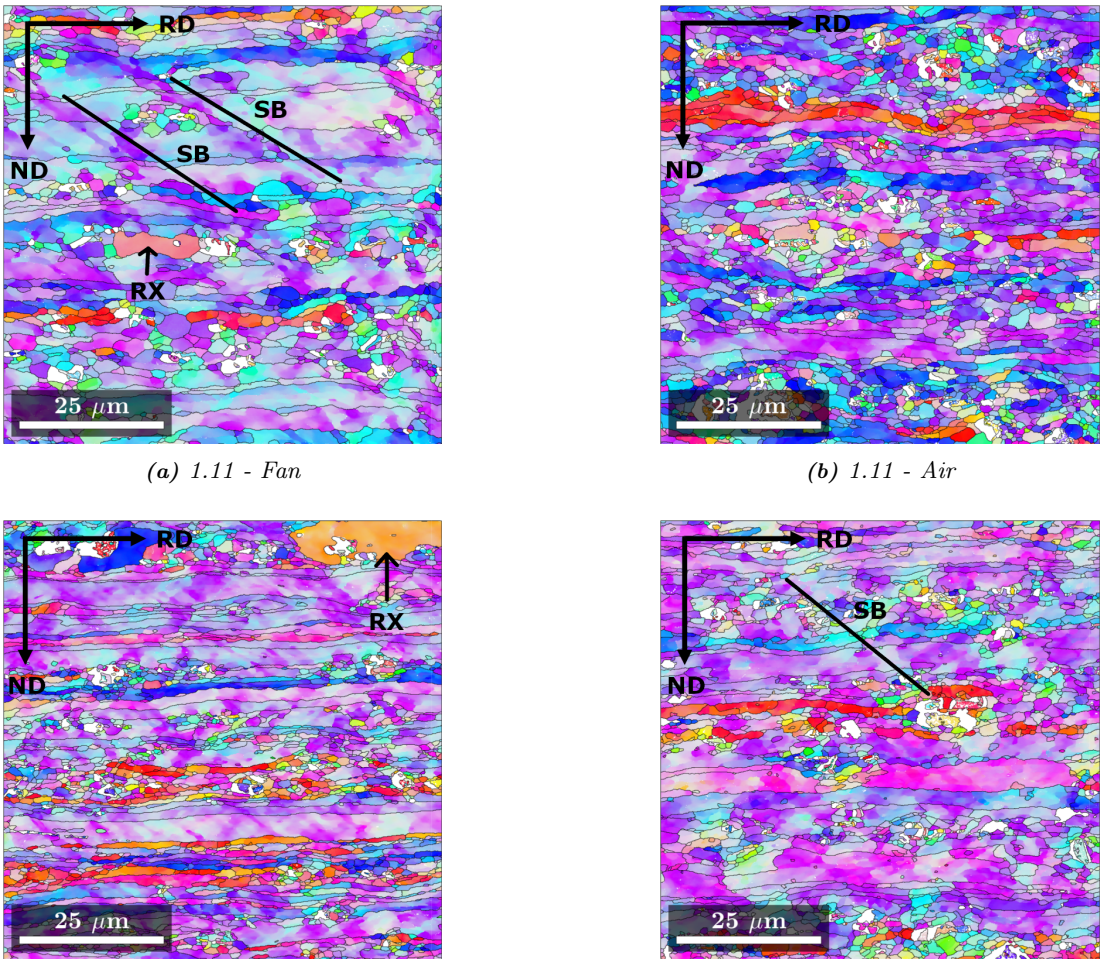

(a) 1.11 - Fan

(b) 1.11 - Air

(c) 1.33 - Fan

(d) 1.33 - Air

Figure 4.6: *Orientation maps for the hot deformed materials from the center of the coil.*

As deformed

Orientation maps for the "As deformed" materials are presented in Figure 4.7. The microstructure previously observed in the hot deformed material is now more elongated and pancake-shaped. More pronounced shear bands have developed, which are marked in the figure. Similar to the hot deformed materials, Br-, S- and Cu-texture is also observed in the "As deformed" state, though the distribution of these components appears to be more homogenous in the "As deformed" state.

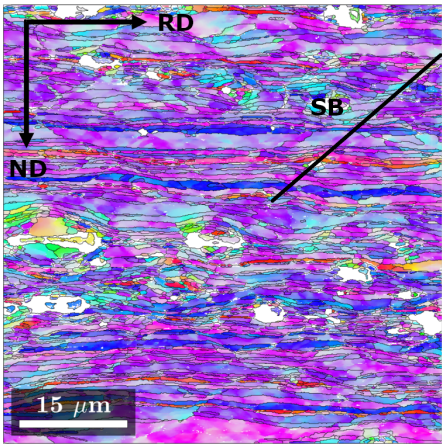

(a) 1.11 - Fan

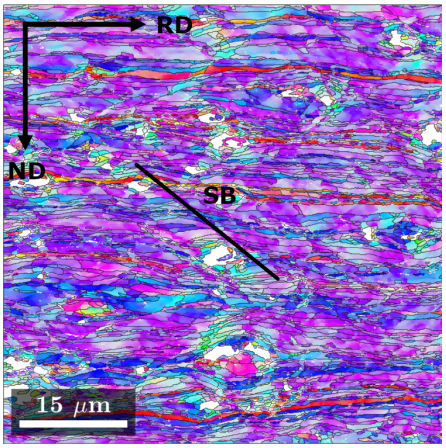

(b) 1.11 - Air

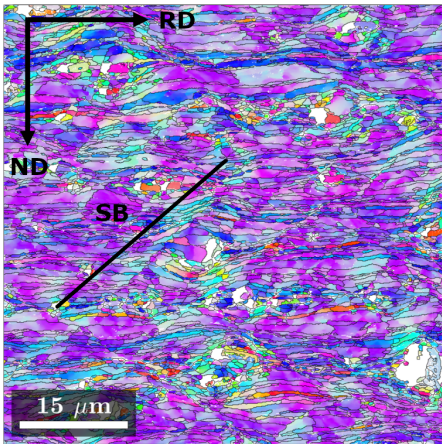

(c) 1.33 - Fan

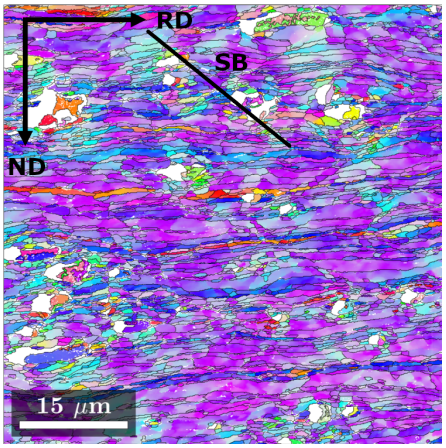

(d) 1.33 - Air

Figure 4.7: *Orientation maps for the "As deformed" materials*

Recovery

Orientation maps for the materials in the "Recovery" state are shown in Figure 4.8. The microstructure is more ordered than for "As deformed". More pronounces shear bands can be observed compared to "As deformed", and the shear bands in the southwest-northeast diagonal are sharper than the ones in the northwest-southeast diagonal, which are broader.

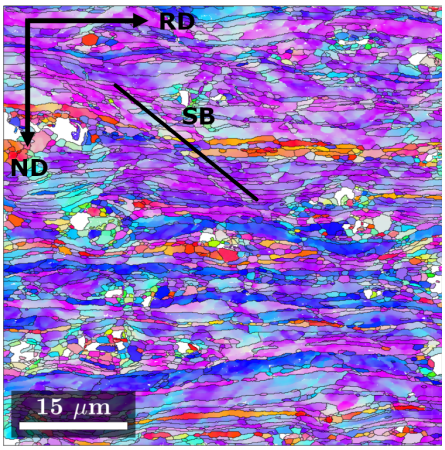

(a) 1.11 - Fan

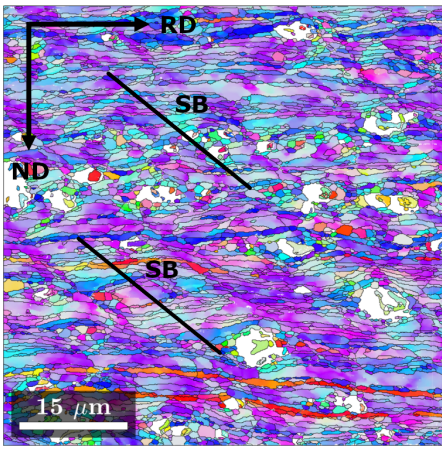

(b) 1.11 - Air

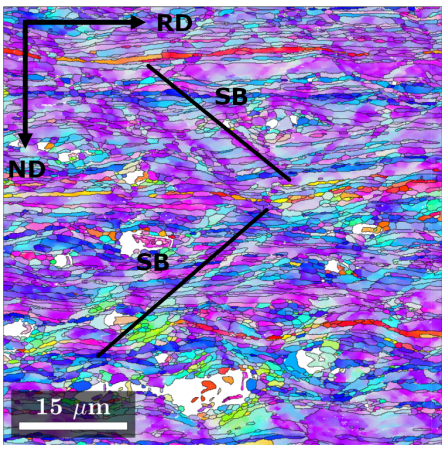

(c) 1.33 - Fan

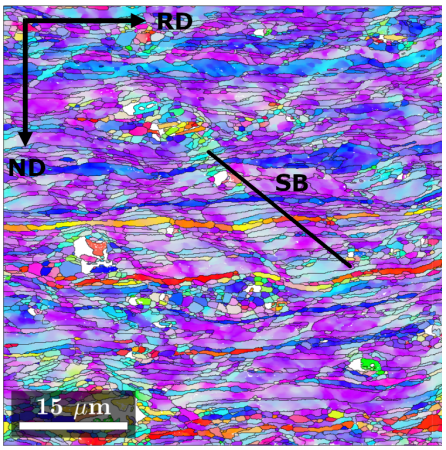

(d) 1.33 - Air

Figure 4.8: *Orientation maps for the materials in the "Recovery" state.*

Partly RX

Orientation maps for the materials in the "Partly RX" state are displayed in Figure 4.9. Recrystallization has been initiated, and recrystallized grains that are larger, less elongated and with other orientations have started to consume the pancake-shaped deformed microstructure. Larger recrystallized grains, which have consumed more of the deformed microstructure are observed in 1.11 - Air and 1.33 - Fan. A large grain with more orientation spread than the other recrystallized grains is observed in 1.33 - Air, marked in Figure 4.9d.

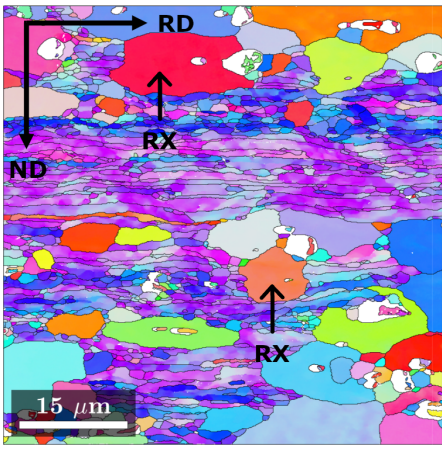

(a) 1.11 - Fan

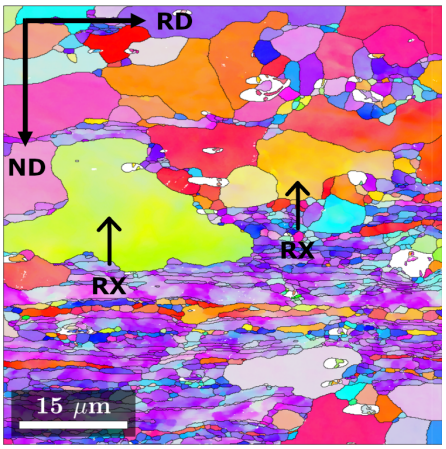

(b) 1.11 - Air

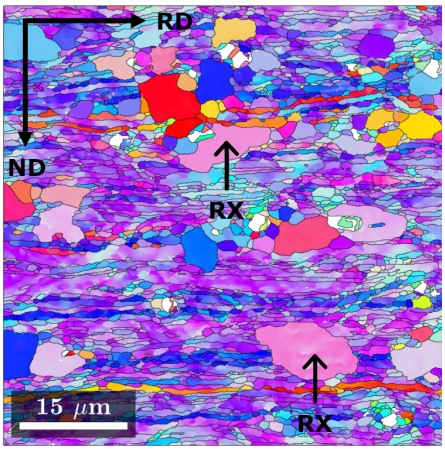

(c) 1.33 - Fan

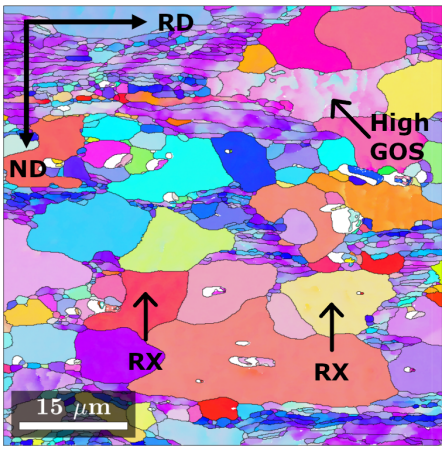

(d) 1.33 - Air

Figure 4.9: *Orientation maps for the materials in the "Partly RX" state.*

Fully RX

Orientation maps for the materials in the "Fully RX" state are shown in Figure 4.10. The previous deformed microstructure is now more or less completely consumed by the recrystallized grains. However, some remnants of the deformed microstructure is observed in 1.11 - Air. The recrystallized microstructures consist of grains with various sizes.

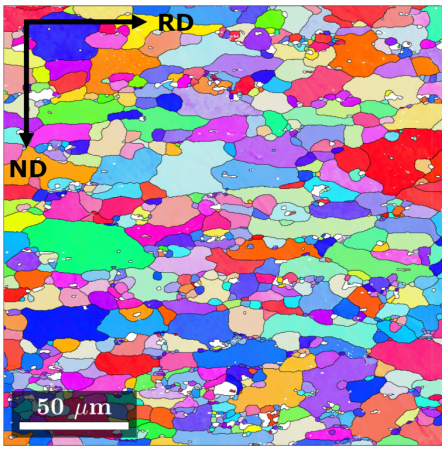

(a) 1.11 - Fan

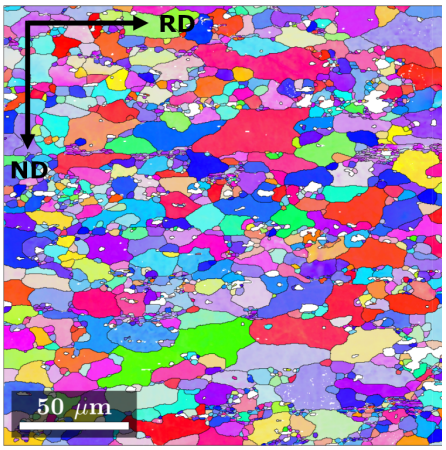

(b) 1.11 - Air

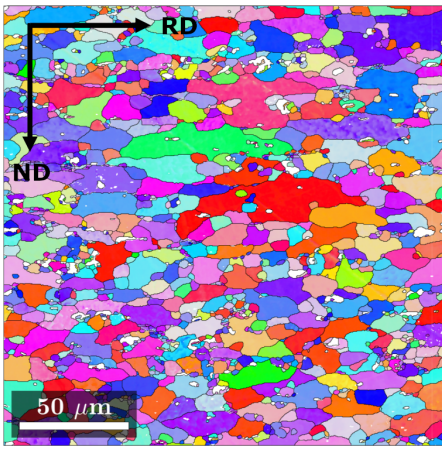

(c) 1.33 - Fan

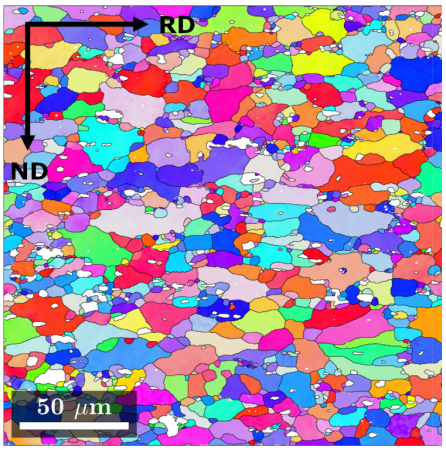

(d) 1.33 - Air

Figure 4.10: *Orientation maps for the materials in the "Fully RX" state.*

4.2.2 Segmentation maps

As described in Section 3.7.1, grains were segmented into subgrains (Sub), recrystallized grains (RX) and grain in the deformation structure that had not yet developed into subgrains (OG). Figure 4.11 shows how these grains appeared in the "As deformed", "Recovery", "Partly RX" and "Fully RX" state, in what the author has labelled "Segmentation maps". *1.33 - Fan* was used to illustrate the result of the grain segmentation. "As deformed", the deformed microstructure consists of a mixture of Original grains and subgrains. It is important to emphasize that the both Subgrains and OG grains are deformed grains. Nevertheless, within the OG grains, the dislocations have not formed boundaries that exceeds the lower limit for detection of grain boundaries, which is set to 2° in this work. Segmentation maps for all materials can be found in Appendix A

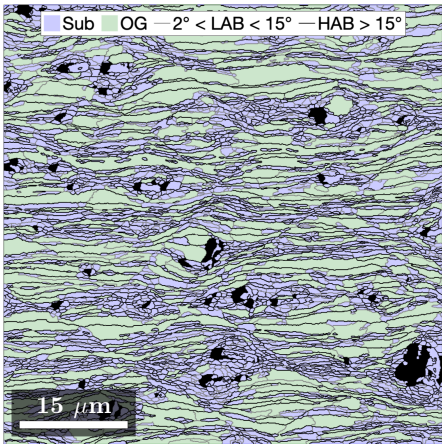

(a) As deformed

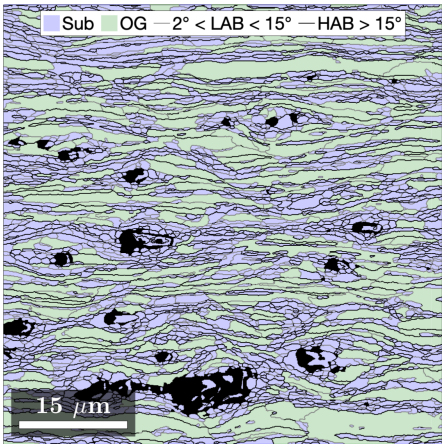

(b) Recovery

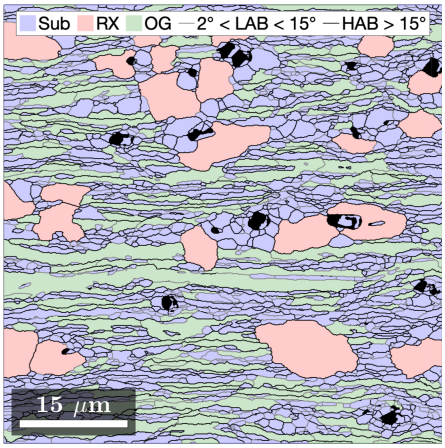

(c) Partly RX

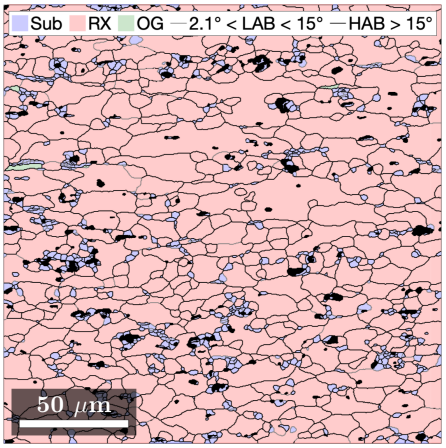

(d) Fully RX

Figure 4.11: *Segmentation maps of the 1.33 - Fan material, showing the development of grain structure during back-annealing.*

4.2.3 Grain statistics

The subgrain size distributions of the hot deformed materials are displayed in Figure 4.12. The figure shows that the for *1.11*, *Air* contains a severely larger amount of subgrains than *Fan*, in the same size range. For *1.33*, it can be seen that *Fan* is shifted toward a smaller subgrain size than *Air*.

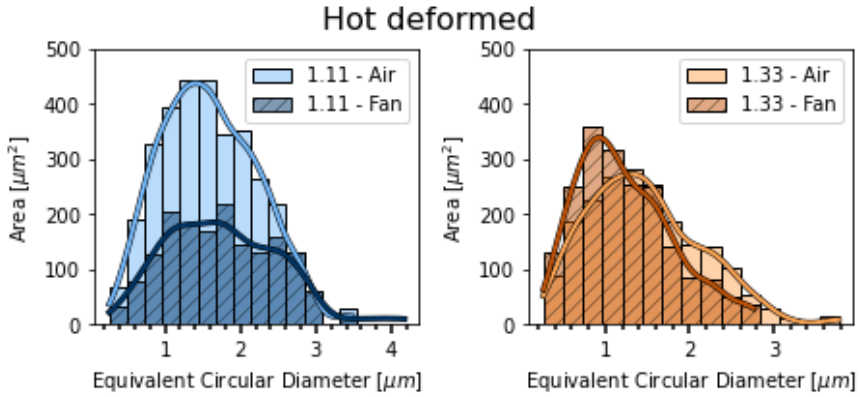

Figure 4.12: *Distribution of subgrains in the hot deformed materials.*

The subgrain size distributions for the materials are displayed in Figure 4.13. A clear tendency can be seen in both *1.11* and *1.33*: One of the parallels contains a higher amount of area occupied by subgrains < 1 µm. This parallel is *Air* for *1.11*, while *Fan* for *1.33*.

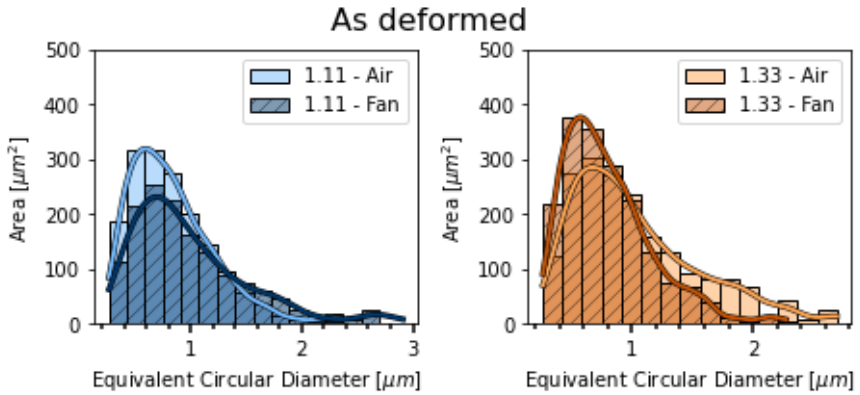

Figure 4.13: *Grain size distribution of subgrains in the "As deformed" state.*

In the "Recovery" state, the trend observed "As deformed" is still observed in *1.11*, but is less distinct for *1.33*. Figure 4.14 shows that *1.11* has more area occupied by smaller subgrains in *Air*, compared to *Fan*. For *1.33*, the difference between *Air* and *Fan* seem less pronounced than for "As deformed", but can still be observed. It is also observed that the shape of the grain size distributions has evolved to a slightly broader distribution.

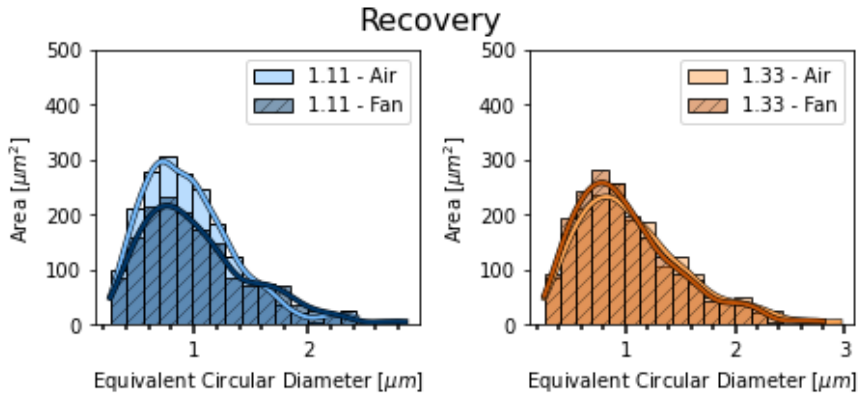

Figure 4.14: *Grain size distribution of subgrains in the "Recovery" state.*

The distribution of grains classified as RX grains in the "Fully RX" state is shown in Figure 4.15. The RX grains are in the range of 3-20 µm. For *1.11*, *Air* shows a larger fraction of grains $<$ 15 µm than *Fan*, which shows an increased amount of grains in the range of 16-20 µm. For *1.33*, the distributions are more equal, although a peak, similar to the one observed for *1.11* - *Fan*, is observed (though not that pronounced). Nevertheless, it is *Air* that displays the peak, in contrary to for *1.11*, where it is *Fan* that exhibits this feature.

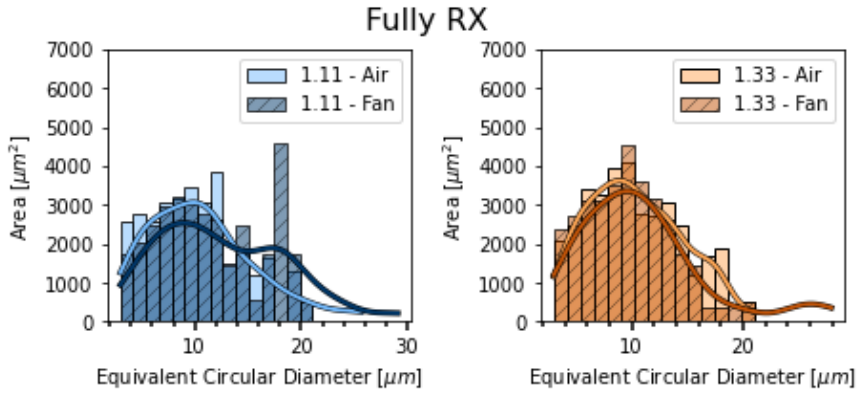

Figure 4.15: *Grain size distribution of RX-grains in the "Fully RX" state.*

The subgrain sizes in the "Hot deformed", "As deformed" and "Recovery" state is presented in Figure 4.16a. The average subgrain size for the "Hot deformed" materials varies between 1.2-1.7 µm. The cold deformation has clearly reduced the subgrain size. In the "As deformed"

state, a tendency of a lower subgrain size for *Air* is observed for *1.11*, whereas *Fan* possesses the lowest subgrain size for *1.33*. These differences seem to have more or less diminished in the "Recovery" state.

The fraction of subgrains are shown in Figure 4.16b. In the "Hot deformed" state, *1.11 - Air* show a much higher fraction of subgrains than the other materials in this state. In the "As deformed" state, *Air* show a higher fraction of subgrains than *Fan*. In the "Recovery" state, the same trend is observed for *1.11*, but not for *1.33*, for which *Fan* has a higher fraction of subgrains. Except for *1.33 - Air* at "Recovery", the measurements of subgrain fractions generelly shows an opposite trend compared to the subgrain sizes, i.e. that the materials with lowest subgrain size also shows a higher fraction of subgrains, although the differences between the materials are small.

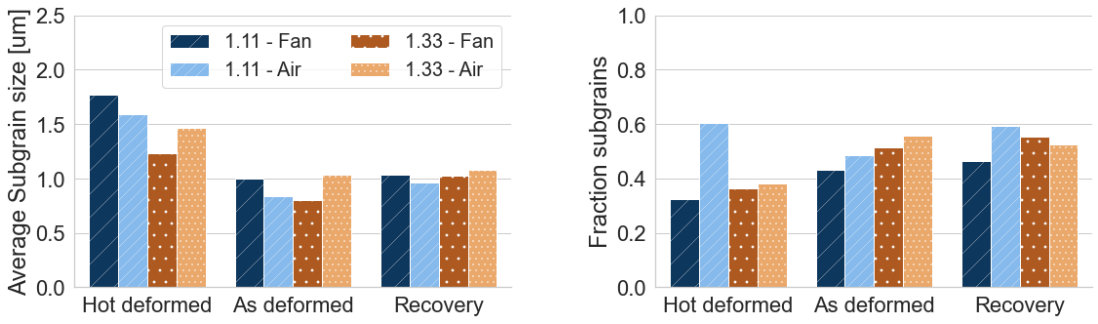

(a) *Average area weighted subgrain size* ***(b)*** *Fraction of grains classified as subgrains*

Figure 4.16: *Development of subgrains in the "Hot deformed", "As deformed" and "Recovery" state.*

The recrystallized (RX) grain sizes and fraction recrystallized grains for the materials at "Partly RX" and "Fully RX" are shown in Figure 4.17a, respectively. At "Partly RX", *Air* displays a higher fraction of recrystallized grains than *Fan* for both *1.11* and *1.33*. A corresponing trend in RX grain size is observed. At fully RX, the materials show very similar results, except for *1.11 - Fan* that shows a larger grain size and fraction recrystallized than the other materials.

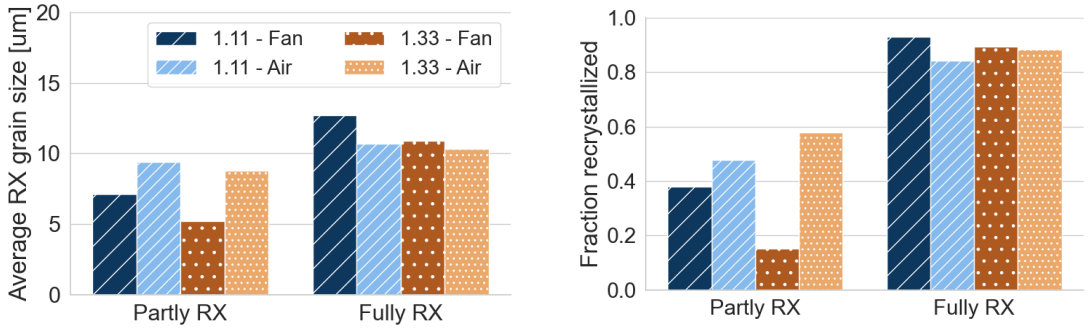

(a) *Average area weighted RX grain size* ***(b)*** *Fraction of grains classified as RX-grains*

Figure 4.17: *Development if RX-grains in the "Partly RX" and "Fully RX" state.*

4.3 Texture

4.3.1 ϕ_2 sections

In this section, the texture of the studied materials will be presented through ϕ_2 sections of ODFs and volume fractions of relevant texture components. Results from the macrotexture measurements will be presented in this section, while the microtexture results can be found in Appendix B.

Macrotexture - Hot deformed

The ϕ_2 sections presented in Figure 4.18 shows that all materials possess a typical rolling texture after hot deformation, i.e. a mixture between Br-, Cu- and S-texture. The intensity of the Br and S the most dominating, while the intensity of Cu is lower.

Macrotexture - As deformed

The ϕ_2 sections for the "As deformed" materials are displayed in Figure 4.19. Similar to the hot deformed materials, "As deformed" also shows a typical rolling texture as described above. However, the intensity of the Br-texture has been reduced, while the intensities of Cu and S remains more or less unchanged.

Macrotexture - Fully RX

In the "Fully RX" state, the rolling texture previously observed in the materials have further developed into a weaker texture consisting of remainders of the rolling texture, and components like Cube, CubeND, and Goss. Such a mixture is a typical recrystallization texture for FCC metals as described in Section 2.7.1. The ϕ_2 sections presented in Figure 4.20 shows that recrystallization is very similar for the materials, both in terms if what components that are present and their magnitude.

Hot deformed

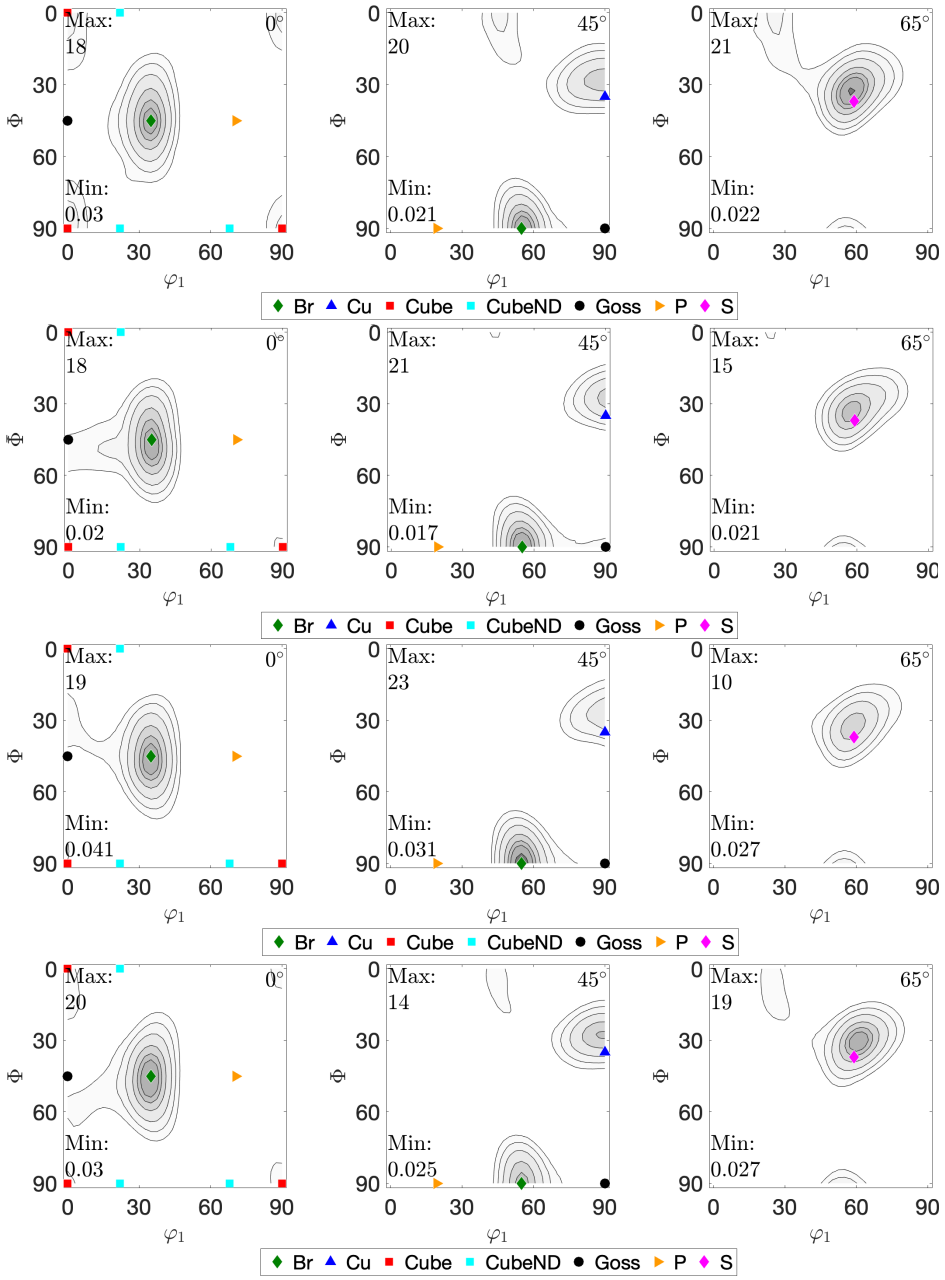

(a) *1.11 - Fan*

(b) *1.11 - Air*

(c) *1.33 - Fan*

(d) *1.33 - Air*

Figure 4.18: *ODFs of hot deformed materials, visualized by cross sections at ϕ_2 = (0°, 45°, 65°).*

As deformed

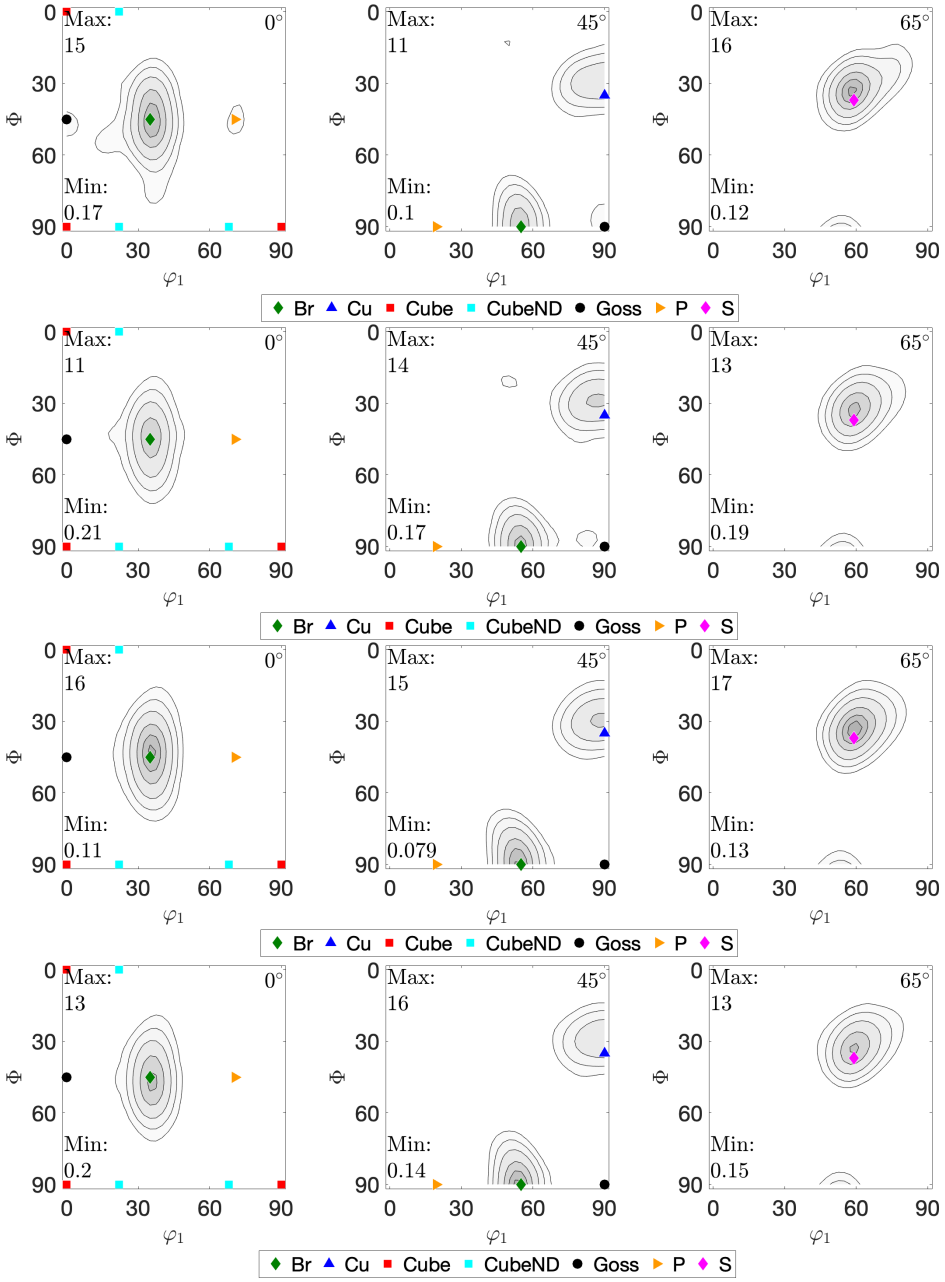

(a) *1.11 - Fan*

(b) *1.11 - Air*

(c) *1.33 - Fan*

(d) *1.33 - Air*

Figure 4.19: *ODFs of the materials in the "As deformed" state, visualized by cross sections at ϕ_2 = (0°, 45°, 65°).*

Fully RX

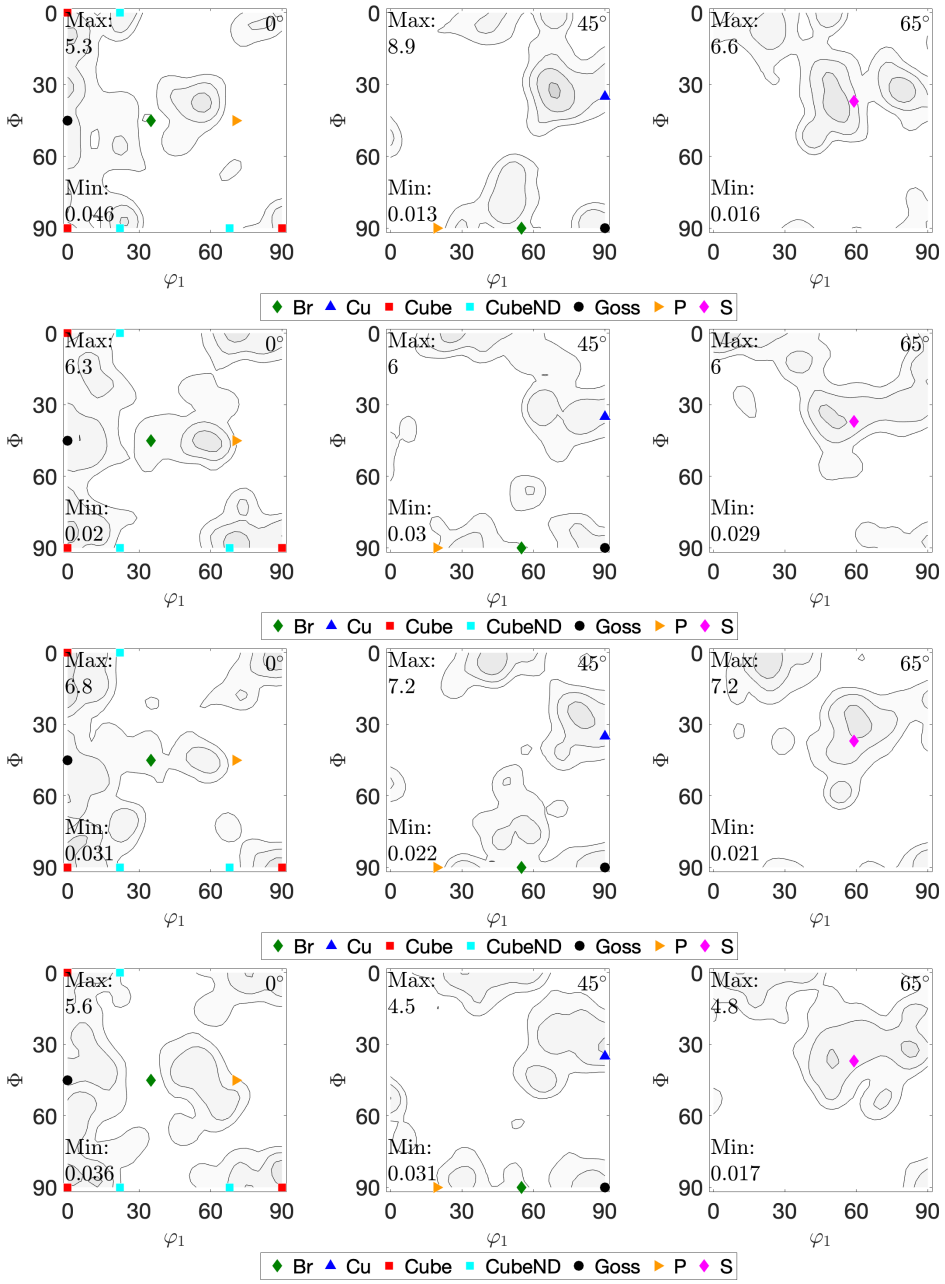

(a) *1.11 - Fan*

(b) *1.11 - Air*

(c) *1.33 - Fan*

(d) *1.33 - Air*

Figure 4.20: *ODFs of the materials in the "Fully RX" state, visualized by cross sections at ϕ_2 = (0°, 45°, 65°).*

4.3.2 Volume fraction of texture components

In this section, the development of texture from "Hot deformed" to "Fully RX" previously presented in ϕ_2 sections, is more quantitatively described in terms of volume fractions of texture components, which are presented in Figure 4.21. The volume fractions are calculated by evaluating the ratio of orientations that is within a given radius of an ideal orientation. The radius, or spread, used in the calculations is 10°. The calculations reveal that the S-texture is the most pronounced in the rolling texture, followed by Br and Cu in decreasing amounts. "Fully RX", the texture consists of the weak mixture of remnant rolling textures and other developed textures, seen in the previously presented ϕ_2 section. Of the rolling textures, clearly more remnants of S can be seen, follwed by Cu and B in decreasing amounts.

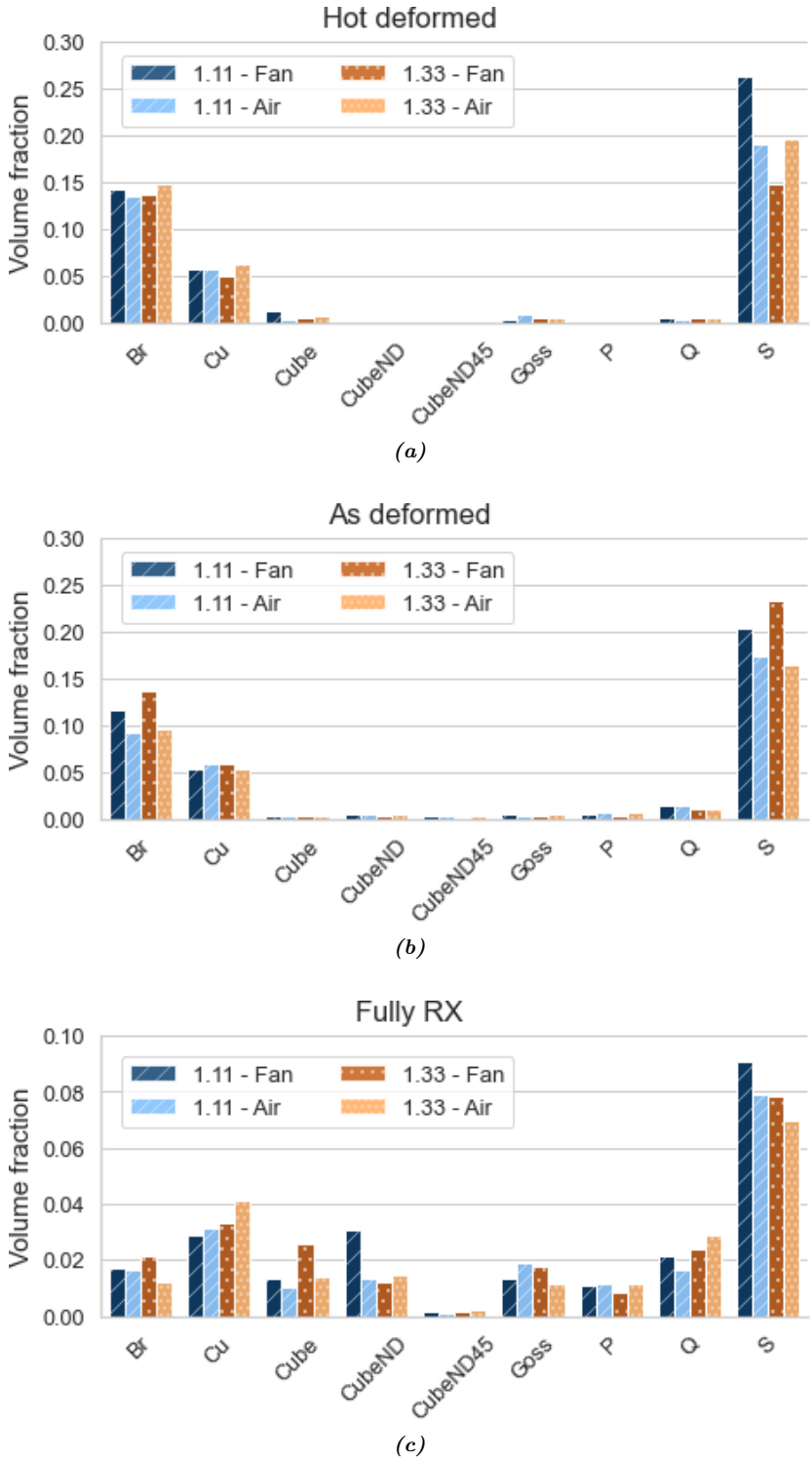

Figure 4.21: *Volume fraction of texture components in the a) "Hot deformed" b) "As deformed" and c) "Fully RX" state. Note the smaller scale used for c).*

4.4 Second phase particles

The volume fractions of dispersoids and constituent particles are presented in Figure 4.22. For the hot deformed materials, *Air* shows a higher volume fraction of dispersoids than *Fan*, whereas the opposite is observed for the constituent particles. For the "Fully RX" materials, the volume fraction of dispersoids appears to have increased for *Fan*, in both alloys. A decrease in volume fraction of dispersoids is observed for *1.33 - Air*. The volume fraction of constituent particles decreases from the "Hot deformed" to the "Fully RX" state. Such a decrease is also observed for *1.33 - Air*. The total volume fraction of second phase particles are shown in Table 4.3

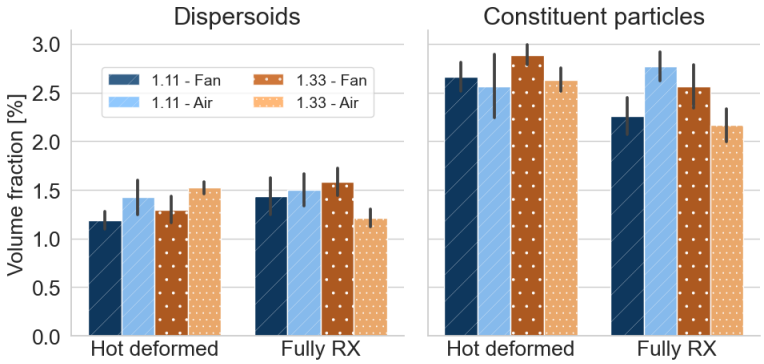

Figure 4.22: *Volume fraction of second phase particles.*

Table 4.3: *Total volume fraction of second phase particles [%].*

	1.11 - Fan	***1.11 - Air***	***1.33 - Fan***	***1.33 - Air***
Hot deformed	3.85	3.99	4.18	4.15
Fully RX	3.69	4.27	4.15	3.38

From Equation (2.3), the contributions on the yield strength from the Orowan mechanism, σ_{oro}, was calculated. The calculated contributions, along with the volume fractions, f_v and average sizes of dispersoids, d, used in the calculations are shown for the "Hot deformed" and "Fully RX" state in Table 4.4 and 4.5, respectively.

Table 4.4: *Calculated Orowan contributions and dispersoid data for the hot deformed materials.*

	1.11 - Fan	***1.11 - Air***	***1.33 - Fan***	***1.33 - Air***
f_v [%]	1.17	1.42	1.30	1.52
d [µm]	0.139	0.127	0.144	0.130
σ_{oro} [MPa]	26.8	32.1	27.4	32.8

Table 4.5: *Calculated Orowan contributions and dispersoid data for the "Fully RX" materials.*

	1.11 - Fan	***1.11 - Air***	***1.33 - Fan***	***1.33 - Air***
f_v	1.43	1.50	1.59	1.21
d [µm]	0.130	0.128	0.132	0.130
σ_{oro} [MPa]	31.6	32.9	33.1	28.7

4.4.1 Second phase particle size distributions

The size distributions for dispersoids and constituent particles are shown in Figure 4.23 and 4.24 for the materials in the "Hot deformed" and "Fully RX" states. In both states, all materials display a bimodal distribution, consisting of dispersoids smaller than around 0.3 µm, and constituent particles with size 1-5 µm. Figure 4.23 reveals that the air cooled parallels has precipitated a significantly higher amount of dispersoids < 0.2 µm in the "Hot deformed" state. The air cooled parallels also contain a slightly higher number of constituent particles between 1-2 µm.

"Fully RX", the dispersoid density appears to have increased for all materials, except for *1.33 - Air*. Where the trend in higher dispersoid density for *Air* vs. *Fan* remains for *1.11*, the opposite is observed for *1.33* in this state, for which Fan shows higher dispersoid density. A correlation between highest number density of dispersoids and constituent particles is seen for all materials in this state. The constituent particle size distributions are all more shifted towards a smaller size in "Fully RX" compared to "As deformed".

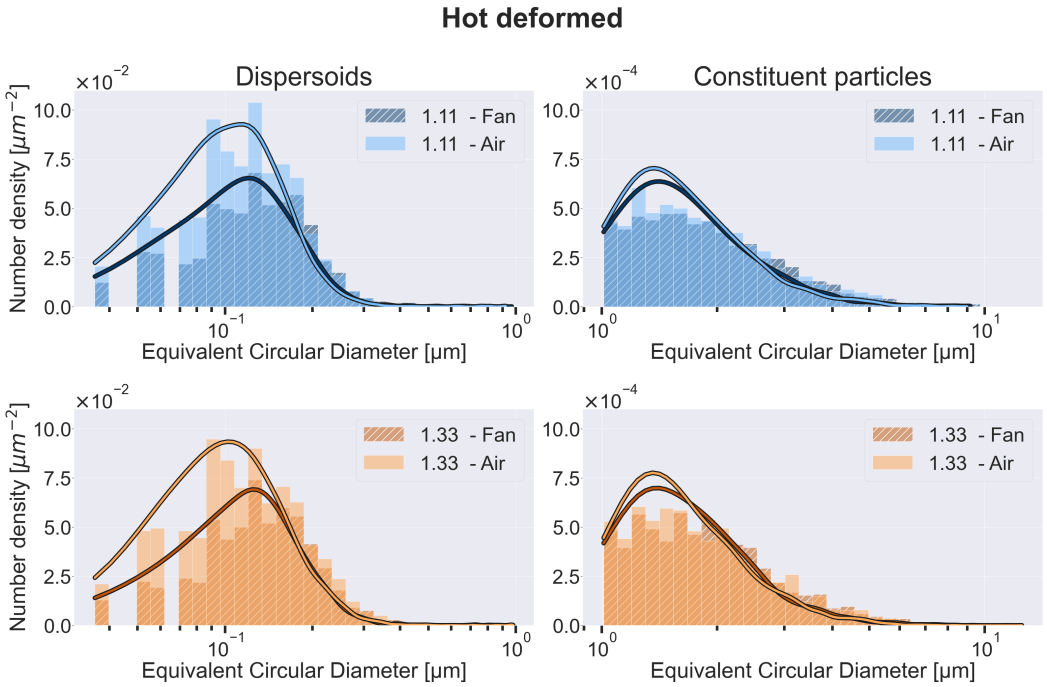

Figure 4.23: *Second phase particle distribution for the hot deformed materials. Materials with the same Mn content but different cooling conditions are plotted together. Note the different magnitude of the y axis for the dispersoids compared to the constituent particles.*

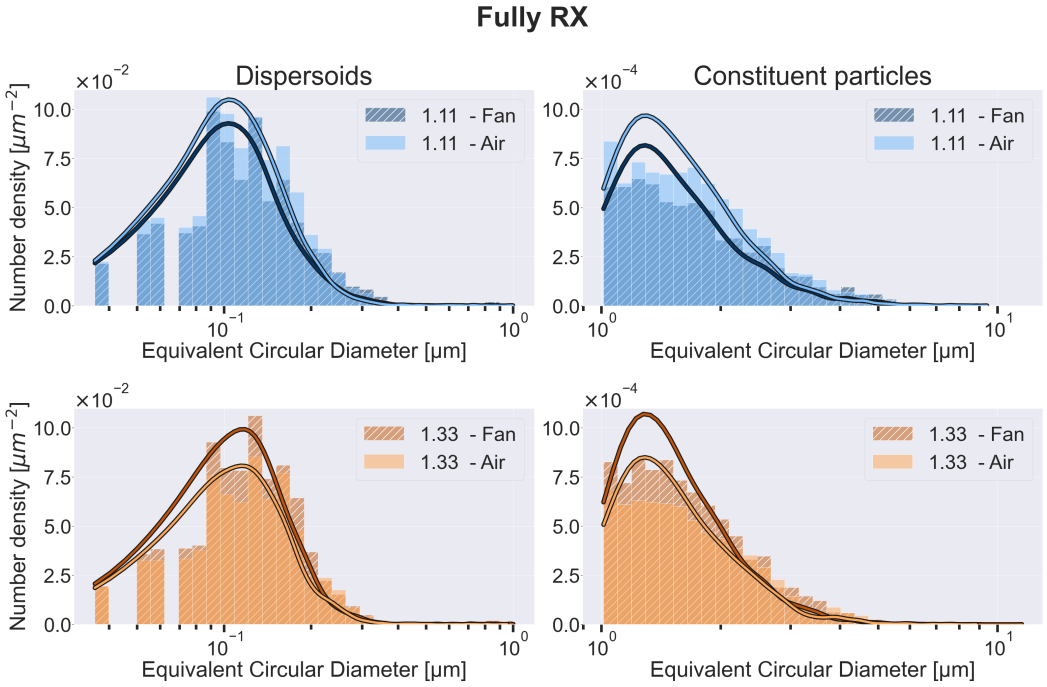

Figure 4.24: *Second phase particle distribution for the materials in the "Fully RX" state. Materials with the same Mn content but different cooling conditions are plotted together.Note the different magnitude of the y axis for the dispersoids compared to the constituent particles.*

4.5 EDS analysis of constituent particles

EDS analysis of around 30 "Constituent particles" (> 1 µm), was carried out for each of the hot deformed materials. The EDS analysis of the constituent particles all revealed significant amounts of Mn, Fe and Si, compared to the reference measurements of the Al matrix. Elemental ratios of (Fe+Mn)/Si and Mn/(Fe+Mn) are presented in Figure 4.25 and 4.26, respectively. The (Fe+Mn)/Si ratio in *1.11* is higher for *Air* than *Fan*, while the parallels are more or less equal for *1.33*, though a tendency of a slightly higher ratio is observed for *Fan*. The Mn/(Fe+Mn) ratio shows a clear tendency of higher ratio for *Air* compared to *Fan*, in both *1.11* and *1.33*. Comparatively, *1.33* is shifted towards a slightly higher ratio than *1.11*.

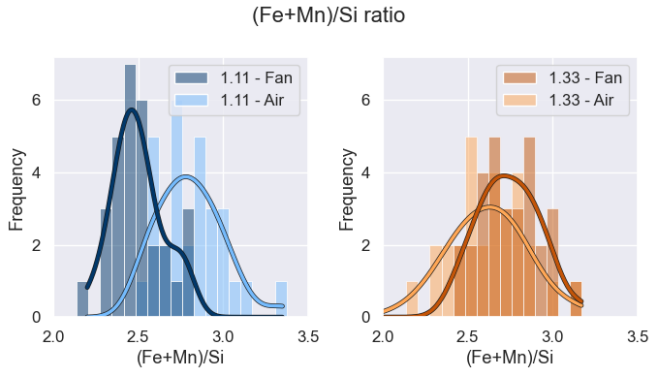

Figure 4.25: *(Fe+Mn)/Si ratio (at%) of constituent particles present in the hot deformed materials*

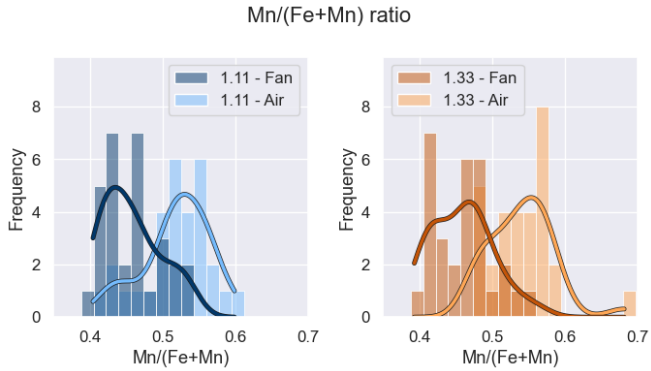

Figure 4.26: *Mn/(Fe+Mn) ratio (at%) of constituent particles present in the hot deformed materials*

5 | Discussion

The aim of this study was to reveal effects of different Mn contents and cooling conditions from hot deformation to ambient temperature in an AA 3005A alloy. Two alloys, containing 1.11 wt.% (*1.11*) and 1.33 wt.% Mn (*1.33*), respectively, have been studied. For each alloy, two parallels have been investigated: One cooled with air (*Air*), and one cooled with a fan (*Fan*), i.e. with the latter providing a much faster cooling than just air cooled. In this section, effects on the mechanical properties, texture and annealing response will be related to, and discussed in light of relevant theory and previous findings presented in Chapter 1.

5.1 Main findings

Hardness testing revealed that air cooling from hot deformation to ambient temperature resulted in slightly higher strength than fan cooling, although the difference was not significant. The electrical conductivity (EC) measurements in this state showed signs of lower EC for the *Air*, but the apparent differences between the materials in this state was statistically insignificant. Considering second phase particles, *Air* had precipitated a higher number of dispersoids than *Fan* and the air cooling also resulted in more Mn incorporated into the constituent particles, compared to fan cooling. In the "As deformed" state, *Air* remained the strongest parallel for the 1.11% Mn containing alloy, whereas the cold deformation had made *Fan* the strongest parallel for the alloy containing 1.33% Mn. Again, a high correlation with strength and low EC was observed. During back-annealing of the materials in the "As deformed" state, *Fan* and *Air* showed similar behaviour in terms of recrystallization kinetics for the 1.11% Mn containing alloys. For the 1.33% Mn containing alloy, on the other hand, *Fan* displayed slower recrystallization kinetics than *Air*, i.e. *Fan* showed a weaker annealing response than *Air*. The "Fully RX" state showed similar strength for all the materials, though remnants of the same tendencies as observed in the "As deformed" state, such as the strength difference between *Air* and *Fan*, could be seen. The materials displayed similar recrystallized grain sizes, at around 10 µm. A higher number density of second phase particles was observed for *Air* compared to *Fan* in the 1.11% Mn containing alloy, while the opposite was observed in the alloy containing 1.33% Mn.

Considering the texture development, the "Hot deformed" materials displayed a typical rolling texture consisting of S, Br, and Cu, in decreasing volume fractions. "Fully RX", the texture of the materials had developed into a mixture of typical recrystallization texture components like Cube, CubeND, Goss, P and Q, along with remnants of the rolling texture. Comparing the

materials, no major differences in texture or the texture evolution were observed.

5.2 "Hot deformed"

Previously shown in Figure 4.1a, the materials displayed similar hardness in the "Hot deformed" state, though a slight tendency of higher hardness (2-4 HV1) for *Air* compared to *Fan* was observed for both alloys. Shown in Figure 4.1b, the EC measurements in this state were similar for the "Hot deformed" materials, although a slight tendency of higher EC for *Fan* compared to *Air* were observed for both alloys. However, the uncertainty of the measurements were high and did not provide good enough statistics to differ between the materials with significance. Moreover, an estimate of the Mn in SS (Mn_{SS}) as a function of the EC measurements presented in Table 4.3 and Figure 4.22 were made, calculated from Equation (3.4). However, error propagation from EC measurements resulted in uncertainty to such a degree that no significant differences between the estimates could be observed in the "Hot deformed" state, as shown in Figure 4.2. The strength advantage for *Air* compared to *Fan* could have several origins. Different amounts of Mn_{SS} could result in a different extent of solid solution hardening, described in Section 2.5.1. However, this seems unlikely, as *Air* displays higher hardness than *Fan*. For *Air* to have more Mn_{SS} than *Fan*, it follows that more Mn must have precipitated into second phase particles in *Fan* than in *Air*. Table 4.3 shows that the total volume fraction of second phase particles is similar for *Air* and *Fan* in the alloy containing 1.33% Mn. In the 1.11% Mn containing alloy, *Air* contains more second phase particles than *Fan*. Moreover, the EDS analysis of the constituent particles (> 1 µm) presented in Figure 4.25 and 4.26 indicated a higher Mn content in the constituent particles in *Air* compared to *Fan*. Hence, a strength advantage for *Air* due to solid solution hardening seems unlikely.

As the air cooled materials contained a higher number density of dispersoids, shown in Figure 4.23, the strength differences could be attributed to the Orowan mechanism, described in Section 2.5.3. The calculations of of yield strength contribution due to the Orowan mechanism shown in Table 4.4 revealed that the increased amount of dispersoids in *Air* resulted in ≈ 5 MPa increase of the Orowan contribution, which was seen for both alloys. Hence, it is plausible that dispersoid strengthening is the origin of the strength difference. However, strength differences due to different substructures, as described in Section 2.5.5, could also contribute to the observed differences in strength. The measured subgrain sizes of the "Hot deformed" materials are presented in Figure 4.16a, and display large variations. Large variations are also seen in the subgrain size distributions in Figure 4.12 and in the orientation maps in Figure 4.6, both regarding grain size, texture and the degree of how well-defined the substructures are. Figure 4.6 shows a distinctly more well-defined substructure, i.e. the formation of subgrains to a higher extent, for the air cooled 1.11% Mn containing alloy than the other materials. This is not consistent with the higher strength measured in *Air* compared to *Fan*. A more well-defined substructure indicates more softening of the material through recovery processes. To summarize, the grain statistics from the orientation maps of the "Hot deformed" materials indicate that the scanned area was not large enough to be representative for the materials. However, this does not exclude the possibility of strength differences due to different extents of substructure strengthening.

5.3 "As deformed"

The "As deformed" materials show a similar correlation between high strength and low electrical conductivity as the "Hot deformed" materials, previously shown in terms of hardness and electrical conductivity measurement and tensile properties presented in Figure 4.3 and 4.4, respectively. However, where the "Hot deformed" material showed a tendency in higher strength for *Air*, the situation is a bit different in the "As deformed" materials. For the 1.11% Mn containing alloy, *Air* displays higher strength, like in the "Hot deformed" materials. In the 1.33% Mn containing alloy, on the other hand, *Fan* displays higher strength than *Air*. The data from tensile testing conducted by Hydro showed higher strength for *Fan* compared to *Air*, for both alloys. To summarize, all testing of mechanical properties at NTNU and Hydro tend to show a higher strength for *Fan* compared to *Air*, except for the hardness measurements of the 1.11% Mn containing alloy, where *Air* shows higher strength than *Fan*, a matter that will be addressed later. Although the strength differences in the cold deformed materials are not that big, it still appears that the order of *Air* vs. *Fan* has been switched. In other words, the cold working appears to have hardened *Fan* to a higher extent than *Air*. The small differences that are observed, could be attributed to differences in content of Mn_{SS}, which will be addressed later. The average values from EC measurements of the "Hot deformed" materials showed similar results for *Air* and *Fan*, with a slight tendency of higher EC in *Fan*. However, the uncertainty of the measurements were of such a high degree, making any comparison between the materials statistically unreliable. The large variations of the measurements indicate a rather inhomogeneous distribution of Mn_{SS} in the "Hot deformed" compared to the "As deformed" materials, which showed fewer variations. It is reasonable to assume that no precipitation occurs during cold deformation, due to the slow diffusion processes in solid state at this temperature. Hence, the level of Mn_{SS} should in principle be the same in the "Cold deformed" as in the "Hot deformed" state. Assuming that the difference in electrical conductivity in the "As deformed" state mainly originates from different contents of Mn_{SS}, it appears that a higher concentration of Mn_{SS} has lead to an increased hardening effect of the cold deformation.

A lower extent of recovery during cold deformation, i.e. lower dynamic recovery rate, could explain the increased effect of the work hardening for the fan cooled parallels, as solutes may reduce the stacking fault energy and also obstruct recovery processes through dislocation pinning or by affecting the mobility and concentration of vacancies.[85] That being said, dynamic recovery is a phenomena usually associated with deformation at higher temperatures, i.e. hot deformation. Nevertheless, several authors have reported that it may also occur during lower temperatures for aluminium.[86,87] However, these reports have been made about pure commercial aluminium, i.e. aluminium with very high stacking fault energy and far less solute concentration than the materials in this study, making dynamic recovery a less plausible cause of the observed difference in effect of the cold deformation.

The subgrain size distributions shown in Figure 4.13 along with the mechanical properties displayed in Figure 4.3 and 4.4, shows a tendency of a smaller subgrain size for the materials the display the highest strength in the "As deformed" state. As described in Section 2.5.5, a smaller subgrain size may increase the flow stress. This indicates that the strength differences observed in the "As deformed" state could originate from substructure strengthening in the form of smaller subgrains.

However, the presence of a high density of dispersoids have also been shown to increase the

effect of work hardening in Al-Mn alloys,[34] through enhancing the formation of a cell structure and leading to a smaller cell size. That being said, the effect is most effective at small strains. At larger strains, the cell size gets smaller than the distance between the dispersoids and their strengthening effect diminishes. It follows that the effect of work hardening in situations when both solutes and high densities of dispersoids are present is a complex matter. The results do however, not show a systematic correlation between low dispersoid density and high strength in the "As deformed" state, shown in Figure 4.3 and 4.23. Note that the dispersoid distribution is from the "Hot deformed state", though it is reasonable to assume that no significant changes in the dispersoid density occur during cold deformation.

Nevertheless, a possible increase in the effect of work hardening due to higher solute content does not explain the evolution of the 1.11% Mn containing alloy, where *Air* remains stronger than *Fan* after cold deformation and apparently has a lower EC than *Fan*, shown in Figure 4.3. The fact that *Air* displays a severely lower EC than *Fan* in the 1.11% Mn containing alloy, and approximately the same EC as *Fan* in the 1.33% Mn containing alloy, seems odd. As mentioned in Section 3.10, the EC is mainly attributed to solute elements, in this case Mn. Intuitively, a higher supersaturation of Mn_{SS} would be expected for *Fan* in the 1.11% Mn containing alloy, as a higher cooling rate would restrict diffusion processes, hence also precipitation of Mn. This, combined with the fact that the tensile testing conducted by Hydro showed a higher strength for the fan cooled materials, for both alloys, indicates that a plausible explanation could be that *Air* and *Fan* got mixed up for the 1.11% Mn containing alloy. As these materials were used for the back-annealing experiments, a possible mixup of these parallels would have affected all material states except for the "Hot deformed" state. Carrying out an analysis of second phase particles in the "As deformed" state, would give further indications on this issue. Another possibility could, of course, be to simply redo the experiments with a new 1.11% Mn containing alloy, which would clarify the matter. However, unfortunatley the time constraints of the master project work did not allow for this.

5.4 Back-annealing of "As deformed"

The difference in recrystallization kinetics between *Fan* and *Air* in the 1.33% Mn containing alloy could originate from concurrent precipitation, which may retard the recrystallization process, as described in Section 2.6.5. The EC measurements during back-annealing shown in Figure 4.3b reveal a lower EC for *Fan* than *Air* for this alloy, indicating a higher Mn content in solid solution in *Fan*. Marked in Figure 4.3, the area where the difference in softening behaviour between *Fan* and *Air* is most pronounced, is also accompanied by a larger increase in the EC for *Fan*, indicating more concurrent precipitation in *Fan* compared to *Air*. As shown in Figure 4.22, the volume fraction of dispersoids appears to have increased for *Fan* in the 1.33% Mn containing alloy, from the "Hot deformed" to the "Fully RX" state. However, the uncertainty of these measurements is rather high, and a higher number of measurements are required in order for the results to be statistically reliable.

The decrease in volume fraction of dispersoids for the air cooled parallel of the *1.33*% Mn containing alloy does not make sense, as the annealing temperature used in the isothermal annealing experiment is 315 °C. Previous work by Li and Arnberg[88] studying the precipitation behaviour of a supersaturated DC cast 3003 alloy during homogenization, showed that dispersoids started to precipitate at around 300 °C, and dissolution of dispersoids did not start before

500 °C. Although the heat treatment in their study was different than the annealing conditions in the present study, it seems unlikely that dispersoids would dissolve at 315 °C, as the dissolution is related to the solubility of Mn in solid solution, which would be expected to be similar for the two alloys, due to similar chemistry. As three measurements per material were taken to estimate the volume fraction of dispersoids, the statistics for the estimates are limited. The apparent decrease in volume fraction for *Air* in the 1.33% Mn containing alloy is more likely a result of insufficient statistics rather than dissolution of dispersoids. Hence, better statistics in terms of more measurements are required to quantify the volume fraction of dispersoids. Nevertheless, the difference in increased EC and slower softening kinetics for *Fan* in the 1.33% Mn containing alloy, marked in Figure 4.3b, show a lower annealing response in *Fan* compared to *Air*, and indicates that this most likely is a result of more concurrent precipitation in *Fan* compared to *Air* in this alloy.

5.5 "Fully RX"

In the final condition, "Fully RX", the materials show similar properties, in terms of strength, grain size and texture. That being said, some minor differences in strength is observed, similar to what was observed in the "As deformed" state, although the differences appear to be slightly smaller. Possible origins of these differences was previously discussed in Section 5.3. However, as the materials have recrystallized, the conditions for these origins have changed.

Shown in Figure 4.3 and 4.4, a correlation between high strength and low EC is observed in this state as well, although the difference in EC between *Fan* and *Air* in the 1.33% Mn containing alloy has decreased. Hence, different degrees of solid solution could contribute to the strength difference, as previously discussed in Section 5.3.

Dispersoid strengthening could also contribute to the strength difference, as previously discussed in Section 5.4. Nevertheless, estimates of the Orowan contribution showed in Table 4.5, indicate little differences between the materials, except for the air cooled parallel in the 1.33% Mn containing alloy, for which the estimate of the contribution is around 3-5 MPa lower than for the other materials. This is due to a lower measured volume fraction, which seems unlikely, as discussed in Section 5.4. Although no significant differences in the Orowan contribution can be observed, the possibility of a contribution due to this mechanism is still possible, even though the statistics of the dispersoids are insufficient to draw any clear conclusions.

Due to similar RX grain sizes shown in Figure 4.17a, strengthening due to the Hall-Petch effect seems unlikely, although a slightly larger grain size was observed for *Fan*, in the 1.11% Mn containing alloy, which may have resulted in less grain boundary strengthening than for the other materials. Although this section has discussed possible origins of the observed strength differences, it must be emphasized that the observed differences were not that large, and that the materials show similar properties in the "Fully RX" state, despite of different Mn contents and cooling conditions.

6 | Further Work

This work has focused on the effects of cooling conditions at different Mn contents in an AA3005 alloy. Effects of Mn has indirectly been discussed. A more direct comparison of the effect of Mn contents would provide an even better understanding of chemical variations in the studied alloy. The Mn contents in this work was 1.11 wt.% and 1.33 wt.% Mn, which was well within the required standard of the alloy which allows contents in the range of 1 - 1.5 wt% Mn. Studying Mn contents even closer to the limits of the specifications, i.e. 1 wt.% and 1.5 wt.% would provide a more comprehensive understanding of the effects of chemical variations and the sensitivity of the thermomechical process at Hydro.

As there are some remaining uncertainties of a possible mix up between the air and fan cooled parallels for the alloy containing 1.11 wt.% Mn, redoing the experiments for a new 3005-alloy containing 1.11 wt.% Mn will possibly clarify this.

As the EBSD-analysis of the materials subsequent to hot rolling provided insufficient statistics to evaluate the microstructure, doing a more comprehensive data collection of the materials in this state will give a more comprehensive understanding of the development of microstructure during the thermomechanical processing of this alloy. The understanding of the development of microhemistry could also been improved by doing a chemical analysis both prior and subsequent to hot rolling.

Chemical analysis of the materials prior and subsequent to hot rolling will provide a better understanding of the development of microchemistry during the thermomechanical processing of AA 3005A-alloys.

7 | Conclusion

This work has investigated the effects of different cooling conditions following hot deformation in an AA 3005A alloy with two different Mn contents. AA 3005A alloys containing 1.11 and 1.33 wt.% Mn have both been studied after two different cooling conditions: Cooling by air, and cooling by a fan, i.e. 'slow' vs 'fast' cooling. The materials have been examined in the successive states throughout the rolling process, namely after hot rolling, cold rolling and during back-annealing of the cold rolled material. The development of mechanical properties and texture of the materials has been studied and compared with the development of microstructure and microchemistry.

The conclusions from this work are presented below:

- The mechanical properties showed minor differences after hot deformation, although a tendency of higher strength for the air cooled materials was seen. The cold deformation appeared to have work hardened the fan cooled materials to a higher extent than the air cooled, as the fan cooled materials displayed the highest strength in this state, indicated by tensile testing conducted by Hydro. However, this tendency was not seen in the alloy containing 1.11% Mn during the investigations carried out by the author. That being said, the air cooled material of this alloy showed a significantly lower electrical conductivity than the fan cooled, almost the same as the fan cooled alloy containing 1.33% Mn. This was a strong indication that the fan cooled and air cooled parallels of the 1.11 wt.% Mn alloy had been mixed up. Further work in the form of redoing the experiments for a new AA 3005A alloy containing 1.11% Mn would clarify this. Nonetheless, the observed differences in mechanical properties were in general small.

- The cooling conditions showed a significant impact on the recrystallization kinetics for the alloy containing 1.33 wt.% Mn. Fan cooling lead to slower recrystallization kinetics than air cooling, most likely due to an increased amount of concurrent precipitation in the fan cooled material, following possibly more Mn in solid solution after hot rolling and cooling and thus prior to the final annealing stage. For the alloy containing 1.11 wt.% Mn, the recrystallization kinetics showed no significant effects of different cooling conditions.

- Although small differences in mechanical properties, were observed after hot deformation and cold deformation, these differences are not that pronounced after back-annealing. The back-annealing seems to 'compensate' for the observed differences, resulting in similar mechanical properties and grain structures for the fully recrystallized materials.

- The texture and texture evolution of the studied materials showed no significant differences, and appeared to be mainly unaffected by the Mn content and cooling conditions studied.
- Air cooling appeared to allow the incorporation of more Mn in constituent particles and precipitation of a higher number of dispersoids compared to fan cooling.

References

[1] M Tangstad. *Metal production in Norway*, chapter 2, page 37. Akademika Publishing, 2013.

[2] K Huang, N Wang, YJ Li, and K Marthinsen. The influence of microchemistry on the softening behaviour of two cold-rolled al–mn–fe–si alloys. *Materials Science and Engineering: A*, 601:86–96, 2014.

[3] A Rudra, M Ashiq, JK Tiwari, S Das, and R Dasgupta. Study of processing map and effect of hot rolling on mechanical properties of aluminum 5083 alloy. *Transactions of the Indian Institute of Metals*, 73:1809–1826, 2020.

[4] Z Jia, G Hu, B Forbord, and JK Solberg. Effect of homogenization and alloying elements on recrystallization resistance of al–zr–mn alloys. *Materials science and engineering: A*, 444(1-2):284–290, 2007.

[5] K Marthinsen, B Holmedal, S Abtahi, R Valle, S Chen, and E Nes. Coupled fem and microstructure modeling applied to rolling and extrusion of aluminium alloys. In *Materials Science Forum*, volume 426, pages 3777–3782. Trans Tech Publications Ltd., Zurich-Uetikon, Switzerland, 2003.

[6] H Takuda, N Yamazaki, N Hatta, and S Kikuchi. Influence of cold-rolling and annealing conditions on formability of aluminium alloy sheet. *Journal of materials science*, 30(4):957–963, 1995.

[7] J McQueen, S Spigarelli, ME Kassner, and E Evangelista. *Hot deformation and processing of aluminum alloys*. CRC press, 2011.

[8] Mtex, matlab toolbox for analyzing and modelling crystallographic textures, May 2020.

[9] Imagej, open source java image processing program, May 2021.

[10] TC Hill. *Evolution of second phase particles with deformation in aluminium alloys*. The University of Manchester (United Kingdom), 2015.

[11] Wrought Aluminum Alloys. International alloy designations and chemical composition limits for wrought aluminum and. 2015.

[12] Joseph R. Davis, editor. *Aluminium and Aluminium Alloys*. ASM International, 3rd edition, 1994.

[13] O Engler and J Hirsch. Control of recrystallisation texture and texture-related properties in industrial production of aluminium sheet. *International journal of materials research*, 100(4):564–575, 2009.

[14] O Engler, L Löchte, and KF Karhausen. Modelling of recrystallisation kinetics and texture during the thermo-mechanical processing of aluminium sheets. In *Materials Science Forum*, volume 495, pages 555–566. Trans Tech Publ, 2005.

[15] K Huang, K Marthinsen, Q Zhao, and RE Logé. The double-edge effect of second-phase particles on the recrystallization behaviour and associated mechanical properties of metallic materials. *Progress in Materials Science*, 92:284–359, 2018.

[16] AMF Muggerud, Y Li, and R Holmestad. Composition and orientation relationships of constituent particles in 3xxx aluminum alloys. *Philosophical Magazine*, 94(6):556–568, 2014.

[17] A Rollett, GS Rohrer, and J Humphreys. *Recrystallization and Related Annealing Phenomena*, chapter 15. Newnes, 2017.

[18] YJ Li and Lars Arnberg. Precipitation of dispersoids in dc-cast 3003 alloy. In *Materials Science Forum*, volume 396, pages 875–880. Trans Tech Publ, 2002.

[19] F Qian, S Jin, G Sha, and Y Li. Enhanced dispersoid precipitation and dispersion strengthening in an al alloy by microalloying with cd. *Acta Materialia*, 157:114–125, 2018.

[20] GE Dieter and DJ Bacon. *Mechanical metallurgy*, volume 3. McGraw-hill New York, 1986.

[21] A Rollett, GS Rohrer, and J Humphreys. *Recrystallization and Related Annealing Phenomena*, chapter 1. Newnes, 2017.

[22] R Le Hazif, PD Et, and JP Poirier. Glissement $\{110\}< 110>$ dans les metaux de structure cubique a faces centrees. *Acta Metallurgica*, 21(7):903–911, 1973.

[23] S Suwas and RK Ray. *Crystallographic texture of materials*. Springer, 2014.

[24] G Sachs. Zur ableitung einer fliessbedingung. *Z. Ver, Dtsch. Ing.*, 72:734–736, 1928.

[25] GI Taylor. Plastic strain in metals. *28th May-Lecture of the Institute of Metals*, 62:307–325, 1938.

[26] W Mao. On the taylor principles for plastic deformation of polycrystalline metals. *Frontiers of Materials Science*, 10(4):335–345, 2016.

[27] P Van Houtte, S Li, M Seefeldt, and L Delannay. Deformation texture prediction: from the taylor model to the advanced lamel model. *International journal of plasticity*, 21(3):589–624, 2005.

[28] A Rollett, GS Rohrer, and J Humphreys. *Recrystallization and Related Annealing Phenomena*, chapter 3. Newnes, 2017.

[29] J Gawad, A van Bael, and P van Houtte. *Multiscale Modelling of Mechanical Anisotropy*, pages 79–134. Springer International Publishing, Cham, 2016.

[30] Ø Ryen, B Holmedal, O Nijs, E Nes, E Sjölander, and H-E Ekström. Strengthening mechanisms in solid solution aluminum alloys. *Metallurgical and Materials Transactions A*, 37(6):1999–2006, 2006.

[31] A Rollett, GS Rohrer, and J Humphreys. *Recrystallization and Related Annealing Phenomena*, chapter 2. Newnes, 2017.

[32] LM Brown and RK Ham. *Dislocation-particle interactions*. Elsevier, 1971.

[33] N Hansen. Dispersion strengthening of aluminium-aluminium-oxide products. *Acta Metallurgica*, 18(1):137–145, 1970.

[34] Q Zhao, B Holmedal, and YJ Li. Influence of dispersoids on microstructure evolution and work hardening of aluminium alloys during tension and cold rolling. *Philosophical Magazine*, 93(22):2995–3011, 2013.

[35] EO Hall. The deformation and ageing of mild steel: Iii discussion of results. *Proceedings of the Physical Society. Section B*, 64(9):747, 1951.

[36] NJ Petch. The cleavage strength of polycrystals. *Journal of the Iron and Steel Institute*, 174:25–28, 1953.

[37] Ø Ryen. Work hardening and mechanical anisotropy of aluminium sheets and profiles. 2003.

[38] MR Staker and DL Holt. The dislocation cell size and dislocation density in copper deformed at temperatures between 25 and 700 c. *Acta Metallurgica*, 20(4):569–579, 1972.

[39] K Marthinsen and E Nes. The alflow-model-a microstructural approach to constitutive plasticity-modelling of aluminium alloys. In *Materials science forum*, volume 331, pages 1231–1242. Trans Tech Publ, 2000.

[40] FR Castro-Fernandez, CM Sellars, and JA Whiteman. Changes of flow stress and microstructure during hot deformation of al–1mg–1mn. *Materials science and technology*, 6(5):453–460, 1990.

[41] AW Thompson. Substructure strengthening mechanisms. *Metallurgical Transactions A*, 8(6):833–842, 1977.

[42] A Rollett, GS Rohrer, and J Humphreys. *Recrystallization and Related Annealing Phenomena*, chapter 6. Newnes, 2017.

[43] A Rollett, GS Rohrer, and J Humphreys. *Recrystallization and Related Annealing Phenomena*, chapter 4. Newnes, 2017.

[44] E Nes. Recovery revisited. *Acta metallurgica et materialia*, 43(6):2189–2207, 1995.

[45] WT Read and W Shockley. Dislocation models of crystal grain boundaries. *Physical review*, 78(3):275, 1950.

[46] PA Beck and PR Sperry. Strain induced grain boundary migration in high purity aluminum. *Journal of applied physics*, 21(2):150–152, 1950.

[47] A Rollett, GS Rohrer, and J Humphreys. *Recrystallization and Related Annealing Phenomena*, chapter 7. Newnes, 2017.

[48] S Tangen, K Sjølstad, T Furu, and E Nes. Effect of concurrent precipitation on recrystallization and evolution of the p-texture component in a commercial al-mn alloy. *Metallurgical and Materials Transactions A*, 41(11):2970–2983, 2010.

[49] A Rollett, GS Rohrer, and J Humphreys. *Recrystallization and Related Annealing Phenomena*, chapter 11. Newnes, 2017.

[50] CS Smith. Grains, phases, and interfaces: An introduction of microstructure. *Trans. Metall. Soc. AIME*, 175:15–51, 1948.

[51] E Nes, N Ryum, and OJAM Hunderi. On the zener drag. *Acta Metallurgica*, 33(1):11–22, 1985.

[52] M Hillert. Inhibition of grain growth by second-phase particles. *Acta Metallurgica*, 36(12):3177–3181, 1988.

[53] A Rollett, GS Rohrer, and J Humphreys. *Recrystallization and Related Annealing Phenomena*, chapter 9. Newnes, 2017.

[54] Lawrence Ko. *Particle Stimulated Nucleation: Deformation around Particles*. The University of Manchester (United Kingdom), 2014.

[55] A Rollett, GS Rohrer, and J Humphreys. *Recrystallization and Related Annealing Phenomena*, chapter 5. Newnes, 2017.

[56] E Nes. The concept of a grain size diagram in the analysis of the recrystallisation behaviour of almn-alloys. *Aluminium*, 52:560–563, 1976.

[57] K Huang, O Engler, YJ Li, and K Marthinsen. Evolution in microstructure and properties during non-isothermal annealing of a cold-rolled al–mn–fe–si alloy with different microchemistry states. *Materials Science and Engineering: A*, 628:216–229, 2015.

[58] Olaf Engler and Valerie Randle. *Introduction to texture analysis: macrotexture, microtexture, and orientation mapping*. CRC press, 2009.

[59] GEG Tucker. Texture and earing in deep drawing of aluminium. *Acta Metallurgica*, 9(4):275–286, 1961.

[60] HJ Bunge. Three-dimensional texture analysis. *International Materials Reviews*, 32(1):265–291, 1987.

[61] HT Jeong, SD Park, and TK Ha. Evolution of shear texture according to shear strain ratio in rolled fcc metal sheets. *Metals and Materials International*, 12(1):21–26, 2006.

[62] JR Hirsch. Correlation of deformation texture and microstructure. *Materials Science and Technology*, 6(11):1048–1057, 1990.

[63] S Benum, O Engler, and E Nes. Rolling and annealing texture in twin roll cast commercial purity aluminium. In *Materials Science Forum*, volume 157, pages 913–918. Trans Tech Publ, 1994.

[64] A Rollett, GS Rohrer, and J Humphreys. *Recrystallization and Related Annealing Phenomena*, chapter 12. Newnes, 2017.

[65] O Engler. On the origin of the r orientation in the recrystallization textures of aluminum alloys. *Metallurgical and Materials Transactions A*, 30(6):1517–1527, 1999.

[66] O Engler. An ebsd local texture study on the nucleation of recrystallization at shear bands in the alloy al-3% mg. *Scripta materialia*, 44(2):229–236, 2001.

[67] Q Zhao, H Zhang, K Huang, and K Marthinsen. Correlating oriented grain number density of recrystallisation in particle-containing aluminium alloys. *Transactions of Nonferrous Metals Society of China*, 28(2):220–225, 2018.

[68] K Huang, K Zhang, K Marthinsen, and RE Logé. Controlling grain structure and texture in al-mn from the competition between precipitation and recrystallization. *Acta Materialia*, 141:360–373, 2017.

[69] JG Morris and WC Liu. Al alloys: The influence of concurrent precipitation on recrystallization behavior, kinetics, and texture. *JOM*, 57(11):44–47, 2005.

[70] AJ Schwartz, M Kumar, BL Adams, and DP Field. *Electron backscatter diffraction in materials science*, volume 2. Springer, 2009.

[71] HW Ånes, J Hjelen, BE Sørensen, ATJ van Helvoort, and K Marthinsen. Processing and indexing of electron backscatter patterns using open-source software. In *IOP Conference Series: Materials Science and Engineering*, volume 891, page 012002. IOP Publishing, 2020.

[72] International Organization for Standardization. Metallic materials - vickers hardness test - part 1: Test method (iso 6507-1:2018). Standard, International Organization for Standardization, June 2018.

[73] Kikuchipy, open-source python library for processing and analysis of ebsd patterns, May 2020.

[74] E Vårli. Masters thesis. https://github.com/erlingvaarli/Masters-thesis, 2021.

[75] F Bachmann, R Hielscher, and H Schaeben. Grain detection from 2d and 3d ebsd data—specification of the mtex algorithm. *Ultramicroscopy*, 111(12):1720–1733, 2011.

[76] HW Ånes. Mtex snippets. https://github.com/hakonanes/mtex-snippets, 2021.

[77] Calcdensity, built-in mtex function that computes an odf from individual orientations, May 2020.

[78] MH Alvi, SW Cheong, H Weiland, and AD Rollett. Recrystallization and texture development in hot rolled 1050 aluminum. In *Materials Science Forum*, volume 467, pages 357–362. Trans Tech Publ, 2004.

[79] Rats, robust automtic treshold selection algorithm, May 2021.

[80] MS Remøe, I Westermann, and K Marthinsen. Characterization of the density and spatial distribution of dispersoids in al-mg-si alloys. *Metals*, 9(1):26, 2019.

[81] K Strobel, E Sweet, M Easton, JF Nie, and M Couper. Dispersoid phases in 6xxx series aluminium alloys. In *Materials Science Forum*, volume 654, pages 926–929. Trans Tech Publ, 2010.

[82] R Srinivasan and MA Imam. Role of dispersoids on the fatigue behavior of aluminum alloys: A review. *Fatigue of Materials III*, pages 11–22, 2016.

[83] D Altenpohl. *Aluminium und aluminiumlegierungen*, volume 19. Springer-Verlag, 2013.

[84] YJ Li and L Arnberg. Solidification structure of dc-cast aa3003 alloy and its influence on homogenization. *Aluminium (Düsseldorf)*, 78(10):834–839, 2002.

[85] A Rollett, GS Rohrer, and J Humphreys. *Recrystallization and Related Annealing Phenomena*, chapter 6, page 204. Newnes, 2017.

[86] HJ McQueen, S Spigarelli, ME Kassner, and E Evangelista. *Hot deformation and processing of aluminum alloys*, chapter 10, page 370. CRC press, 2011.

[87] H Hallén. A theory of dynamic recovery in fcc metals. *Materials Science and Engineering*, 72(2):119–123, 1985.

[88] YJ Li and L Arnberg. Quantitative study on the precipitation behavior of dispersoids in dc-cast aa3003 alloy during heating and homogenization. *Acta Materialia*, 51(12):3415–3428, 2003.

A | Segmentation maps

Hot deformed

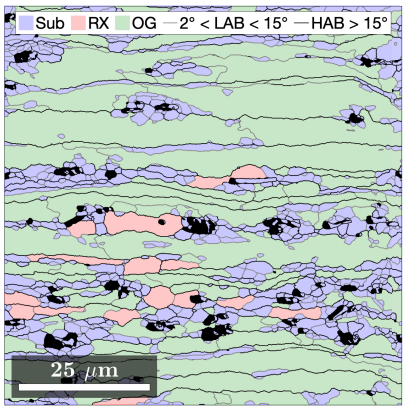

(a) 1.11 - Fan

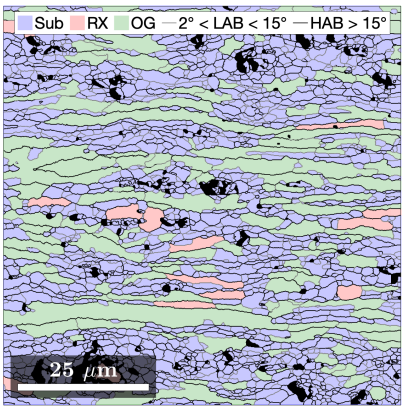

(b) 1.11 - Air

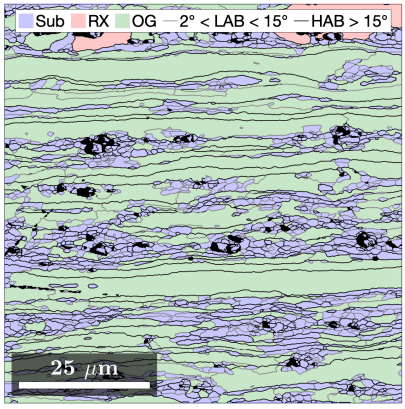

(c) 1.33 - Fan

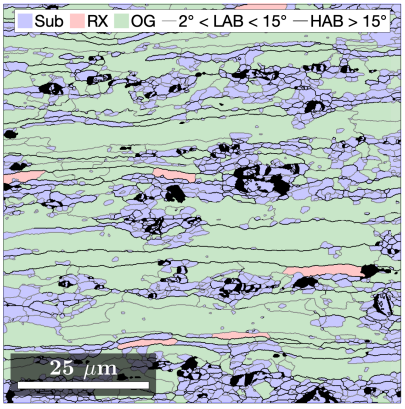

(d) 1.33 - Air

Figure A.1: *Segmentation maps of the hot deformed materials.*

As deformed

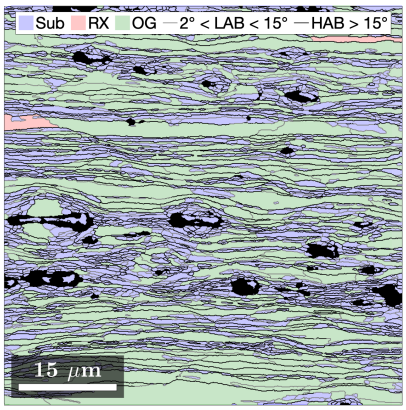

(a) 1.11 - Fan

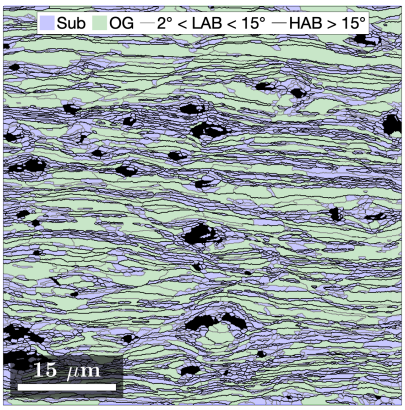

(b) 1.11 - Air

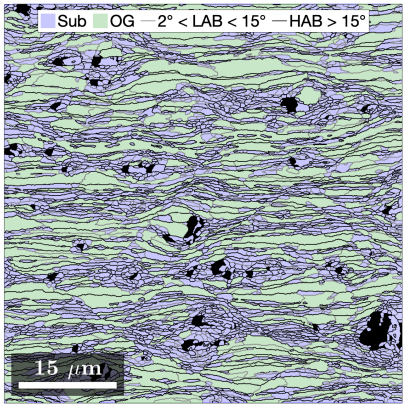

(c) 1.33 - Fan

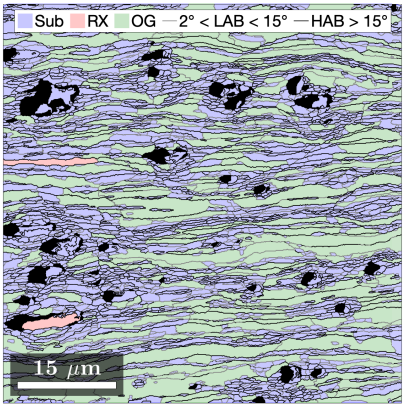

(d) 1.33 - Air

Figure A.2: *Segmentation maps of the materials in the "As deformed" state.*

Recovery

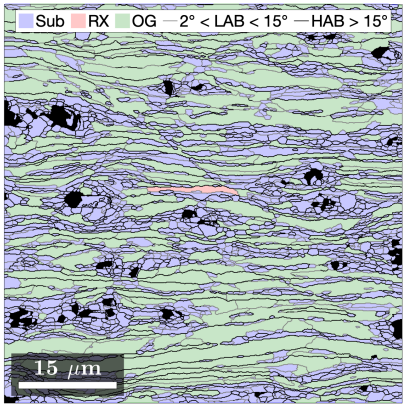

(a) 1.11 - Fan

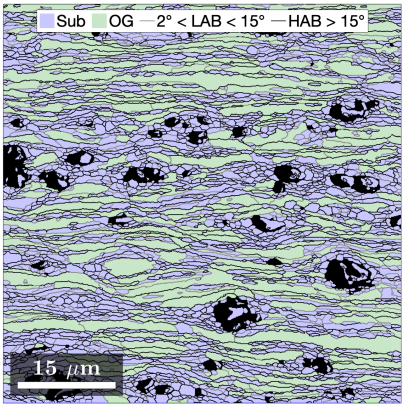

(b) 1.11 - Air

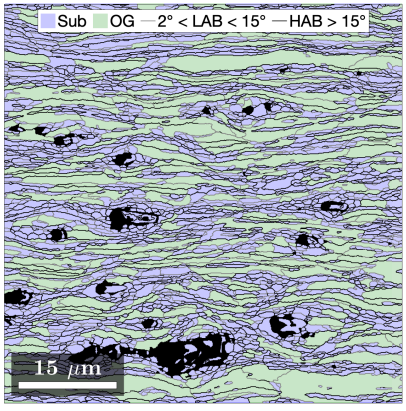

(c) 1.33 - Fan

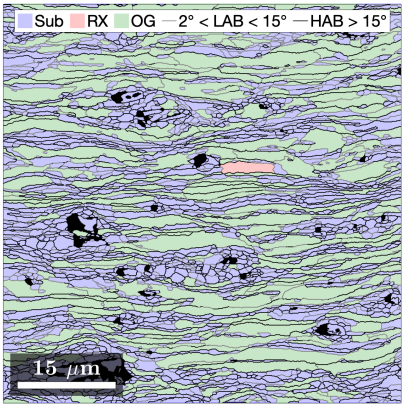

(d) 1.33 - Air

Figure A.3: *Segmentation maps of the materials in the "Recovery" state.*

Partly RX

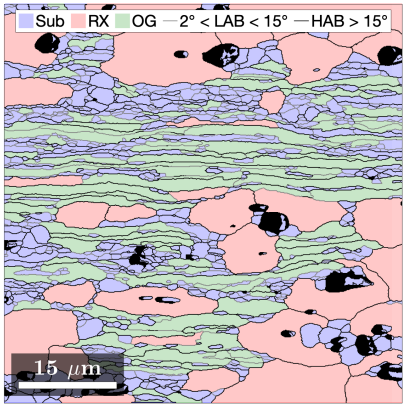

(a) 1.11 - Fan

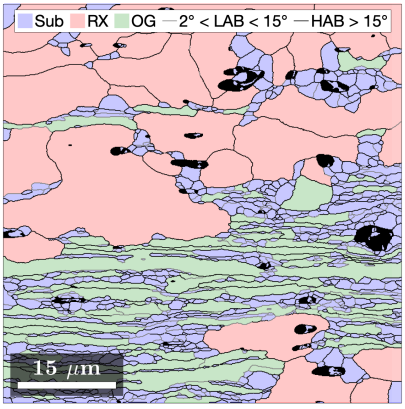

(b) 1.11 - Air

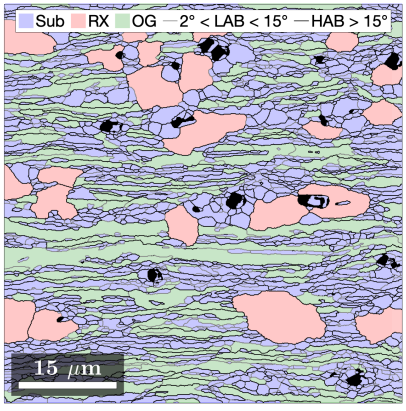

(c) 1.33 - Fan

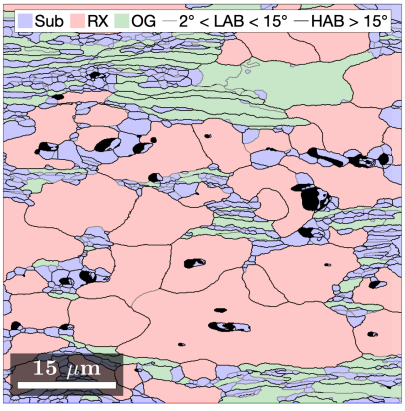

(d) 1.33 - Air

Figure A.4: *Segmentation maps of the materials in the "Partly RX" state.*

Fully RX

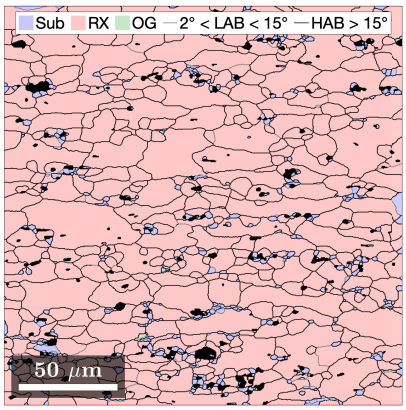

(a) 1.11 - Fan

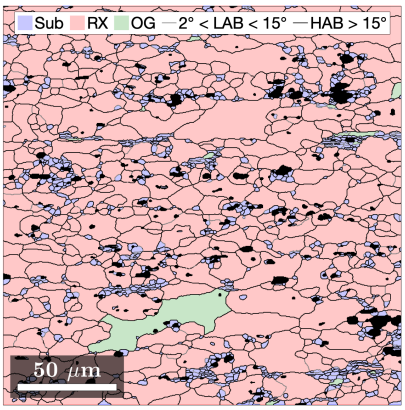

(b) 1.11 - Air

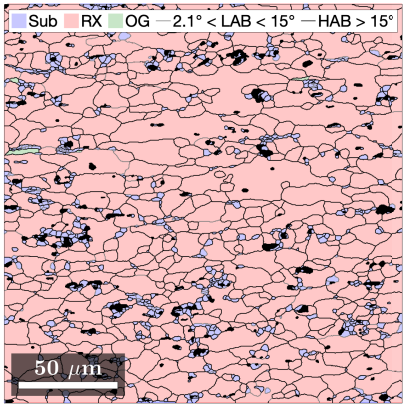

(c) 1.33 - Fan

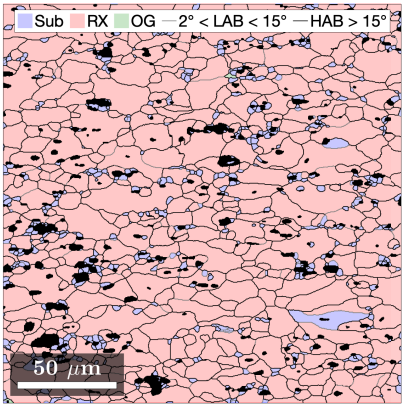

(d) 1.33 - Air

Figure A.5: *Segmentation maps of the materials in the "Fully RX" state.*

B | Microtexture

Microtexture - Hot deformed

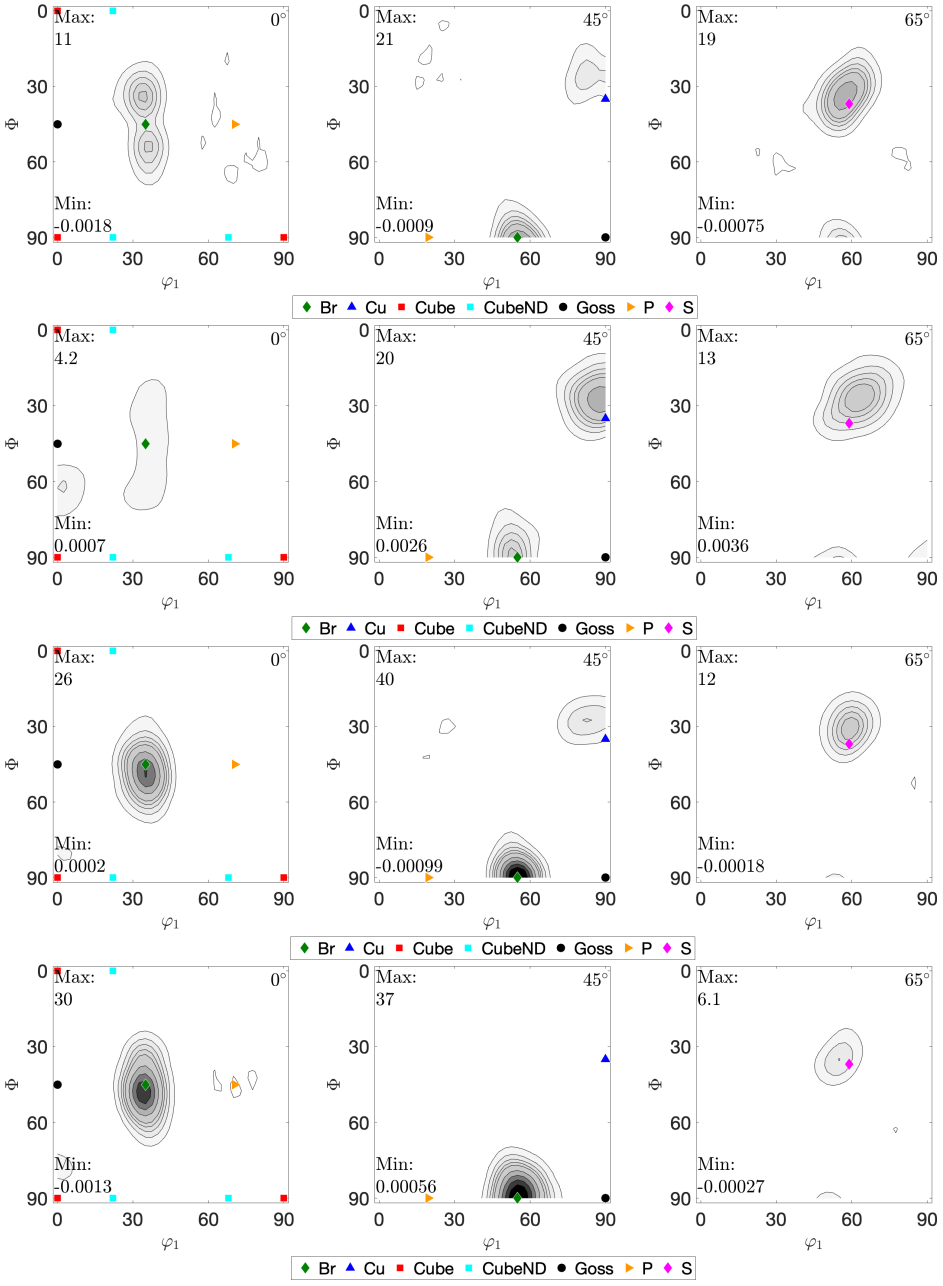

(a) *1.11 - Fan*

(b) *1.11 - Air*

(c) *1.33 - Fan*

(d) *1.33 - Air*

Figure B.1: *Microtexture measurements of the hot deformed materials, visualized by ϕ_2 sections from ϕ_2 = (0°, 45°, 65°).*

Microtexture - As deformed

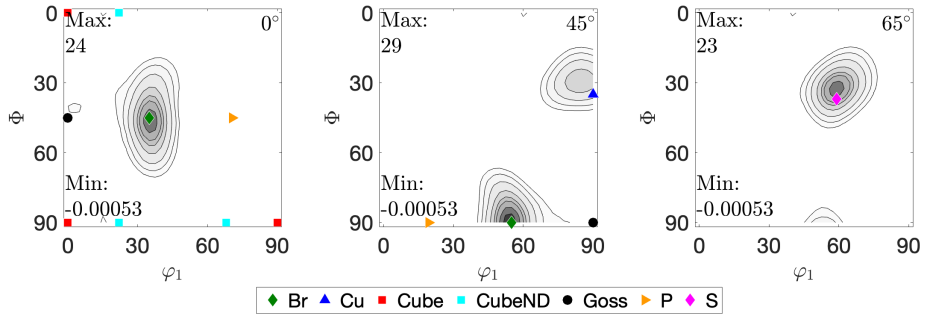

(a) 1.11 - Fan

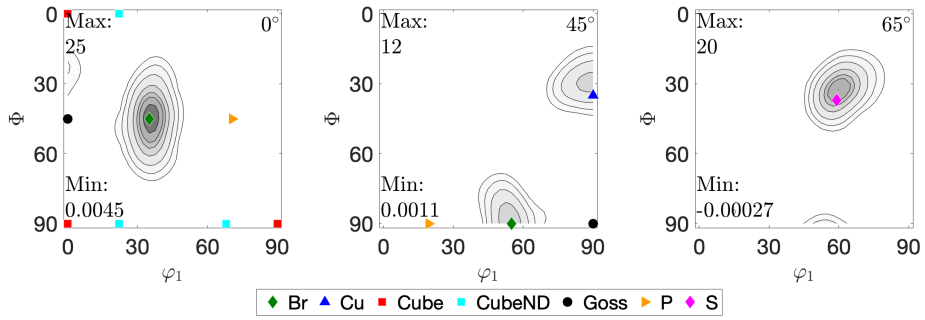

(b) 1.11 - Air

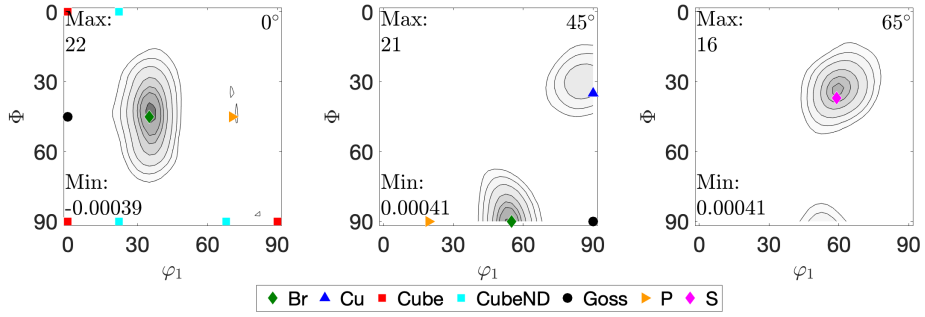

(c) 1.33 - Fan

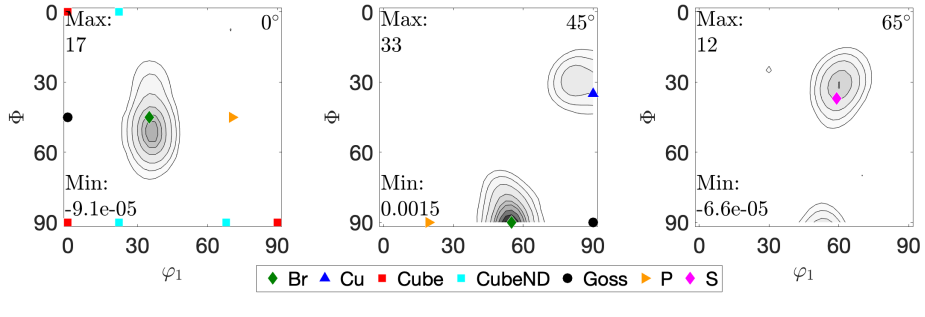

(d) 1.33 - Air

Figure B.2: *Microtexture measurements of the materials in the "As deformed" state, visualized by ϕ_2 sections from ϕ_2 = (0°, 45°, 65°).*

Microtexture - Recovery

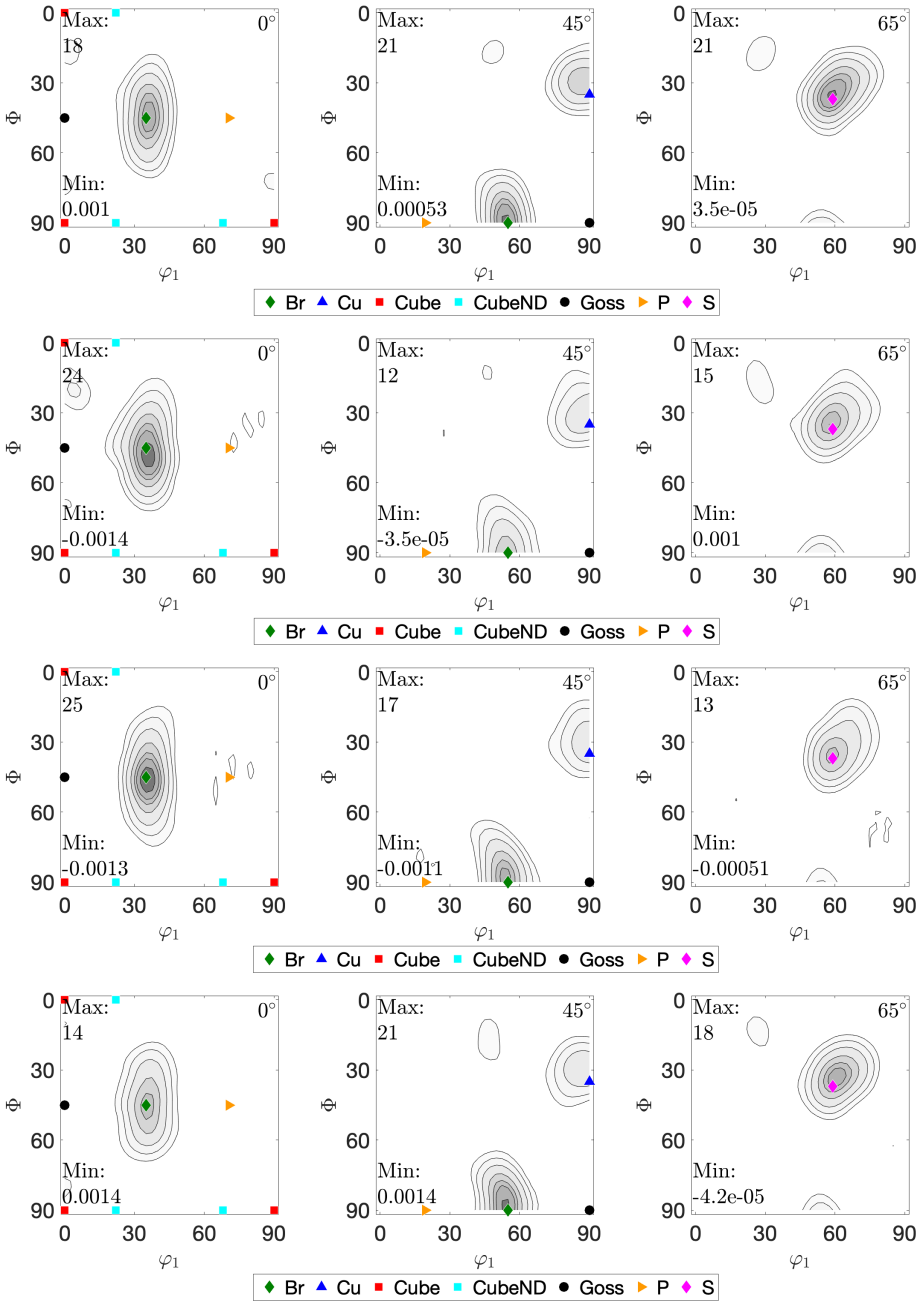

(a) 1.11 - Fan

(b) 1.11 - Air

(c) 1.33 - Fan

(d) 1.33 - Air

Figure B.3: *Microtexture measurements of the materials in the "Recovery" state, visualized by ϕ_2 sections from ϕ_2 = (0°, 45°, 65°).*

Microtexture - Partly RX

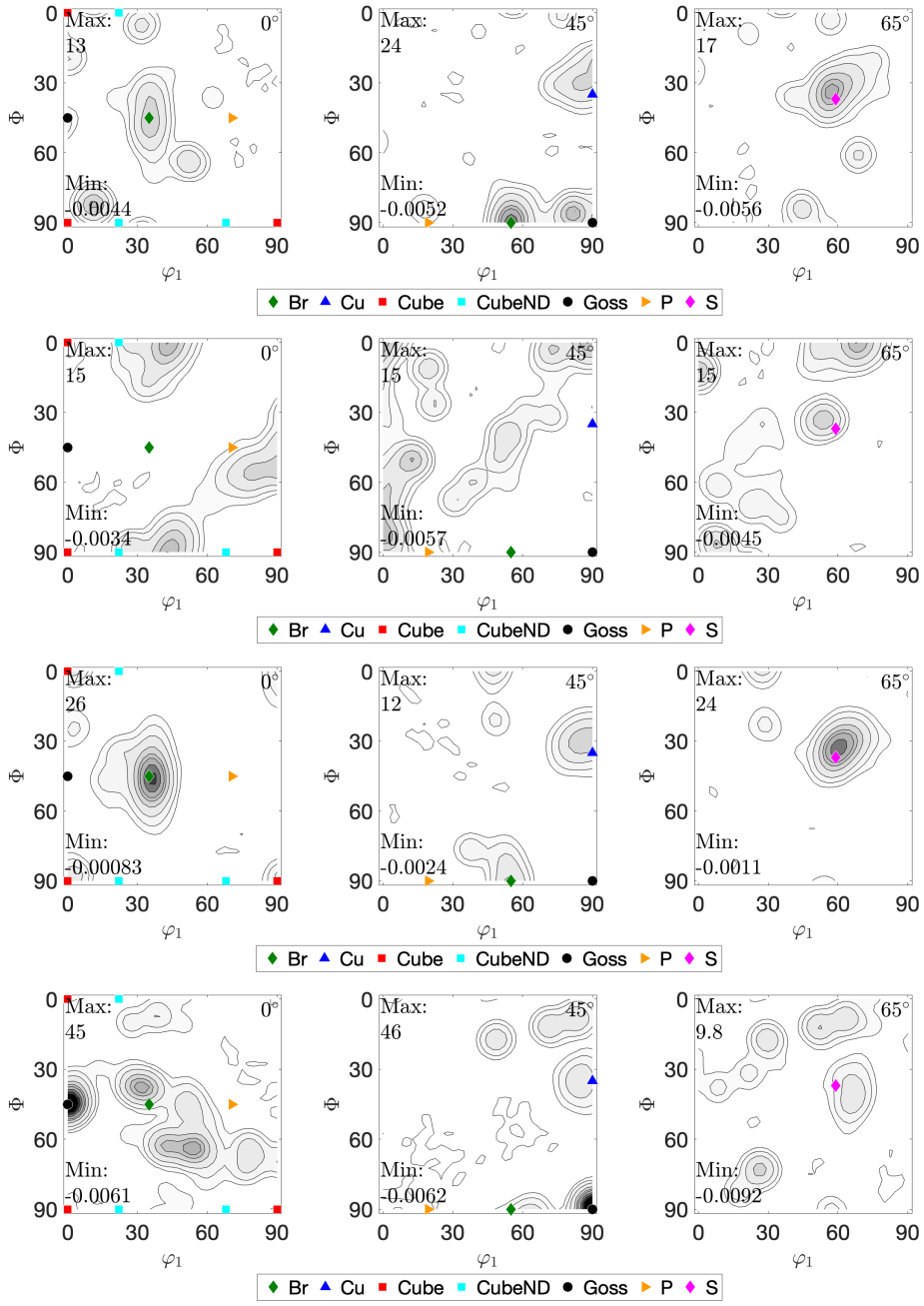

(a) 1.11 - Fan

(b) 1.11 - Air

(c) 1.33 - Fan

(d) 1.33 - Air

Figure B.4: *Microtexture measurements of the materials in the "Partly RX" state, visualized by ϕ_2 sections from ϕ_2 = (0°, 45°, 65°).*

Microtexture - Fully RX

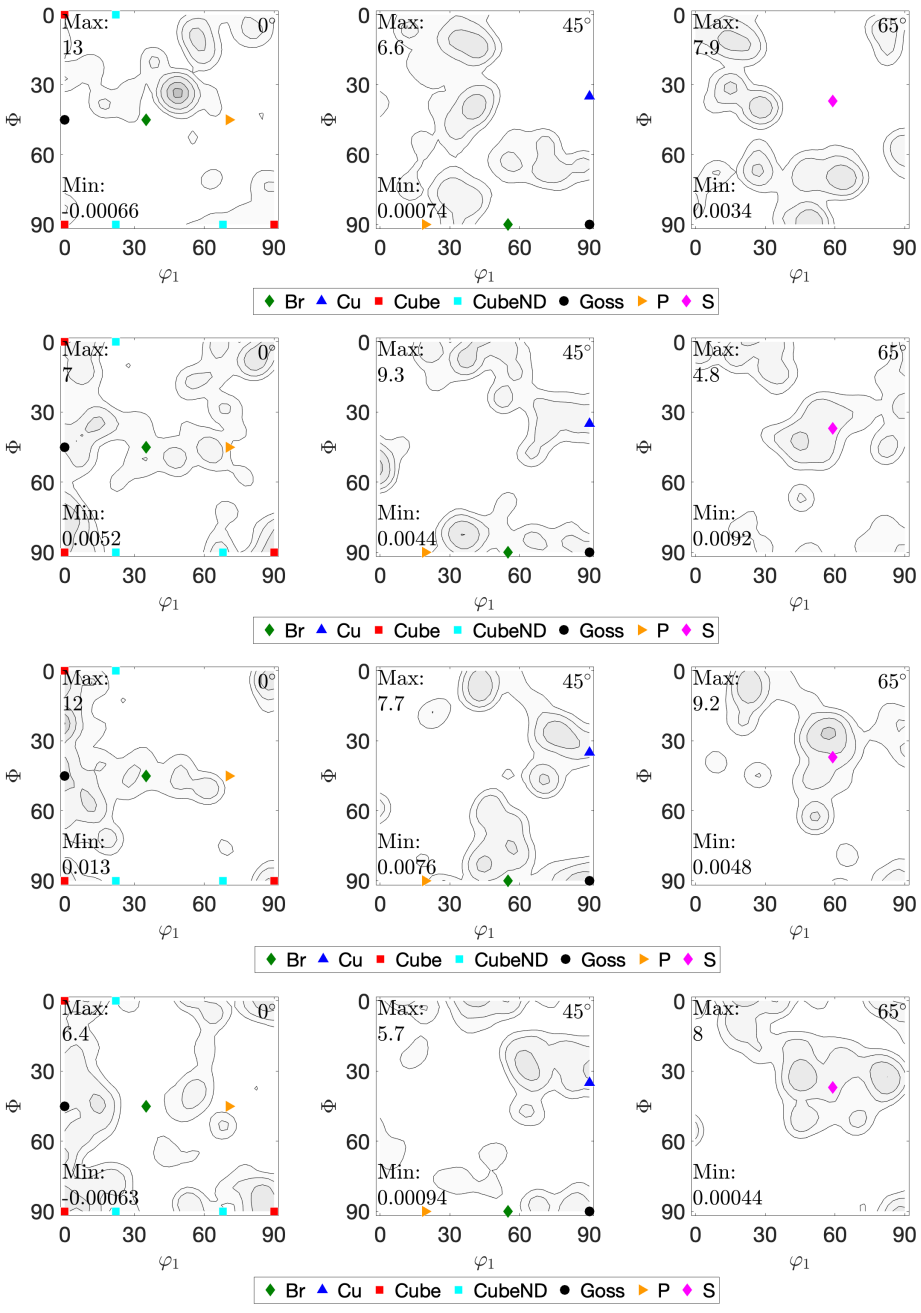

(a) *1.11 - Fan*

(b) *1.11 - Air*

(c) *1.33 - Fan*

(d) *1.33 - Air*

Figure B.5: *Microtexture measurements of the materials in the "Partly RX" state, visualized by ϕ_2 sections from ϕ_2 = (0°, 45°, 65°).*

Erling Aares Vårli

Effects of Mn content and cooling conditions in a rolled AA 3005A alloy

NTNU
Norwegian University of
Science and Technology